Infocommunications Journal

A PUBLICATION OF THE SCIENTIFIC ASSOCIATION FOR INFOCOMMUNICATIONS (HTE)

September 2011 Volume III Number 3 ISSN 2061-2079

hte

IEEE HUNGARY SECTION

Indexing information

Infocommunications Journal is covered by INSPEC and Compendex.

The journal is supported by NCA NEMZETI CIVIL ALAPPROGRAM the National Civil Fund.

Infocommunications Journal

Technically co-sponsored by IEEE Hungary Section

Editorial Office (Subscription and Advertisements)**:**
Scientific Association for Infocommunications
H-1055 Budapest, Kossuth Lajos tér 6-8, Room: 422
Mail Address: 1372 Budapest Pf. 451. Hungary
Phone: +36 1 353 1027, Fax: +36 1 353 0451
E-mail: info@hte.hu
Web: www.hte.hu

Articles can be sent also to the following address:
Budapest University of Technology and Economics
Department of Telecommunications
Tel.: +36 1 463 3261, Fax: +36 1 463 3263
E-mail: szabo@hit.bme.hu

Subscription rates for foreign subscribers:
4 issues 50 USD, single copies 15 USD + postage

Publisher: PÉTER NAGY • Manager: ANDRÁS DANKÓ

HU ISSN 2061-2079 • Layout: MATT DTP Bt. • Printed by: FOM Media

www.infocommunications.hu

Model based 3D vision and analysis for Production Audit purposes

(Invited Paper)

K.Vaiapury, A.Aksay (*Senior Member, IEEE),* X.Lin and E.Izquierdo (*Senior Member, IEEE)*

***Abstract*— This paper describes a new methodology for 3D measurement and model matching for installation audit in industrial environment. The problem is addressed by using both 3D information from 2D images and semantic meta-data of the installation engine parts by comparing with that of corresponding base CATIA installations. In this research, we deploy independent (vision- based) method to accelerate the convergence toward optimal system architecture that integrates safety constraints.**

***Index Terms*—model knowledge, installation and production audit, aircraft safety audit and analysis, three-dimensional measurement, model matching,**

I. INTRODUCTION: PRODUCTION AUDIT

WITH the availability of cheap sensors and high end 3D vision technology from the market, industries show lot of interest in automating the industrial audit process. Upon a careful analysis, one can note that there is indeed a gap that exists between the industrial need/requirement for safety analysis and existing commercial solutions (for example scanners).

The prior knowledge about industrial installations is the model information available for each of the subparts of the installation components so called DMU (Digital Mock-Ups). In this research, we took initiatives to address the auditing requirement using safety engineer input and CATIA model information as a key input for discrepancy checking.

The increase of aerospace systems complexity has meant that by using existing methods for systems development, industry has reached a barrier to innovation and a risk to the competitiveness of products. This is characterized by an increasing time to market for new technologies, increasing costs to demonstrate proof of safety, a greater demand for skilled resources and a limitation on design iterations, which means there is less time to optimize designs that are compliant with safety targets. In this work, it is aimed at filling this gap and providing methods and infrastructure that accelerate the convergence toward optimal system architecture that integrate safety constrains.

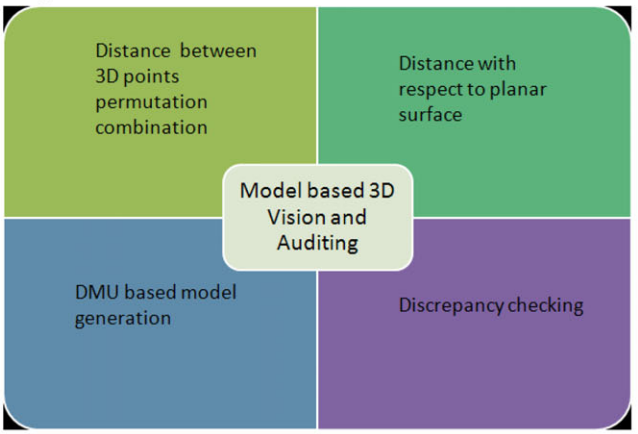

Fig 1.Functional matrix in proposed 3D Vision Auditing framework

Reliable 3D information can be extracted just using the input from 2D images of the industrial installations. As shown in Figure 1, our framework contains four functional components a) measuring distance of any permutation pair of points selected in 2D images to give measure in 3D space b) measure distance with respect to planar surface detecting using non collinear point selection c) DMU based model generation d) discrepancy checking between the visual and model information. It should be noted that functionality c is used for discrepancy checking process.

II. DISTANCE BETWEEN 3D POINTS

A. *User point selection from safety engineer perspective*

The first functionality is where a user provides points of interest with which distance constraints need to be checked.

B. *Point based disparity:*

Point based disparity is based on each of the points identified from in two images that show a different perspective of the same scene. While selecting points, first the user is shown the left image where they select the point coarsely (refer Figure 2 (a)). Then, the system shows the point location on left image that is zoomed so that the user can select the point

Manuscript received August 17, 2011. The research leading to these results has received funding from the European Community's Seventh Framework Programme FP7/2007-2013 under grant agreement n° ACP7-GA-2008-212088-MISSA.

Authors are with the MMV Research Laboratory, School of Electronic Engineering and Computer science, Queen Mary University of London, United Kingdom. Phone: 02078827132; Fax: 02078827997; email:{karthike.vaiapury,anil.aksay,xinyu.lin,ebroul.izquierdo}@eecs.qmul.ac.uk).

location very accurately. Similarly, a user will be shown the right image where they will select the point coarsely (refer Figure 2 (b)). Then the point location on the right image will be zoomed so that the user can select the point location very accurately. Since disparity is obtained manually, there is no need for outlier removal and mm level accuracy can be achieved.

Fig.2(a). Selected Points in Pipe (Left View)

Fig.2(b). Selected Points in Pipe (Right View)

C. 3D Stereo Triangulation

As stated by Izquierdo et al, two corresponding points represent the projection onto the image planes of the same object point [3]. 3D position is the intersection of both viewing lines and can be estimated using the coordinates of its projection in both images and the camera parameters. Triangulation is the process of determining the location of a point by measuring angles to it from known points at either end of a fixed baseline, rather than measuring distances to the point directly. The point can then be fixed as the third point of a triangle with one known side and two known angles.

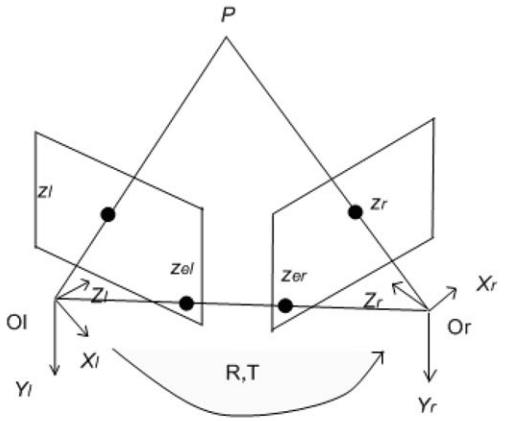

Figure 3 Epipolar stereo geometry

As shown in Figure 3, we retrieve P in space from observed projection $z_l = (u_l, v_l)$ and $z_r = (u_r, v_r)$ onto image planes. u, v represent the coordinate system used in computer or digitized image. It can also be noted that triangulation is not possible if P lies on O_l, O_r or $z_l = z_{el}$ and $z_r = z_{er}$ where z_{el} and z_{er} are epipoles.

Given 3×4 camera projection matrices M_l, M_r and z_l, z_r which represents the corresponding points in stereo images, then mathematically triangulation can be written as a function

$$P = \tau(M_l, M_r, z_l, z_r)$$

$$M_i = K_i[R_i \mid t_i]$$

Where i is the index representing number of cameras n_c

K is the calibration matrix. R_l and R_r represent the rotation matrixes of an object relative to the first camera and to the second camera. The rotation between them (R_{lr}) can be calculated as

$$R_{lr} = R_r \times R_l^{-1}$$

R_{lr} can be written as

$$R_{lr} = \begin{pmatrix} \cos\alpha\cos\gamma + \sin\alpha\sin\beta\sin\gamma & \cos\beta\sin\gamma & -\sin\alpha\cos\gamma + \cos\alpha\sin\beta\sin\gamma \\ -\cos\alpha\cos\gamma + \sin\alpha\sin\beta\cos\gamma & \cos\beta\cos\gamma & \sin\alpha\sin\gamma + \cos\alpha\sin\beta\cos\gamma \\ \sin\alpha\cos\beta & -\sin\beta & \cos\alpha\cos\beta \end{pmatrix}$$

Where α, β and γ are rotation angles around X, Y and Z axis. Similarly given two translation vectors t_l and t_r, translation between two cameras can be obtained as

$$T_{lr} = t_r - R_{lr} \times t_l$$

The 3D position of a point P can be reconstructed from the perspective projection of M on the image planes of the cameras, once the relative position and orientation of the two cameras are known.

Let $\hat{X}_l = (X_l, Y_l, Z_l)$ and $\hat{X}_r = (X_r, Y_r, Z_r)$ represent the 3D world coordinate points of point P in left and right camera coordinate systems.

$U_l = \frac{\hat{X}_l}{Z_l} = \begin{pmatrix} u_l \\ v_l \\ 1 \end{pmatrix}$, $U_l = \frac{\hat{X}_r}{Z_r} = \begin{pmatrix} u_r \\ v_r \\ 1 \end{pmatrix}$ are the coordinate vectors of perspective projection of P on the image.

$\hat{X}_l$ and $\hat{X}_r$ are related by rigid motion equation as

$$\hat{X}_l = R_{lr}\hat{X}_r + T_{lr}$$

$$U_l Z_l = R_{lr} Z_r U_r + T_{lr}$$

$$\begin{bmatrix} U_l & -R_{lr}U_r \end{bmatrix} \begin{bmatrix} Z_l \\ Z_r \end{bmatrix} = T_{lr}$$

With each of two cameras, we get linear equations in unknown coordinates of P, which can be written as $AP = T_{lr}$ where $A = \begin{bmatrix} U_l & -R_{lr}U_r \end{bmatrix}$

where A is 3×4 matrix involving projection matrix M_l, M_r of the camera.

In order to find the best reconstructed 3D point, linear method minimizes the criterion

$\|AP - T_{lr}\|^2$ with respect to P.

This can be written as sum of squared error criterion which needs to be minimized.

$$J(P) = \|AP - T_{lr}\|^2$$

where a and k represent the samples and number of samples in A respectively.

The above equation can be solved by closed form solution based on

$$\Delta J = A^T (AP - T_{lr})$$

Setting the above to zero, we get

$$A^T AP = A^T T_{lr}$$

This provides a closed form pseudo inverse solution

X can be determined as

$$P = (A^T A)^{-1} A^T T_{lr}$$

where $A^T A$ is non-singular and $(A^T A)^{-1} A^T$ is pseudo inverse of A

Given the 3D points, measurement error can be calculated as follows.

$$\%Measurementerror = \frac{abs(estdist - actdist)}{actdist} \times 100$$

The 3D measurement results for the points selected in Figure 2 are summarized in Table.1 The mean error is 4.2895%.

Points	Actual Dist (mm)	Estimated Dist(mm)	3D Measurement Error %
(P1,P2)	64± **0.5**	65.7198	2.6872
(P1,P3)	28± **0.5**	30.0682	3.2316
(P4,P5)	56± **0.5**	56.8278	1.2934
(P5,P6)	28± **0.5**	26.8777	1.7536
(P6,P7)	54± **0.5**	63.6137	15.0214
(P8,P9)	22± **0.5**	20.8802	1.7497
Average Error			4.2895

TABLE.1. DISTANCE OF SELECTED POINTS IN PIPE

III. DISTANCE WITH RESPECT TO PLANAR SURFACE

A plane can be defined just using 3 non-collinear points. The user is required to select 3 non-collinear points in the stereo images in order to obtain the plane (refer Figure 4).

Figure 4 Noncollinear points selected in Pipe

The system of equations $(ax + by + cz + d = 0)$ with the selected points can be solved using Cramer's rule.

Let three non collinear points of 3D data be $x_1, y_1, z_1, x_2, y_2, z_2$ and x_3, y_3, z_3. Then, the parameters of plane can be obtained as

$$\theta = \tan^{-1}(b/a)$$

$$\phi = \tan^{-1}(-\cos(\theta)./a)$$

$$\rho = c \times \sin(\varphi)$$

where a, b, c are calculated as follows

$$a = \left(\frac{-d}{D}\right) \times \begin{vmatrix} 1 & y_1 & z_1 \\ 1 & y_2 & z_2 \\ 1 & y_3 & z_3 \end{vmatrix}$$

$$b = \left(\frac{-d}{D}\right) \times \begin{vmatrix} x_1 & 1 & z_1 \\ x_2 & 1 & z_2 \\ x_3 & 1 & z_3 \end{vmatrix}$$

$$c = \left(\frac{-d}{D}\right) \times \begin{vmatrix} x_1 & y_1 & 1 \\ x_2 & y_2 & 1 \\ x_3 & y_3 & 1 \end{vmatrix}$$

Where D is determinant of the 3D data and $d = 2$

Figure 5(a). Selected Points in Pipe (Left View)

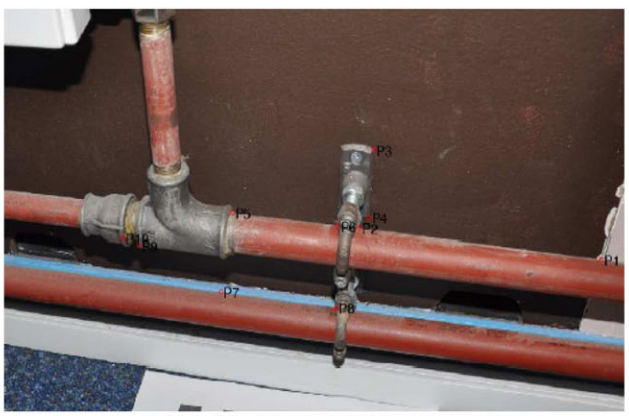

Figure 5(b). Selected Points in Pipe (Right View)

As provided in Table 2, the average error of distance between points selected in Figure 5 and the plane obtained using three non collinear points is 6.5988%. At the cost of around .5% more error than that of using automatic plane detection algorithm [1,4,5], this method is preferable and faster since it needs only 3 points selection rather estimating automatic disparity (SIFT[7], SURF[8]) which relatively takes longer time.

		Manual Selection	
3D Points	**Actual (mm)**	**Manual Selection**	**Error (%)**
P1	225	189.0557	15.1664
P2	216	223.5899	3.2025
P3	237	256.3304	8.1563
P4	176	192.6959	7.0447
P5	216	221.1379	2.1679
P6	230	234.2832	1.8073
P7	136	184.2114	20.3424
P8	160	159.3372	0.2797
P9	210	194.1538	6.6862
P10	213	210.3114	1.1344
Average Error			6.5988 %

TABLE.2. DISTANCE OF SELECTED POINTS IN PIPE WITH REFERENCE TO PLANE

IV. DMU BASED MODEL GENERATION

A. *DMU based knowledge*

The semantic information is used for building the part primitives with exact object component. 3D cloud is segmented using metadata knowledge where information such as color, location and shape class labels etc., are available. The 3D cloud of points need to be compared and fitted with DMU (Digital Mock–Up) model shape primitives thereby enabling further discrepancy analysis.

Model based matching is based on fact that whole object is a transformation (projection) of a preconceived model, or else it can be broken into parts that are. There exists numerous literature for 3D model matching, however the work which is close to our research is Georgeli et al. 2007., The authors [2] propose augmented reality solution for discrepancy check for identifying the differences between the planned 3D model and built items. Initially, anchor–Plates are used as reference information to obtain the pose in the coordinate system of the 3D model. Once pose is obtained, an augmented CAD is created by positioning the image into the 3D view. Upon positioning, a transparency level is used to view the deviation which is done using 2D information. However, we use 3D information from multiview images and we use model knowledge to perform discrepancy analysis in 3D space.

B. *Geometry model generation*

Geometry primitive are generated for each of the class labels available from the prior knowledge model representation. The sample generated primitive for a rectangular prism, pyramid and cube is shown in Figure 6.

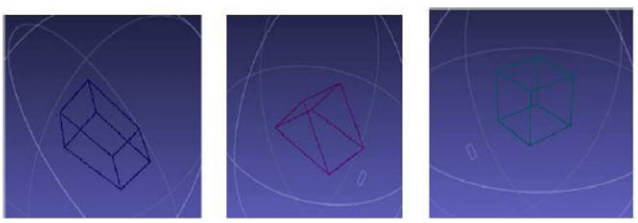

Figure 6. Generated Geometry Primitives

V. DISCREPANCY CHECKING AND ANALYSIS PROCESS

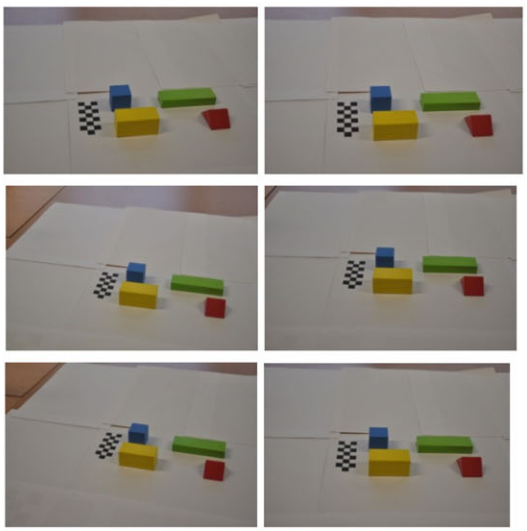

Figure 7.Sample Multiview Images

In this framework, we use calibration information to a) estimate camera pose information and b) perform model alignment. A 3D model of the environment is obtained using a Patch-based Multi-view Stereo algorithm [6] by Furukawa et al 2009. In order to get more accurate parameters, we use automatic calibration pattern recognition instead of bundle adjustment using automatic correspondences. In order to align the whole model with the cloud, we can use either a calibration pattern or one of the objects in the environment as a datum.

A. *Pose Estimation*

In order to perform the projection, we need to know the pose information of the objects present in the environment. Given the reconstructed computer vision Model of the Datum shape (MD) and Model of the Geometry shape (MG), the problem we solve is to minimize the difference between clouds of points and find the best alignment of MD with MG to obtain the pose information. This problem can be formulated based on least square criterion. The points are associated by nearest neighbor criteria and transformation parameters are estimated using a mean square cost function. We use the ICP (Iterative Closest Point) algorithm [9] for estimating this transformation matrix and it is fed to the discrepancy checking module for deviation analysis of the installation environment.

Let M be the reconstructed CV model of the datum shape and $M^{'}$ represent the geometry model shape. $\{m1_i\}$ and $\{m2_i\}$ represent the point sets of models.

$$M = \{m1_i\}_{i=1}^{N1} \text{ and } M^{'} = \{m2_i\}_{i=1}^{N2}$$

This problem can be formulated based on least square criterion as follows.

$$\min_{R,Tj\in\{1,2..N_2\}} \sum_{i=1}^{N1} \left\| Rm1_i + T - m2_j \right\|$$

where $R^T R = I_m$ and $|R| = 1$

where R and T are rotation and translation paramete
The two main steps of ICP algorithm are as follows.

The correspondence between two point sets M and based on $(p-1)_{th}$ rigid transformation are achieved as

$$cp(i) = \arg\min_{j\in\{1,2..N_2\}} \left\| R_{p-1} m1_i + T_{p-1} - m2_{j(i} \right.$$

The rotation and translation parameters are obtain minimizing squared distance

$$(R_k, T_k) = \arg\min_{R^T R = I_m, \det(R)=1} \sum_{i=1}^{N1} \left\| Rm1_i + T - m2 \right.$$

the set of points of the given argument for which the va the given expression attains its minimum value. The ob R and T transform the CV model to the geometry mod order to transform from geometry to CV model, the paran such as $R^{'}$ and $-T^{'}$ can be used.

B. *Point Cloud Segmentation*

Since we know the semantic metadata description reg each of the objects such as color, position, and class lab use it as key information to aid segmentation. For exam this setup, each object has distinct color information, wh highly useful in discriminating between those object hence we use segmentation based on color palette inform The location information can be used to localize the s space of the model within the vicinity. The supervise based (R,G,B) color segmentation is used [1].

Pseudo code:

1.*Input* : $3D \quad po\,\text{int}\,s(d)$

2.*for* $\quad i = 1 : size(d,1)$

3.*if* $\quad d(i,indR) <= rh \,\&\, d(i,indR) >= rl \,\&\, ...$
$<= gh \,\&\, d(i,indG) >= gl \,\&\, ... d(i,indB)$
$d(i,indB) >= bl$

4.*extract* $\quad d(i,:)$

5.*end*

6.*Output* : $\quad Segmented \quad cloud\,based$

The cloud segmented based on color palette informat

shown in Figure 8.

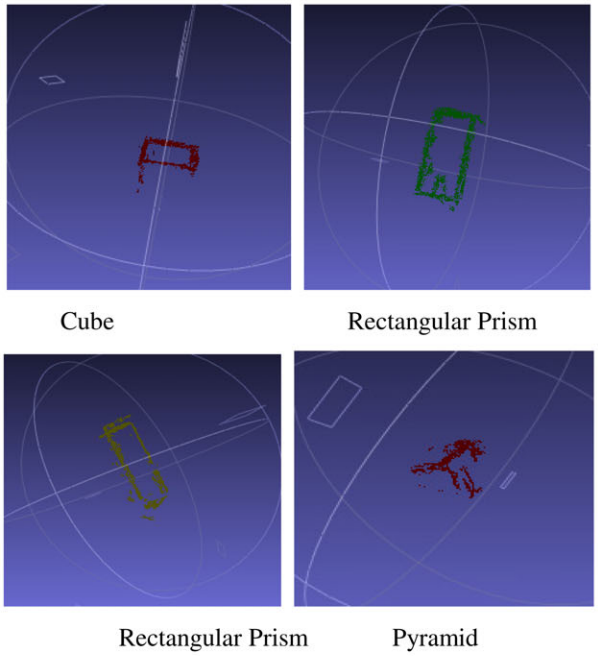

Figure 8. Segmented color clouds

If the segmented cloud still contains outliers, post processing is done using component analysis to get reliable segmented cloud. The algorithm for connected component analysis is as below.

1.*number of points* $(N = 100)$
2.*minimum distance threshold* $(m = 0.5cm)$
3.*find the distance between eachpoint*
4.*Create list for labels of the points*
a vector of size N. Label all to -1.
set label_counter $= 0$
5.*loop* :
6.*find* $\min$*imum dis*$\tan$*ce in matrix*
indexes i and j
if $\min$ *dist* $>$ *m stop*
7.*check the labels of both*
8.*if they have no labels set their labels*
to label_counter and increment labelcounter
9.*if one of them have a label, set*
the other one with the same label.
10.*if they both have labels, choose label*
with smaller label set the other to the
smaller label
11.*replace the other label with smaller*
one in label vector
12.*go to* 5

C. Pose estimation of the Individual objects

For each of the segmented object and corresponding geometry primitive, pose $P_i\{i = 1 : S_n\}$ is recovered using method discussed earlier. S_n is the number of segmented objects. This transformation matrix is used to project geometry primitives onto the 3D digital reconstruction. We use a single pose recovered from the whole system and a pose for each of the object in a system so that the entire system is available.

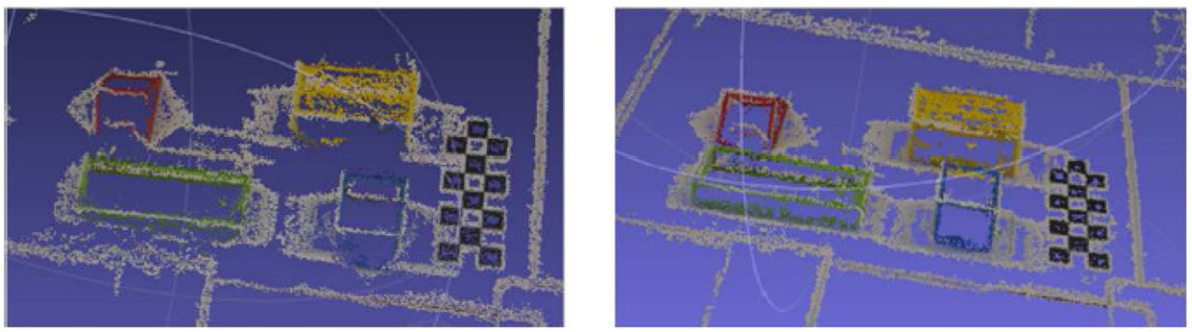

Figure 9-1 Original and Blue shifted cloud

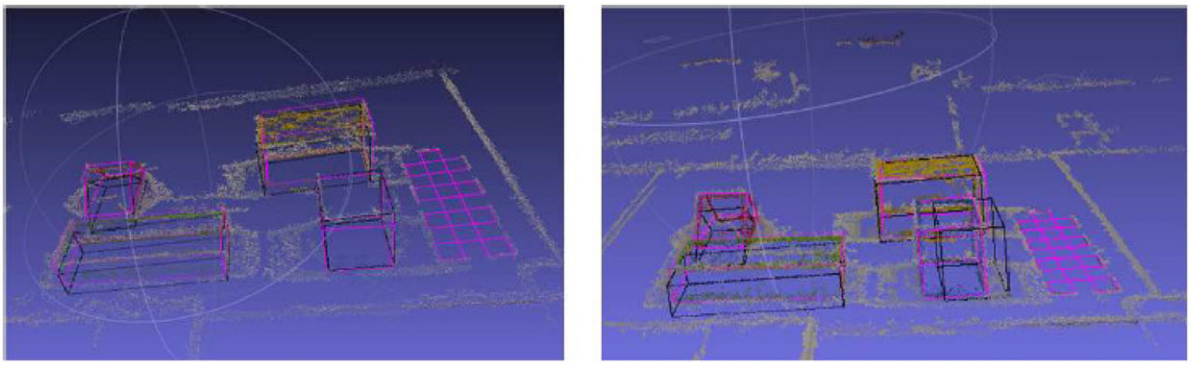

Figure 9-2 Original Fitted and Blue shift Fitted cloud

Class	X	Y	Z
Cube	0.0597	0.0165	0.0997
Rectangular Prism1	0.0061	0.0315	0.5877
Rectangular Prism 2	0.6549	0.2610	0.0746
Triangular Prism	0.2232	0.1043	0.8892

Set (A)

Class	X	Y	Z
Cube	0.0663	0.9556	0.1275
Rectangular Prism1	0.3401	0.0435	0.4443
Rectangular Prism 2	0.1190	0.2941	0.0225
Triangular Prism	0.4288	0.0945	0.7117

Set (B)

TABLE.3 DIFFERENCE BETWEEN CENTER OF OBJECTS ALIGNED BY ICP AND CALIBRATION LOCATION

The original (SetA) and blue shifted cloud (SetB) used for experimentation is shown in Figure 9-1. We use single pose recovered from the whole system and pose for each of the object in a system so that entire system is available. The model and CV cloud aligned using the pose information is shown in Figure 9-2. It can be clearly seen that the shift of 1 cm in blue cube is visible. This deviation from the model would be useful for automatic verification analysis. The difference between the center of the objects aligned by ICP and aligned by calibration location for both normal(Set A) and blue shifted(Set B) cloud is provided in Table 3.

V. CONCLUSIONS

In this paper, we presented a new 3D vision based auditing framework which uses safety engineer input and CATIA model knowledge information. Firstly, we showed that distance between any points in a given installation environment with or without planar surface reference can be measured. Secondly, we provided a novel model matching strategy that uses input from digital camera and semantic metadata knowledge available from geometry models which can be used for verification tasks. The discrepancy analysis of CV model with DMU is demonstrated. A novel framework constituting the various algorithms for achieving the model matching and discrepancy analysis is presented with results. Ideally, the framework acted as proof of concept for safety analysis and verification and has been tested in a controlled environment dataset for model matching. 3D object structures with respect to other objects position in the scene can be extracted. In future, experiments would be conducted in real industry setup.

ACKNOWLEDGMENT

Our thanks to Dr. Chris Papadopoulos for his help throughout the project.

REFERENCES

[1] K.Vaiapury, A.Aksay, X.Lin, E.Izquierdo, C.Papadopoulos, A Vision Based Audit Method and Tool that Compares a Systems Installation on a Production Aircraft to the Original Digital Mock-Up, with a Focus on Safety Driven Installation Constraints, such as Segregation, Proximity and Orientation, *SAE 2011 AeroTech Congress & Exhibition*, 2011.

[2] P.Georgeli, P.Schroederi, S.Benhimanei, S.Hinterstoisseri, M.Appel, N.Navab, An Industrial Augmented Reality Solution For Discrepancy Check, *Proceedings of the 6th International Symposium on Mixed and Augmented Reality*, 2007.

[3] E.Izquierdo and J.R.Ohm, 2000, Image based rendering and 3D Modeling, A complete framework, *Signal processing: Image Communication*, Vol.15, Issue 10, pp. 817-858, 2000.

[4] F.T.Kurdi, T.Landes, and P.Grussenmeyer, Hough Transform and extended RANSAC algorithms for automatic detection of 3D Building Roof Planes from LIDAR data, *International Archives of Photogrammetry, Remote Sensing and Spatial Information Sciences*, ISPRS, Volume 3, Issue Part 3/W52, p.407-412,2007.

[5] R.Schnabel, R.Wahl, R.Klein,Efficient RANSAC for Point-Cloud Shape Detection, *In Computer Graphics Forum*, pp.214-226, 2007.

[6] Y.Furukawa and J.Ponce, Accurate, Dense, and Robust Multi-View Stereopsis, *IEEE Transactions on Pattern Analysis and Machine Intelligence*, 2009.

[7] Lowe D. G, Distinctive Image Features from Scale-Invariant Keypoints, *International Journal of Computer Vision*, 60, 2, pp. 91-110, 2004.

[8] Herbert Bay, Andreas Ess, Tinne Tuytelaars, Luc Van Gool, SURF: Speeded Up Robust Features, *Computer Vision and Image Understanding (CVIU)*, Vol. 110, No. 3, pp. 346--359, 2008.

[9] P.J. Besl and N.D. McKay. 1992. A Method for Registration of 3-D Shapes. *IEEE Transactions on Pattern Analysis.and Machine. Intelligence*, Vol.14, Issue 2, ,pp. 239-256, February 1992.

Karthikeyan Vaiapury has obtained BTech (Information Technology) from School of Engineering and Technology, Bharathidasan University (currently Anna University,Trichy), India and M.S (Computer Science) from National University of Singapore, Singapore in 2003 and 2007 respectively. He has worked as software engineer (R&D) at Mahindra Satyam, Singapore for 2 years.He has also worked as Lecturer at the School of Engineering and Technology, Bharathidasan University from Oct 2003 to Dec 2004. Currently, he is a PhD student at Queen Mary, University of London, working on Model based 3D Reconstruction and Recognition using multiview stereo images.

Dr.Anil Aksay received the B.S., M.S and Ph.D degrees in Electrical and Electronics Engineering, from Middle East Technical University, Ankara, Turkey in 1999, 2001 and 2010, respectively. His research interests include image, video and 3D coding, streaming, transmission.

Dr. Xinyu Lin graduated from University of Central Lancashire with BSc (Hons) in Electronics in 1997. He continued his graduate study in the same University and earned PhD degree in image compression in 2004. Currently he is a post-doc researcher in Multimedia and Vision Group in Queen Mary University of London. His research interests include computer vision, medical image processing and object oriented software development.

Prof.Ebroul Izquierdo (M'95–SM'03) received the B.Sc and M.Sc degrees in applied maths from Humboldt University, Berlin, Germany, in 1987 and 1989, respectively. He received the Dr. Rerum Naturalium (Dr.rer.nat) degree for his thesis on the numerical approximation of algebraic-differential equations in 1993 from the same institution. From 1990 to 1992, he was a Teaching Assistant with the Department of Applied Mathematics,Technical University Berlin, Berlin, Germany. From 1993 to 1997, he was an Associate Researcher with Heinrich-Hertz Institute for Communication Technology, Berlin, Germany. From 1998 to 1999, he was a Senior Research Officer with the Department of Electronic Systems Engineering, University of Essex, Essex, U.K. Since 2000, he has been with the Department of Electronic Engineering, Queen Mary, University of London, London, U.K., where he is currently the Chair of Multimedia and Computer Vision and the Head of the Multimedia and Vision Research Group with the Department of Electronic Engineering and Computer Science. He has been involved and coordinating several large European research projects over the last 12 years. He has published over 300 technical papers, including different chapters in books. His current research interests include video coding, video analysis, and visual information retrieval. Dr. Izquierdo is an Associate Editor of several journals in the field of multimedia signal processing, including the IEEE Transactions on Circuits and Systems for Video Technology (TCSVT) and the EURASIP Journal on Image and Video Processing. He has served as a Guest Editor of three special issues of the IEEE TCSVT, three special issues of the Journal Signal Processing: Image Communication, two special issues of the EURASIP Journal on Applied Signal Processing and Image and Video Processing, and several special issues in other journals in the same field. He is a Chartered Engineer, a Fellow Member of the Institution of Engineering and Technology, and a Member of the British Machine Vision Association. He has chaired and co-organized several conferences and workshops in multimedia communications, visual information retrieval, and coding technology.

Event-based media organization and indexing

(Invited Paper)

Riccardo Mattivi
University of Trento/Department of Information Engineering and Computer Science, Trento, Italy
Email: rmattivi@disi.unitn.it

Giulia Boato and Francesco G. B. De Natale
University of Trento/Department of Information Engineering and Computer Science, Trento, Italy
Email: {boato, denatale}@ disi.unitn.it

***Abstract*—As highlighted in the recent literature, *events* may provide important information to associate content and context for media indexing and retrieval. Nevertheless, a thorough implementation of such concept into viable applications is still lacking, due to the difficult in defining a suitable representation of events but also in producing effective automatic tools to create and instantiate event structures. In this paper we give an overview of the existing work in the field and we present a showcase in which event structures are exploited to better organize and access personal media contents, allowing to automatically detect events and sub-events in photo collections and annotate media accordingly.**

***Index Terms*—multimedia retrieval, events and sub-events recognition, photo collection organization.**

I. INTRODUCTION

In the last years, the ever-increasing use of digital compact cameras allowed producing an enormous amount of multimedia contents. Nowadays, people use to capture the most important moments of their lives with pictures and videos and to store them on their pc, on mobile devices, or on social networks. This last instrument is also becoming the most popular solution to share a wide variety of multimedia information among individuals and groups. For a single user there is a clear link between such contents and their own experiences (e.g., their last holiday, their kids playing softball, the wedding of their best friend) and this is the most natural way of indexing their contents (e.g., "Winter 2010 Italy" or "Bob's Wedding"). Indeed, recent studies in neuroscience have demonstrated that humans remember their life using past experience structured into events [1].

Our life is a constellation of events that, one after the other, pace our everyday activities and index our memories. A birthday, a marriage, or a summer vacation, are the lens through which we see and memorize our own personal experiences. Global events, such as world sport championships or global natural disasters or, on a smaller scale, a local festival or a soccer match, build collective experiences that allow us to share personal experiences as part of larger phenomena that we could call collective events. Events can therefore be used as the primary means for organizing and indexing media (e.g., photos, videos, journal articles), but also to share them (e.g., through social networks).

The typical approach to content-based media retrieval is to start from media and trying to extract information (descriptors) that helps understanding their content. Event-based analysis provides a way to reverse this approach, making events become the main key for organizing our memories and media an attribute of such memories, which represent our experience of that specific event. Events have a local dimension, which allows for a local mapping between tags and the personal experience, as represented in the data, thus making easier and doable understanding media contents. At the same time events have also a global dimension, in a twofold sense: first, the semantic of an event has a common ground for the peers involved in it, thus providing a way for sharing a specific event among involved people; second, events of the same type (e.g., weddings) share similar structures, in the sense that it is usually possible to identify a more or less standard sequence of episodes that characterize that specific event type (e.g., ceremony, group pictures, banquet), thus providing a way of sharing events of the same type within user communities.

From the user's viewpoint, organizing and indexing photo collections through events may be beneficial, as it allows accessing their data in a natural and intuitive way. Furthermore, on this basis it is possible to develop powerful facilities to support users and communities in media management. As an example, let imagine a family coming back home from a winter holiday on the snow. At present, they would most probably download their photos from the camera to the pc and store them in a folder, perhaps with some manual annotation. An event-based indexing tool, exploiting a suitable model for that type of event, may automatically provide a structuring and labelling of the media collection with appropriate tags, sub-event recognition (e.g., skiing, taking a break, shopping, etc.), and possibly adding information on time, geographical location, people involved, and so on. This will be useful at a later time to retrieve their data based on multiple keys, or to match similar events (e.g., the previous year holyday), or to share it with friends that participated to the same event.

In this paper we overview the state of the art on event definition and recognition, by first describing basic image analysis tools exploited for this purpose (Section II), and then detailing the structure of events and various application scenarios where such a concept can be exploited (Section III). Section IV presents some results of automatic organization and classification of images based on three types of structured events (graduation, marriage, ski holiday), while Section V draws some concluding remarks.

II. IMAGE ANALYSIS TOOLS FOR EVENTS

In this section, we will review the basic existing tool for image analysis, which are extensively used in the techniques described in the following sections for event detection and recognition.

The question is: what kind of information a picture can provide? First of all, nowadays cameras or smartphones store a lot of useful information in the form of standard EXIF data[1]. According to the device capabilities, such data may include date and time, camera settings - such as camera model, shutter speed, aperture, focal length, ISO settings - thumbnail information (for image preview in file managers or on the camera), but also GPS-based geo-location information, if available. In addition to this, the picture itself carries a lot of information in its pixel data, which can be analysed and exploited. In the last decades several global features were studied: colour histograms [2][3], which provide an estimation of colour distribution in images; invariant features [4][5], which are features invariant with respect to certain transformations; texture features and high-order moments, which give information about the relationships among neighbouring pixels. Among texture features, Gabor features [6] computed as the result of a set of Gabor filters at different scale and direction have been widely used in this context. Tamura features [7] have been used as well, for their ability to mimic the human visual perception in terms of coarseness, contrast and directionality.

In 2001 the MPEG7 group defined a standard set of visual descriptors [8] that describe the visual content in terms of colour (five tools to compute colour distribution in a single image and colour relations into sequences of images), texture (three tools that describes the region homogeneity and edge histograms), shape (three tools to describe contours, regions or shapes after a segmentation phase), and motion (several algorithms that describe the motion in video sequences).

Colour and Edge Directivity Descriptor (CEDD) features [9] represent a compact set of colour and texture statistics, which can be exploited in large image databases or in video segmentation [10]. GIST descriptor [11] aims at describing real world scenes bypassing the segmentation and the processing of individual objects or regions and it is based on a set of Gabor filters evaluated at different scales and at different orientations.

Although the typical approach is to calculate such descriptors on the entire picture, thus providing a unique representation of the whole image, it is also possible to compute them in particular regions of the image, corresponding to some visual object or simply to a sub-block. In the following we detail local descriptors, which are widely used for media content characterization.

Scale-Invariant Feature Transform (SIFT) algorithm [12] collects features in interesting parts of the image. In its original version, SIFT detects some interest points in an intensity image, extracts a region around them and describes the relevant content. The features computed with this technique are invariant to translation, rotation and scale and have been widely used for different purposes such as image stitching, object recognition, wide line matching, and robotic mapping. In the last years several modifications have been proposed, such as the extension to several colour spaces [13], different method for computing the description of local patches [14], or fast approximations for the computation of both localization and description of interest points in the so-called SURF algorithm [15]. Recently, a fast and dense computation of local features has been proposed in [16], which outperforms previous methods for object and concepts recognition.

Once visual features are obtained from raw pixel values, further steps are required to obtain more information for retrieval, recognition, or other goals. An adage says, “A picture is worth a thousand words”. What about a group of pictures? Several clustering algorithms exist in literature whose aim is to gather photos into clusters exploiting time, geo-location, similarity of visual content, or tag information. The k-means algorithm [17] finds k clusters based on the distribution of data in the feature space. Several modifications have been proposed, such as approximate k-means [18] or hierarchical clustering [17]. Grouping of pictures can be done also by analyzing distances inside a matrix that represents the distances between each feature vector [19], by applying probability latent semantic analysis to feature vectors [20][21], or by applying dominant sets [22].

In the following section, these basic tools will be used for image clustering and event recognition purposes.

III. EVENTS AND EVENT RECOGNITION

Event recognition is a term widely used in computer vision and image analysis, which encompasses several phases in the process of data interpretation, from the recognition of actions in video sequences [1][23], to the characterization of behaviours [24], the detection of specific situations [25][26][27], the recognition of activities from single images [28]. An event, with all the attributes that will be described later in this section, can be considered as a point in a multi-dimensional space, where each dimension brings a different facet of such a complex entity. This representation highlights the diversity that is inherent the concept of event, and includes the notions of time, space, activities, actors, emotions, etc. Photos and videos (among other media) depicting an event can be regarded as additional sources of information, or the “experiential” dimension of the

[1] www.exif.org

event. The concept of diversity in itself is gaining special attention in information retrieval, as witnessed by the recent developments of search engines such as Yahoo! and Google, and the big investments in research (see, e.g., the EU FET IP Project LivingKnowledge and related references [29]).

If one thinks to the typical way an event in one's life is recalled, typically the above dimensions are explored in our memories answering simple questions such as: where (place), when (time), who (people involved), what (type of event), how (various attributes that characterize the event). Once localized the event, people typically search for the relevant photo albums, if available, to refresh the visual memory of the event. Accordingly, the pioneering work by Westermann and Ramesh [30] defines an event model as characterized by the following aspects/axis:

Temporal: events are strictly related to the concept of time; this information is easily stored in the time stamp of multimedia content and it can be absolute or relative to a previous event.

Spatial: an event occurs in a geographic area, usually captured by a GPS receiver, or even in a region of interest of a picture.

Informational: the event model should provide additional information about the involved actors and the involved entities: this information can be taxonomically organized.

Experiential: since the event model is applied to multimedia applications, the model should support connections to different media contents and should provide the users with an easy way to explore them.

Furthermore, events can be linked each other by several types of relationships. For instance, an event may be the cause of another one, or may simply precede or follow it. An event can be also part of another larger event (thus leading to the concept of event granularity). On this basis one can define the following relational attributes to an event:

Structure: event models may apply at different levels of abstraction and granularity (e.g., sub-events, similar events, etc.).

Causality: an event model should support the description of cause-effect relationships.

This structure allows a flexible collection and management of all information, data, and multimedia contents connected with a certain event. In the following subsection we describe how such different aspects can be analysed and exploited for event-based media organization and indexing.

III.A Event detection and event-based organization

The problem of recognizing events from visual data inherits researches from recent years in the field of scene, object and landmark recognition. In the following, a brief survey on these methods is given, relying on the basic tools described in the previous section, with references and focus on the event recognition task.

Figure 1. Sports and social events. From top to bottom baseball, cycling, figure skating, meeting, pic-nic, mountain trip, ski-holiday (skiing and bar-relax sub-events), wedding (celebration and group-pictures sub-events), graduation (ceremony and group-pictures sub-events)

In early works, image retrieval and image recognition has been achieved by solving simple tasks, such as distinguishing between indoor and outdoor images [31], or retrieving images looking at their textures and colour histograms [32]. In [11], Oliva et al. developed a holistic method to recognize real world scenes built upon the GIST descriptor, while in [33] GIST descriptor was also used for automatic discovery of image families. In the last decade, methods inspired by local features (mainly SIFT) have gained particular attention by the research community. The most common approach is the Bag of Words (BoW) representation. This method was originally developed for text retrieval: a document, a sentence or a simple text is represented as a collection of words, disregarding the word order and the grammar, and the word frequency count is used for retrieving or classifying documents. Similarly, in the image domain, an image is represented as an unordered collection of "visual words", disregarding the spatial layout. Such visual words are smart conversions from samples of local regions as computed by the SIFT algorithm [12], and their frequencies in an image are then used in the

classification. Such a model has been used for object recognition [34], scene recognition [34], and human action recognition [35][23].

More specifically for event recognition, Li et al. in [36] classify sport events in single images by fusing object and scene recognition. For instance, a rowing competition is recognized by the presence of a given scene (e.g., a lake) and some typical objects (e.g., boats, athletes, etc.). Thus, event recognition is achieved taking into consideration as much semantics as possible in the image interpretation. In [37], Jiang et al. exploit local visual features by building a 21-concept space instead of dealing with a higher dimensional low-level feature space. Rasiwasia et al. in [38] propose a similar approach to classify events in an intermediate space, by exploiting a low dimensional semantic theme for image representation. Indeed, each theme induces a probability density on the space of low-level features, and images are represented as vectors of posterior theme probabilities, thus reducing the computational time both for training and testing phase. In [39], Imran et al. mine a set of pictures belonging to specific events and describe it as a histogram of word occurrence, using the BoW approach. They try to discover the most informative features of different events using the PageRank technique, achieving a small increase in the performance. Das et al. in [40] investigate the use of high-level visual and temporal features and determine a subset of features that provide good correlation with the event class.

More recently, Lin et al. in [41] build a framework for vision-assisted tagging of personal photo collections using people, events, and location information. They exploit a probabilistic model of context that couples the multiple domains through a set of cross-domain relations, where each relation represents the probability of co-occurrence in two domains. In [28], Tsampoulatidis et al. represent images and videos as vectors of responses given by a high number of trained visual concept detectors. The high-dimensional vector in the concept-space is then analyzed with a subclass discriminant method for identifying the most appropriate concept subspace to detect and recognize the target event. A novel method for fast and robust event detection is introduced by Dao et al. in [42]. The key idea is to define and extract a unique signature from a set of photo albums related to a given event category. The event type of a new photo collection is then given by the classification of its signature.

Usually, image annotation systems consider a single photo at a time and label the photos individually. However, as highlighted in [42], collections of personal photos contain information that could be exploited at a global level. In recent years, automatic clustering of digital photo sets has received increasing attention and picture timestamp information is one of the most exploited features to achieve this task (see Graham et al. [43]). Together with time information, content-based features have also been used to build systems able to summarize photos into events: Cooper et al. [19] present a multi-scale temporal and content similarity clustering to define salient moments in a digital photo library, while Lim et al. [44] summarize collections combining content and time information and use predefined event taxonomy to annotate new photos.

Space information, ever increasingly available in terms of GPS coordinates or geographic landmarks, is also relevant data that can be exploited to browse and organize picture archives. For instance in [45], Jaffe et al. present different frameworks for generating summaries of geo-referenced photographs with map visualization. In [46], Cao et al. make use of the contextual information naturally provided by the associated GPS position and time metadata in a collection of pictures. They first employ a constrained clustering algorithm to partition a photo collection into event-based sub-collections, taking into consideration both time and place. Then, a conditional random field is used to model the correlation among photos, based on time-location constraints and on the relationship between collection-level annotation (i.e., events) and image-level annotation (i.e., scenes). Another approach for exploiting the geo-location information is introduced by Yuan et al. in [47]. They mine informative features derived from traces of GPS coordinates and from the bag of visual words. Such features are based both on the entire collection and on individual photos. In [48], Luo et al. exploit the photo location in a different way: they obtain satellite images corresponding to the picture position and investigate a novel use of these data by recognizing the picture-taking environment, as if the picture taking activity has been seen by a third eye above the user. Moreover, they combine this inference with classical vision-based event detection methods and they study the synergistic fusion of the two approaches.

In the next Section we propose a novel methodology for event and sub-event detection and recognition, which exploits content-based features and EXIF data to support the user in photo album management and annotation.

IV. EVENT-BASED PHOTO COLLECTION MANAGEMENT

As a proof of concept, we propose here a completely automatic recognition system able to discover events from a collection of pictures and able to suggest a structure according to the relevant sub-events. A preliminary version of this approach was proposed in [49].

The system works as a cascade of classifiers, as follows:

Event level: the system first classifies a given photo album into “social” or “sport” event (binary classifier) and successively labels it more specifically according to given macro-category (see events description in Table 1).

Sub-event level: on the basis of the detected event type, a further understanding of users' activities is conducted and a deeper analysis is performed in order to recognize all sub-events present in the image collection (see examples of sub-events recognized for social events in Table 2).

The cascade of classifiers supports events and sub-events discovery from general information to a more specific one. As an example, a photo album depicting a

wedding is first classified as belonging to social class, successively to wedding class and further on its specific moments are classified as ceremony, group-pictures or other sub-event types.

In the following we provide details of the dataset used, the experimental setup and the obtained results.

IV.A Dataset

In the literature, different datasets have been collected and made available to the research community for testing and comparing different algorithms, such as action recognition [50][51], object recognition [34], scene recognition [52]. Unfortunately, this is not the case for event detection from media where, to the best of our knowledge, no extensive corpora have been made available so far. Although many social networks are used to share event-related media among private users, no publicly available datasets contain consistent event-related tagging. In [40] and [47], authors use databases obtained from several users spanning different events, but not available to the community. Recently, MediaEval benchmarking initiative for multimedia evaluation [53] has released a dataset for social event detection (limited to testing purposes), where images are crawled from Flickr with associated tags and time data.

Due to the increasing interest in this field of research, we initiated the collection of an event-based image database, which consists of two different event families: sports and social events. Within them, we selected several event types, as reported in Table 1. The pictures of our database were downloaded as entire album collections from PicasaWeb Album service and manually labelled at the image level. For some specific social events that show a quite well defined structure (Graduation, Wedding, and SkiHoliday), we further manually labelled each image with sub-event classes as specified in Table 2 and some of them are shown in Figure 1. We define as event-albums a collection of pictures spanning one event and collected from one user.

Table 1. Event classes for social and sports events

Main event	*Event-albums classes*
Social events	Concert, Graduation, Wedding, Meeting, Mountain Trip, Pic-nic, Sea Holiday, Ski Holiday
Sport events	Baseball, Basketball, Bike, Cycling, F1, Golf, Hockey, Rowing, Figure Skating, Swimming

Table 2 Sub-event classes for some social events

Social events	*Sub-event classes*
Wedding	Group pictures, ceremony, party-eating, unknown
Graduation	Group pictures, celebration, party-eating, unknown
Ski-Holiday	Skiing, walking in the town, eating at hotel, eating. relax during skiing, partying, unknown

IV.B Experimental Setup

We make use of time information from EXIF data and visual information following the pipeline of Uijlings et al. [16]. We densely extract RGB-SIFT features, we project the descriptors with a Random Forest and finally we use Support Vector Machines (SVM) with histogram intersection kernel for classification. The codebook has been built on the Pascal 2007 database and has 4096 visual words. Such configuration results as the best tradeoff between accuracy and computational time. We proved in [49] this visual pipeline to be state-of-the-art in a standard sport event database.

We designed the system in two different ways:

- *Single-step classifier:* the system is trained with all social and sports event classes at once for the purpose of event recognition, and with all sub-events classes for the purpose of sub-event recognition. In this approach there is no previous discrimination between sports and social classes and no a-priori information about the event type being analyzed for the sub-event recognition phase.
- *Multi-step classifier:* the system is built as a cascade of classifiers working from coarse recognition to a more specific sub-class categorization. For instance, an event-album depicting a graduation ceremony is first classified as belonging to the social-event class, then to graduation, and finally to its specific sub-event types.

At the event level we followed two approaches for the recognition task:

- *Single image:* this approach provides the classification of single images, discarding event-related information, and represents the baseline for our comparisons.
- *Post processing - majority info:* since each event-album belongs to a single event, the event class label of each image is given by the majority of the single image event labels in the analyzed test instance.

Regarding sub-event analysis, several activities can be identified in a photo collection. Typically such activities are bounded in time. Therefore, the first step is to group the pictures into homogeneous clusters based on time information [19]. We exploit such information in two different ways: by applying post-processing algorithms on the single image classification output or by dealing with the visual features of each cluster as a whole.

- *Single image:* this represents the classification of single images taking in consideration only the visual information, regardless the belonging to a cluster.
- *Cluster BoW:* in this approach we exploit the information of the cluster in the classification phase. The signature of the cluster is obtained by averaging the BoW signatures of each image belonging to the cluster itself. The system is trained with the signature of single images, but tested with the signatures of the clusters. The label of the cluster is then assigned to each single image inside the cluster.
- *Post processing, median filter:* the result of the classification is filtered with a median filter with a fixed window size. The assumption is that successive

pictures belong to the same sub-event class. This method represents a baseline for the post-processing algorithm.

- *Post processing, cluster information:* the classification of images belonging to a cluster is given by the majority vote inside the cluster. The assumption is that pictures grouped into clusters belong to the same class. This method is similar with the approach used at the event level.

As our results are influenced by the reliability of the clustering algorithm to give homogeneous clusters, in the analysis of results we report the upper-bound as the classification achieved with the "post-processing, cluster information" method having the ground truth as test set (*post processing, upperbound*).

We conducted the experiments using the Leave-One-Out methodology: having *n* event-albums, we trained the system with *n-1* albums and we performed the tests on the remaining one. Such task is repeated for *n* times and the results are averaged over all tests. As metric of performance we use the f-measure, defined as $f=(2*P*R)/(P+R)$, where the precision P is defined as $P=(t_p/(t_p+f_p))$ and the recall R as $R=t_p/(t_p+f_n)$. In the previous formulas t_p stands for true-positive, f_p for false positive, and f_n for false negative. The results refer always to the classification of single images.

IV.C Results

1) Single-step vs Multi-step

We are first interested in comparing the single-step vs. the multi-step classification strategies for both events and sub-events. As can be seen in Figure 1, the SVM classifier trained with both sport and social events (18 classes in total) gives an average f-measure of 0.66. The multi-step classifier performs better, with an average of 0.73, at the cost of a slightly higher complexity (due to two step classification). More specifically, in the second case the first step of binary classification of the event-album into sports or social event classes gives an average f-measure of 0.91 for sports and 0.88 for social events. The application of a post-processing algorithm (as mentioned in the experimental setup and detailed in the following) allows recovering also the erroneous cases, thus achieving a perfect categorization of sport or social event class. The classification within each macro-class is achieved through a separate set of classifiers dealing with simpler problems (8 classes for social or 10 classes for sports. This results in an average f-measure of 0.81 for sport events classification and of 0.62 for social events.

The same effect is noticed for sub-events recognition within structured events (Graduation, Wedding and SkiHoliday): single-step classifier trained with all sub-events from the three social event classes provides an average f-measure of 0.58, while multi-step classifier yields an improvement of 0.14. Also in this case, the duty of the classifier is simplified, having a reduced number of sub-events to recognize. Table 2 shows the results obtained for sub-event recognition (single-step and multi-step labels).

We conclude that the exploitation of events at different granularity level helps improving the overall recognition results.

2) Exploiting time at the event level

We now use the time information to improve the results both at event and sub-event level. At the event level, we apply the post-processing - majority info method. We focus on the results of Figure 1 to show the f-measure for the sport and social classes for single image classification (in the figure named also as multi-step classifier) and for our post-processing algorithm as majority voting. First of all, we can see that the post-processing significantly outperforms the baseline for sports events with an improvement of 0.17 in the f-measure (thus achieving an almost perfect classification). As a matter of fact, the post-processing is able to correct the confusion between visually similar classes (see for instance Bike vs. Cycling vs. F1, Hockey vs. Figure Skating, Baseball vs. Golf) mainly due to similar environments (speed circuit, ice-hockey stadium, or grass) where only minor parts of the scene change.

Similar results are shown for social event classification. We score an f-measure of 0.62 as baseline (in Figure 1 named as multi-step classifier), while f-measure increases to 0.89 with post-processing majority voting. Also in this case we observe a larger confusion between images with similar environment or sharing similar activities (e.g., outdoor eating in pic-nic or mountain trip, or people standing in a large meeting room in graduations and meetings). However, the representative images for each class are mostly correctly classified. Thus, the post-processing helps in disambiguating the Mountain trip, Sea Holiday and Ski Holiday classes and a significative improvement is obtained for the Graduation class.

We can conclude that considerable improvements can be achieved over single-image classification by defining them as events and by using majority voting over the event-albums.

3) Exploit time at sub-event level

We now exploit time information at sub-event level, since an event-album may contain multiple sub-events. We compare the classification of single images (the baseline) with an approach that uses the signature of the entire cluster and two post-processing strategies. We also provide an upper bound measure about the quality of the clustering algorithm. All the results are summarized in Table 3.

We first evaluate the ability of the clustering algorithm to give uniform clusters. Results, named as *post processing, upperbound*, are shown in Figure 2. The upperbound for Graduation and Wedding is very high with an f-measure of 0.98 and 0.96 respectively. However, performance for the Ski-Holiday class is only 0.87, due to the confusion between bar-relax and skiing sub-events. This is explained by the fact that many pictures are taken before or after a break instead of directly in action, thus inducing errors in the time-based clustering.

Table 3 Values of f-measure for sub-events recognition obtained with different methods

Method	Grad.	Wedd.	SkiH.	Av.ge
Baseline	0.7406	0.7284	0.7017	0.7236
Cluster BoW	0.7564	0.7541	0.6726	0.7277
Post-median filter	0.7671	0.7807	0.6228	0.7235
Post-cluster info	0.7598	0.7631	0.7232	0.7487
Post-upperbound	0.9788	0.9568	0.8663	0.9340

The *post processing - median filter* helps by leveraging the sparse classification errors, thus performing better than the baseline approach for all classes. This method does not include information on the cluster borders, and therefore is prone to errors at the border of the sub-events. The Graduation gives an f-measure of 0.74 for the baseline and an increment of 0.02 is achieved with this method.

The *post processing - cluster info* method allows achieving better performances. The Graduation and Wedding classes reach the best performance of 0.77 and 0.78, respectively, while Ski-Holiday shows a slight decrease in accuracy, due to the aforementioned confusion in the clustering. This method is able not only to handle and correct sparse classification errors inside the cluster, but also at its borders, provided that the clustering is of sufficient quality.

Finally, we exploit cluster information with the *cluster BoW* method, which gives better results than the baseline but slightly worse than the post-processing cluster info method. Hence by using the cluster signature one can save computational effort at the expense of a small reduction in classification quality.

We conclude that the *post-processing - cluster info* is the best strategy to boost the classification accuracy of sub-events, if the quality of the cluster algorithm is sufficient.

Figure 2. Sub-event results for a Wedding class tested with an event-album from Flickr. From top to bottom: celebration, group pictures, group pictures, party-eating.

V. CONCLUSIONS

In this paper we proposed an overview of the existing research about event recognition and event-based media indexing, showing how "events" can boost the performance of conventional content-based retrieval systems, making it possible to conveniently associate content with context. Moreover, we demonstrated a possible application of this concept in the field of personal photo collection organization. In particular, we showed that event structures may be exploited to better organize and access personal media, by introducing events and sub-events recognition in photo collections and automatically providing album organization.

ACKNOWLEDGMENT

This work is developed within the GLOCAL Project, co-funded by the EU Research Framework Programme 7 under DG INFSO Networked Media Systems.

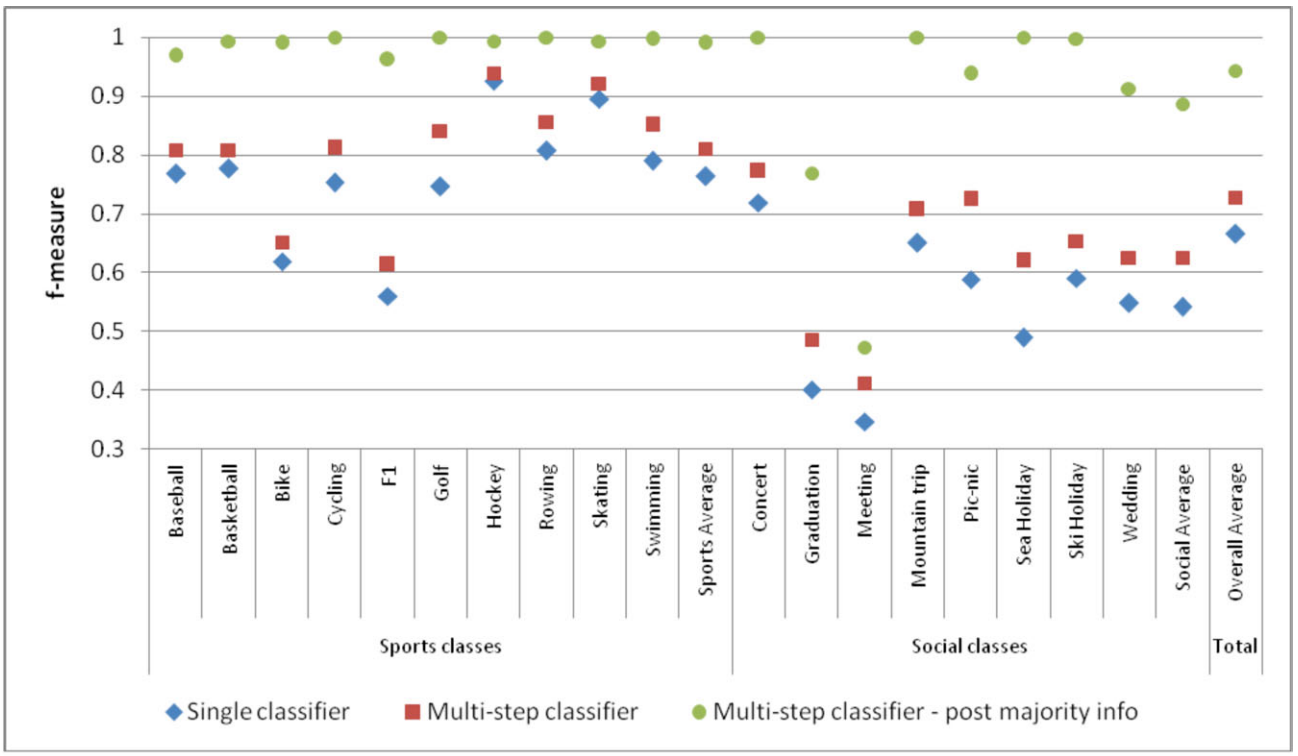

Figure 1. Events: Single classifier, Multi-step classifier and Multi-step classifier with post-processing technique.

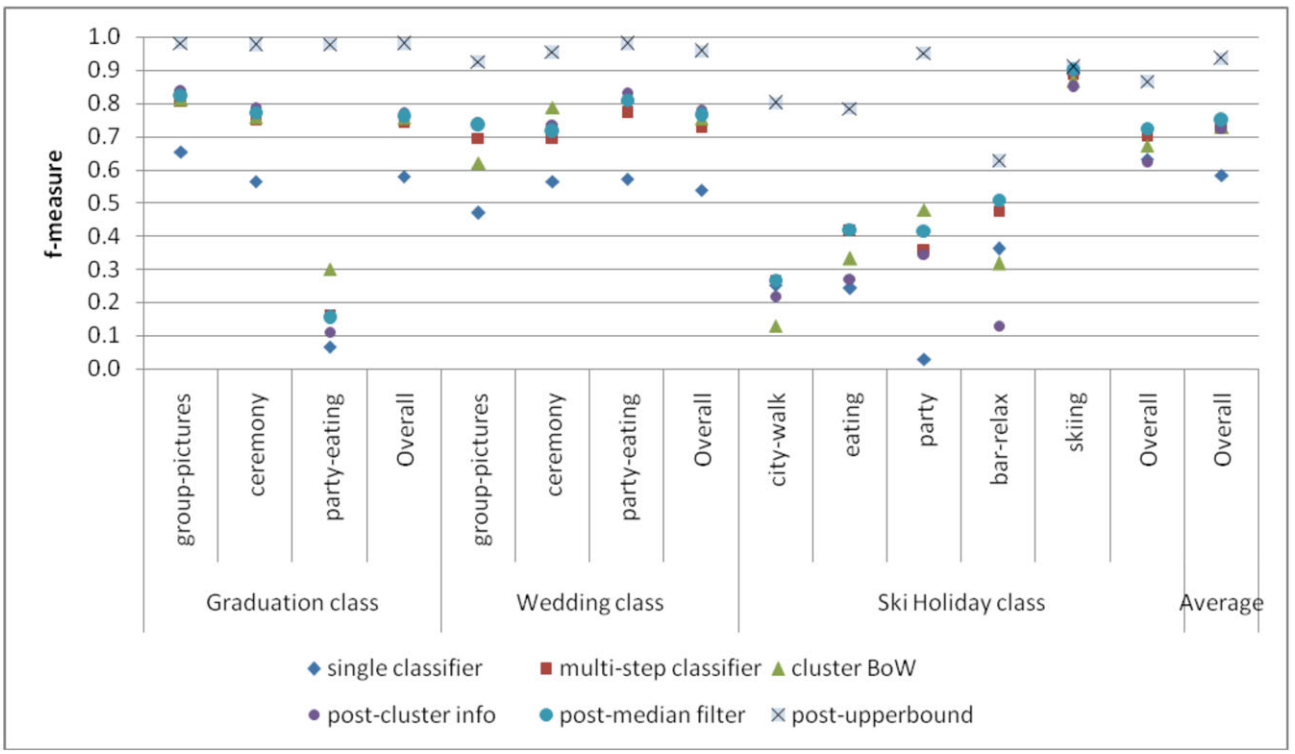

Figure 2 Sub-events: single classifier, multi-step classifier and post-processing techniques. Multi-step classifier label is the baseline for the comparison of the post-process techniques.

REFERENCES

[1] J.M. Zacks, T.S. Braver, M.A. Sheridan, D.I. Donaldson, A.Z. Snyder, J.M. Ollinger, R.L. Buckner, M.E. Raichle, "Human brain activity time-locked to perceptual event boundaries," *Nature neuroscience*, vol.4, n.6, pp.651-655, Jun. 2001.

[2] C. Faloutsos, R. Barber, M. Flickner, J. Hafner, W. Niblack, D. Petkovic, W. Equitz, "Efficient and effective querying by image content," *Journal on Intelligent Information Systems*, vol.3, pp.3-4, Jul. 1994.

[3] R. Aibing, R. K. Srihari, Z. Zhongfei, "Spatial color histograms for content-based image retrieval," *IEEE Conference on Tools with Artificial Intelligence 1999,* pp.183-186, 1999.

[4] C. Schmid, R. Mohr, C. Bauckhage. "Evaluation of Interest Point Detectors," *International Journal on Computer Vision*, vol.37, n.2, pp.151-172, Jun. 2000.

[5] K. Mikolajczyk, C. Schmid, "A Performance Evaluation of Local Descriptors," *IEEE Transactions on Pattern Analysis and Machine Intelligence*, vol.27, n.10, pp.1615-1630, Oct. 2005.

[6] J.K. Kämäräinen, V. Kyrki, H. Kälviäinen, "Invariance Properties of Gabor Filter Based Features - Overview and Applications", *IEEE Transactions on Image Processing*, vol.15, n.5, pp.1088-1099, May 2006.

[7] H. Tamura, S. Mori, T. Yamawaki, "Textural features corresponding to visual perception," *IEEE Transaction on Systems, Man, and Cybernetics,* vol.8, n.6, pp.460-472, Jun. 1978.

[8] T. Sikora, "The MPEG-7 visual standard for content description-an overview," *IEEE Transactions on Circuits and Systems for Video Technology,* vol.11, no.6, pp.696-702, Jun 2001.

[9] S.A. Chatzichristofis, Y.S. Boutalis, "CEDD: color and edge directivity descriptor: a compact descriptor for image indexing and retrieval," C*onference on Computer vision systems 2008* (ICVS 2008), pp.312-322, 2008.

[10] M. Broilo, E. Zavesky, A. Basso, F.G.B. De Natale, "Unsupervised event segmentation of news content with multimodal cues," *Workshop on Automated information extraction in media production 2010* (AIEMPro 2010), pp.39-44, 2010.

[11] A. Oliva and A. Torralba, "Modeling the shape of the scene: A holistic representation of the spatial envelope," *International Journal of Computer Vision*, vol.42, n.3, pp.145–175, May 2001.

[12] D. Lowe, "Distinctive image features from scale-invariant keypoints," *International Journal of Computer Vision*, vol.60, n.2, pp.91–110, 2004.

[13] K.E.A. Van de Sande, T. Gevers, C.G.M. Snoek. "Evaluating color descriptors for object and scene recognition," *IEEE Transactions on Pattern Analysis and Machine Intelligence,* vol.32, n.9, pp.1582-1596, Sep. 2010.

[14] M. Heikkila, M. Pietikainen, C. Schmid. "Description of interest regions with local binary patterns," *Journal on Pattern Recognition*, vol.42, n.3, pp.425-436, Mar. 2009.

[15] H. Bay, A. Ess, T. Tuytelaars, L. Van Gool, "SURF: Speeded Up Robust Features," *Computer Vision and Image Understanding*, vol.110, n.3, pp.346-359, 2008.

[16] J.R.R. Uijlings, A.W.M. Smeulders, R.J.H. Scha, "Real-Time Visual Concept Classification," *IEEE Transactions on Multimedia*, vol.12, n.7, pp.665-681, Nov. 2010.

[17] S. Theodoridis, K. Koutroumbas, "Pattern Recognition," Academic Press, 3 edition, March 2006.

[18] N. Ailon, R. Jaiswal, C. Monteleoni, "One-pass approximate k-means optimization," *Workshop on On-line Learning with Limited Feedback 2009*, 2009.

[19] M. Cooper, J. Foote, A. Girgenshon, L. Wilcox, "Temporal event clustering for digital Photo collections," *ACM Transactions on Multimedia Computing, Communications, and Applications,* vol.1, n.3, pp. 269-288, 2005.

[20] X. Liao, Y. Wang, L. Ding, "Discovering Temporal Patterns from Images using Extended PLSA," *Conference on Multimedia Technology 2010* (ICMT 2010)*,* pp.1-7, 2010.

[21] A. Bosch, A. Zisserman, X. Muñoz, "Scene Classification Via pLSA," *European Conference on Computer Vision 2006* (ECCV 2006), pp.517-530, 2006.

[22] M. Pavan, M. Pelillo, "Dominant sets and hierarchical clustering," *IEEE Conference on Computer Vision 2003,* pp.362-369, 2003.

[23] L. Shao, R. Mattivi: "Feature detector and descriptor evaluation in human action recognition". *ACM Conference on Image and Video Retrieval 2010*, 2010.

[24] N. Robertson, I. Reid, M. Brady, "Behaviour Recognition and Explanation for Video Surveillance," *Conference on Crime and Security 2006,* pp.458-463, 2006.

[25] S. Park, J.K. Aggarwal, "A hierarchical bayesian network for event recognition of human actions and interactions," *Multimedia Systems*, vol.10, n.2, pp.164–179, Aug. 2004.

[26] H. Foroughi, B.S. Aski, H. Pourreza, "Intelligent Video Surveillance for Monitoring Elderly in Home Environments," *Conference on Computer and Information Technology 2008* (ICCIT 2008), 2008.

[27] R. Mehran, A. Oyama, M. Shah, "Abnormal crowd behavior detection using social force model," *IEEE Conference on Computer Vision and Pattern Recognition 2009* (CVPR 2009), pp.935-942, 2009.

[28] I. Tsampoulatidis, N. Gkalelis, A. Dimou, V. Mezaris, I. Kompatsiaris. "High-level event detection system based on discriminant visual concepts," *ACM Conference on Multimedia Retrieval 2011* (ICMR 2011), 2011.

[29] P. Zontone, G. Boato, F.G.B. De Natale, A. De Rosa, M. Barni, A. Piva, J. S. Hare, D. Dupplaw, P. H. Lewis, "Image diversity analysis: context, opinion and bias," *Workshop on Living Web: Making Web Diversity a true asset 2009*, 2009.

[30] U. Westermann, R. Jain, "Toward a Common Event Model for Multimedia Applications," *IEEE Multimedia,* vol.14, no.1, pp.19-29, Jan.-Mar. 2007.

[31] M. Szummer and R.W. Picard, "Indoor-outdoor image classification," *IEEE Workshop on Content-Based Access of Image and Video Database,* pp.42-51, 1998.

[32] M. Broilo, P. Rocca, F.G.B. De Natale, "Content-Based Image Retrieval by a Semi-Supervised Particle Swarm Optimization" *IEEE Workshop on Multimedia Signal Processing 2008*, pp.666-671, 2008.

[33] M. Aly, P. Welinder, M. E. Munich, P. Perona, "Automatic discovery of image families: Global vs. local features," *IEEE Conference on Image Processing 2009* (ICIP 2009), pp.777-780, 2009.

[34] K.E.A. Van de Sande, T. Gevers, C.G.M. Snoek, "Evaluating Color Descriptors for Object and Scene Recognition", *IEEE Transactions on Pattern Analysis and Machine Intelligence*, vol.32, n.9, pp.1582-1596, 2010.

[35] P. Dollár, V. Rabaud, G. Cottrell, S. Belongie, "Behavior Recognition via Sparse Spatio-Temporal Features," *Visual Surveillance and Performance Evaluation of Tracking and Surveillance 2005,* 2005.

[36] L.J. Li, "What, where and who? Classifying events by scene and object recognition," IEEE Conference on Computer Vision 2007 (ICCV 2007), 2007.
[37] W. Jiang, A.C. Loui, "Semantic event detection for consumer photo and video collections," *IEEE Conference on Multimedia and Expo 2008* (ICME 2008), 2008.
[38] N. Rasiwasia, N. Vasconcelos, "Scene classification with low-dimensional semantic spaces and weak supervision," *IEEE Conference on Computer Vision and Pattern Recognition 2008*, pp. 1–6, 2008.
[39] N. Imran, J. Liu, J. Luo, M. Shah, "Event recognition from photo collections via PageRank," *ACM Conference on Multimedia 2009,* 2009.
[40] M. Das, A.C. Loui, "Event classification in personal image collections", *IEEE Conference on Multimedia and Expo 2009* (ICME 2009), 2009.
[41] D. Lin, A. Kapoor, G. Hua, S. Baker, "Joint people, event, and location recognition in personal photo collections using cross-domain context," *European conference on Computer vision 2010* (ECCV 2010), pp.243-256, 2010.
[42] M.S. Dao, D.T. Dang-Nguyen, F.G.B. De Natale, "Signature-Image-Based Event Analysis for Personal Photo Albums," *ACM Conference on Multimedia 2011,* 2011.
[43] A. Graham, H. Garcia-Molina, A. Paepcke, T. Winogrand, "Time as the essence for photo browsing through personal digital libraries," *ACM Joint Conference on Digital Libraries 2002*, 2002.
[44] J.H. Lim, Q. Tian, P. Mulhelm, "Home photo content modeling for personalized event-based retrieval," *IEEE Multimedia*, vol.10, n.4, pp.28–37, 2003.
[45] A. Jaffe, M. Naaman, T. Tassa, M. Davis, "Generating summaries and visualization for large collections of georeferenced photographs," *ACM Workshop on Multimedia Information Retrieval 2006* (MIR 2006), pp.89–98, 2006.
[46] L. Cao, J. Luo, H. Kautz, T.S. Huang, "Annotating collections of photos using hierarchical event and scene models", *IEEE Conference on Computer Vision and Pattern Recognition 2008* (CVPR 2008), 2008.
[47] J. Yuan, J. Luo, Y. Wu, "Mining Compositional Features From GPS and Visual Cues for Event Recognition in Photo Collections," *IEEE Transactions on Multimedia,* vol.12, no.7, pp.705-716, Nov. 2010.
[48] J. Luo, J. Yu, D. Joshi, W. Hao, "Event recognition: viewing the world with a third eye," *ACM Conference on Multimedia 2008,* pp.1071-1080, 2008.
[49] R. Mattivi, J. Uijlings, F.G.B. De Natale, N.Sebe, "Exploitation of time constrains for (sub-)event recognition," *ACM Workshop on Modeling and Representing Events 2011*, 2011.
[50] C. Schuldt, I. Laptev, B. Caputo, "Recognizing Human Actions: A Local SVM Approach," *Conference on Pattern Recognition 2004* (ICPR 2004), 2004.
[51] I. Laptev, M. Marszalek, C. Schmid, B. Rozenfeld, "Learning realistic human actions from movies," *IEEE Conference on Computer Vision and Pattern Recognition 2008* (CVPR 2008), pp.1-8, 2008.
[52] A. Quattoni, A. Torralba, "Recognizing Indoor Scenes," *IEEE Conference on Computer Vision and Pattern Recognition 2009* (CVPR 2009), 2009.
[53] http://www.multimediaeval.org/mediaeval2011/SED2011/index.html

Riccardo Mattivi was born in Italy in 1984. He received BA and MSc in Telecommunication Engineering from the University of Trento, Italy. He is currently a PhD candidate in Information and Communication Technologies at DISI department at the University of Trento.

His researches focus on detection and recognition of events in multimedia data within the EU project GLOCAL. He is interested in patter recognition, image analysis and understanding, image retrieval and multidimensional data management and analysis.

Giulia Boato was born in Italy in 1979. She received the M.Sc. in Mathematics in 2002, and the Ph.D. in Information and Communication Technologies in 2005, both from the University of Trento, Italy. In 2006 she was visiting researcher at the Signal Theory and Communications Department of the University of Vigo (Spain). Currently, she is Assistant Professor at the Department of Information Engineering and Computer Science (DISI) at the University of Trento, working in the Media Laboratory.

Her research interests are focused on image and signal processing, with particular attention to multimedia data protection, data hiding and image forensics, but also intelligent multidimensional data management and analysis. On these topics she is active in the European Projects coordinated by DISI: in LIVINGKNOWLEDGE for the development of image forensics methods supporting opinion mining on the web, in GLOCAL for the design of multimedia annotation and retrieval systems based on the concept of event.

Giulia Boato is a Member of IEEE.

Francesco G.B. De Natale (M.Sc. in Electronic Engineering, 1990, Ph.D. in Telecommunications, 1994) is Professor of Telecommunications Engineering at University of Trento, Italy.

His research interests are focused on multimedia communications, with particular attention to multidimensional signal processing, analysis, archiving and transmission. He was General Chair of the Packet Video Workshop (PV-2000), TPC Co-Chair of the IEEE Intl. Conf. on Image Processing (ICIP-2005) and General Chair of the ACM Intl. Conf. on Multimedia Retrieval (ICMR-2011). He is Associate Editor of the IEEE Trans on Multimedia and member of the IEEE Signal Proc. Society Technical Committee on Multimedia Signal Processing (MMSP). In 1998 he was co-recipient of the IEEE Chester-Sall Best Paper Award. He is the Coordinator of the EU IP GLOCAL project.

Prof. De Natale is a Senior Member of IEEE.

General Bit Error Ratio Analysis of Interference Affected M-PSK Transmissions

(Invited Paper)

László Pap, *Senior Member, IEEE,* Albert Mráz, *Member, IEEE*

***Abstract*—The authors of current work provide a performance analysis in terms of the bit-error-ratio of gray-mapped M-PSK transmission. The analysis results exact and closed form expressions which consider the effects of different interference scenarios with arbitrary number of interference sources and multiple types of fading scenarios on the propagation of the analyzed signal. Both effects have been modeled stochastically.**

***Index Terms*—M-PSK, BER, Rayleigh-, Rice-, Nakagami-fading, stochastic interference model.**

I. INTRODUCTION

EXACT and closed form bit-error-ratio (BER) calculation method will be provided in this paper for M-ary phase-shift keying (PSK) transmission, considering arbitrary number of interference sources and different fading models affecting the propagation of the useful signal.

Numerous works are present in the literature, which deal with solutions for the error analysis of M-PSK transmission. Paper [1] – referring the related existing calculation methods – contains an exact symbol-error-ratio (SER) calculation for M-ary quadrature modulation (QAM) and M-PSK transmission, which contains an extended interference- and fading model for the calculation, generally defined in [2]. The referred model contains a universal fading calculation method and interference model for M level frequency shift keying (FSK) with the *fully separated* handling of the interference and fading effects, resulting a gainful and extendable tool for considering almost arbitrary fading- (Rayleigh, Rice and Nakagami) and interference situations. The contribution of [1] means a novelty for the interference model by considering the effects of the spectral overlap between the useful- and interfering signals, calculating with the spectral shapes and the frequency-domain distances of them. The model has been extended to arbitrary number of OFDM interferers with sinc spectral shapes.

A previous work of current authors [3] provides an extension of [1] towards the BER calculation of M-QAM over the previously considered fading channels and involving the extended interference model of [1]. The developed solution provides an extension for [4] as an exact BER calculation of the gray-mapped M-QAM. However it deals only with additive white Gaussian-noise (AWGN) and without any interference effects. The contribution of [3] expands the BER calculation with interference- and fading models of [2] with some transformations in reference to the original BER expression to make it able to involve the defined models.

László Pap and Albert Mráz are with the Department of Telecommunications, Budapest University of Technology and Economics, Budapest H-1117, Hungary (e-mail: pap@hit.bme.hu, mraz@hit.bme.hu).

Manuscript received August 1, 2011; revised August ?, 2011.

This paper aims to provide exact closed form BER calculation for gray-mapped M-PSK transmission with different newly defined interference models and for the extension of the spectral overlap calculation of [1]. Within this area a SER calculation has already been interpreted in [5] containing the effects of imperfections during the synthesis of the in-phase- and quadrature components within the M-PSK transmitter. It was expressed for AWGN channel with the help of the two-dimensional Gaussian error functions. The SER calculation of M-PSK has been extended to BER calculation with gray mapping and fading channels affecting the useful signal [6]. Nevertheless, the random properties of the interference have not been investigated. An other path for the calculation of the BER of M-PSK has been given in [7] presenting exact closed form BER expression for 8-PSK. However for larger M values only (tight) upper and lower bounds have been given. The authors of [8] have provided an improvement for [7] resulting an exact solution for *arbitrary* M levels for AWGN and gray mapping likewise.

This paper has the following structure. In Section II a framework will be proposed for the calculation of the BER of M-PSK according to [8] valid for AWGN and gray mapping, which will be extended to the mathematical form defined in [2] and [1] with the investigation of the spectral overlap among the interferers and introducing an extended interference model within Sections III and IV. A transformed form of the M-PSK BER expression will be given in Section V, which is extendable to consider various interference- and fading models. Three different interference scenarios will be analyzed in Section VI and illustrated with calculation results.

II. BIT ERROR RATE OF M-PSK IN AWGN CHANNEL

A solution has been provided in [8] for the calculation of the average BER of M-PSK for AWGN and assuming gray coding. The solution has been a refinement of the calculation method in [7], which gives only an upper bound for $M \geq 16$, where M denotes the size of the modulation alphabet. The reason of this inaccuracy has been shown in [8] and the following expression has been resulted for the average BER of gray-coded M-PSK

$$P_b = \frac{1}{\log_2(M)} \sum_{m=1}^{M-1} \overline{d}\,(m)\, P\,(m), \tag{1}$$

in which $\overline{d}\,(m)$ represents a so-called average distance spectrum, denoting the average number of bit positions differing adequately to the alternatives of the received signal with the

description of

$$\overline{d}(m) = 2\left|\frac{m}{M} - \left\lfloor\frac{m}{M}\right\rceil\right| + 2\sum_{i=2}^{\log_2(M)}\left|\frac{m}{2^i} - \left\lfloor\frac{m}{2^i}\right\rceil\right|, \quad (2)$$

where $\lfloor . \rceil$ denotes the rounding to the nearest integer. Within expression (1) $P(m)$ represents the probability, that the received signal vector falls into the decision region of R_m in the case of $X = 0$ has been sent as

$$P(m) = \Pr\{\mathbf{Y} \in R_m | X = 0\}, \quad (3)$$

where X denotes the transmitted symbol with $X \in \{0, 1, ..., M-1\}$. The expression of $P(m)$ has been defined and calculated in [7, eq. (3)] (denoted by A_m) as

$$P(m) = \int_0^\infty f(z)\left[Q\left[\vartheta + z\cdot\tan\left(\left(\frac{M}{2} - 2m - 1\right)\frac{\pi}{M}\right)\right] - Q\left[\vartheta + z\cdot\tan\left(\left(\frac{M}{2} - 2m + 1\right)\frac{\pi}{M}\right)\right]\right]dz, \quad (4)$$

in which $\vartheta = \sqrt{2\cdot\log_2(M)\frac{E_b}{N_0}}$ with E_b being the bit-energy and N_0 the spectral power density of the AWGN, $f(z) = \exp\left(-z^2/2\right)/\sqrt{2\pi}$, while $Q(x) = 1/\sqrt{2\pi}\int_x^\infty \exp\left(-u^2/2\right)du$ represents the tail probability of the standard normal distribution. Note, we have performed some modifications in terms of the notations compared to [7] and [8] to avoid the handling of unnecessary variables.

In Section V we will extend the BER expression defined in (1) – valid for AWGN channel – in a similar way to [1] and [3], in order to consider a general interference model. However, this extension could only be performed if $P(m)$ would have a special *exponential integral* form, which is not true for (4). Furthermore, the $Q(.)$ components of it cannot be simply transformed into the desired form. It means that an alternate method needs to be invented to calculate $P(m)$. Towards this, let consider the constellation model of Fig. 1. The streaked part of the circle represents the decision region R_m. With the notations of the model

$$\tan(\varphi_1(m)) = \frac{\mathbf{r}_1\sin(\theta)}{\sqrt{E_s} - r_1\cos(\theta)},$$

from which the $\mathbf{r}_1$ distance vector (to $X = 0$) can be expressed as

$$\mathbf{r}_1 = \sqrt{E_s}\frac{\tan(\varphi_1(m))}{\sin(\theta) + \tan(\varphi_1(m))\cos(\theta)},$$

with $\varphi_1(m) = \pi\frac{2m-1}{M}$ and $\varphi_2(m) = \pi\frac{2m+1}{M}$. After that, the $P(m)$ probability can be expressed with a surface integral for the signal space $\mathcal{A}$ as

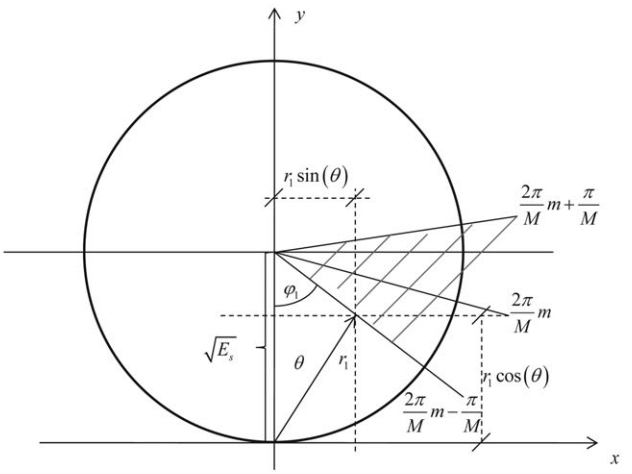

Fig. 1: Model to calculate $P(m)$ probability with the help of the polar coordinates

$$P(m) = \iint_{\mathcal{A}}\frac{1}{\pi N_0}\exp\left(\frac{\mathbf{r}_1^2}{N_0}\right)drd\theta = \frac{1}{2\pi}\int_0^{\beta_1(m)}\exp\left(-\frac{E_s}{N_0}\frac{\sin^2(\varphi_1(m))}{\sin^2(\varphi_1(m)+\theta)}\right)d\theta - \frac{1}{2\pi}\int_0^{\beta_2(m)}\exp\left(-\frac{E_s}{N_0}\frac{\sin^2(\varphi_2(m))}{\sin^2(\varphi_2(m)+\theta)}\right)d\theta, \quad (5)$$

containing the E_s symbol energy and the $\beta_1(m) = \pi - (2m-1)\pi/M$ and $\beta_2(m) = \pi - (2m+1)\pi/M$ integration limits. Following the transformation above, we will be able to re-calculate the results of [8]. At the same time, we have originally aimed for making make the expression of P_b suitable to be an object of a further extension after which almost-arbitrary interference scenarios could be modeled during the calculations.

III. CALCULATION OF THE SPECTRAL OVERLAP

It was shown in [1] that the frequency-domain distance and the spectral shapes of the useful- and interfering signals influences the final BER results. To model this effect, a so-called *spectral overlap* factor has been defined as

$$v(\Delta f_k) = \frac{\int_{-\infty}^{\infty} S_{\eta_k}(f - \Delta f_k)\,S(f)\,df}{\int_{-\infty}^{\infty} S(f)\,df}, \quad (6)$$

where $S_{\eta_k}(f)$ was defined the spectral shape of interferer k with the dimension of $[\frac{1}{\text{Hz}}]$ and an $\eta_k(t)$ complex Gaussian process has been introduced with independent real- and imaginary components and $R_{\eta_k}(0) = 1$. $S(f)$ will be considered as the spectral power density of the useful signal in $[\frac{\text{W}}{\text{Hz}}]$. After that, the amount of $v(\Delta f_k)$ is expected to be a value with the dimension of [s]= $[\frac{1}{\text{Hz}}]$, which is proportional to the spectral shapes of the useful- and interfering signals and the s_0 power of the useful signal.

A. Interferers with sinc spectral shape

Expression (6) was calculated in [1] for OFDM interference. In this case the $S_{\text{OFDM}}(f)$ spectral power density function of an OFDM subcarrier has been assumed to have a pulse shape for the $s(t)$ time-domain signal in terms of

$$s(t) = \begin{cases} \sqrt{s_0}\ \text{[V]}, \text{ if } t \in \left[-\frac{T_\text{s}}{2}, \frac{T_\text{s}}{2}\right) \\ 0, \text{ otherwise,} \end{cases}$$

where T_s represents the symbol period. Thus the spectral power density function of $s(t)$ after applying Fourier-transform can be expressed as

$$S_{\text{OFDM}}(f) = \\ = \frac{s_0}{T_\text{s}} \left| \int_{-\frac{T_\text{s}}{2}}^{\frac{T_\text{s}}{2}} e^{-j2\pi ft} dt \right|^2 = s_0 T_\text{s} \left(\frac{\sin(\pi f T_\text{s})}{\pi f T_\text{s}} \right)^2 \left[\frac{\text{W}}{\text{Hz}}\right] \quad (7)$$

as a variant of the $\text{sinc}(x) = \sin(x)/x$ function. Similarly, assuming the same T_s symbol period for the interferers, the spectral power density function of interferer k can be given with $S_{\eta_k,\text{OFDM}}(f) = T_\text{s}\left(\frac{\sin(\pi f T_\text{s})}{\pi f T_\text{s}}\right)^2$. It was shown in [1] that for $l \in \mathbb{Z}$

$$v_{\text{OFDM}}(\Delta f_k) = v_{\text{OFDM}}(l \cdot \Delta f_\text{c}) = \frac{T_\text{s}}{l^2\pi^2} \left[\frac{1}{\text{Hz}}\right], \quad (8)$$

in which $\Delta f_k = |f_0 - f_k|$ represents the frequency domain distance of the f_k center frequency of interferer k from the f_0 carrier frequency of the useful signal. The expression above means that for Δf_k values, which can be expressed with the integer l multiples of the Δf_c subcarrier spacing, the calculation of $v_{\text{OFDM}}(.)$ represents a reasonably simpler task.

B. Interferers with raised cosine spectral shape

The calculation of the spectral overlap above is valid for OFDM transmission. Nevertheless, PSK modulation is not frequently applied for OFDM transmission. To create a realistic interference model, let consider spectral shapes generated by a raised cosine (RC) filter. For assuming a simplified form of the $|G_\text{rc}(f)|$ spectral shape of a signal generated by a RC filter, let consider a *unit roll-off factor* [9] for that. After that

$$|G_\text{rc}(f)| = \begin{cases} \frac{T_\text{s}}{2}\left[1 + \cos(\pi f T_\text{s})\right] \left[\frac{1}{\text{Hz}}\right], \text{ if } |f| \le \frac{1}{T_s} \\ 0, \text{ otherwise} \end{cases} \quad (9)$$

We know that $|G_\text{rc}(f)|^2 = \frac{T_s}{s_0} S_\text{rc}(f)$ with the $S_\text{rc}(f)$ spectral power density of the useful signal. During the calculation of the integral in (6) applied to the current case, the numerator will be expressed as $\int_{-1/T_\text{s}+\Delta f_k}^{1/T_\text{s}} S_{\eta_k,\text{rc}}(f - \Delta f_k) S_\text{rc}(f)\, df$, with $S_{\eta_k,\text{rc}}(f) = \frac{1}{T_s}|G_\text{rc}(f)|^2$. For the denominator it can be shown, that $\int_{-\infty}^{\infty} S_\text{rc}(f)\, df = \frac{3}{4}s_0$. Then the spectral overlap

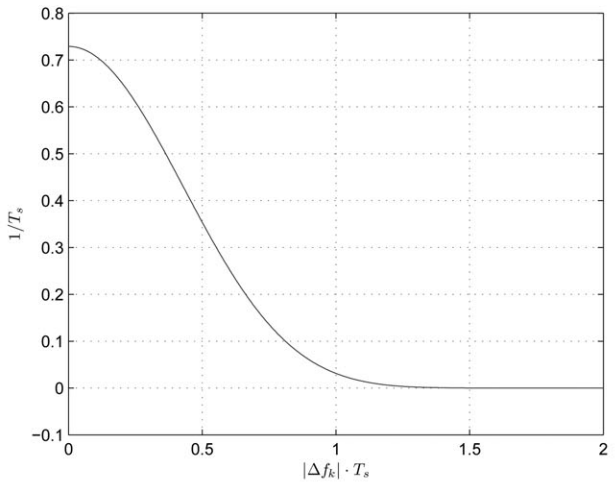

Fig. 2: Illustration of the $v_\text{rc}(\Delta f_k)$ overlap for raised cosine spectral shapes of the interferers and useful signal

can be given with

$$v_\text{rc}(\Delta f_k) = \frac{3T_s}{8} - \frac{3\Delta f_k T_s^2}{16} + \\ + \frac{T_s}{6}(\Delta f_k T_s - 2)\cos(\pi \Delta f_k T_s) + \\ + \frac{T_s}{96}(\Delta f_k T_s - 2)\cos(2\pi \Delta f_k T_s) + \frac{5T_s}{18\pi}\sin(\pi \Delta f_k T_s) + \\ + \frac{25T_s}{576\pi}\sin(2\pi \Delta f_k T_s) \quad (10)$$

with the dimension of $1/[\text{Hz}]$ for $0 < |\Delta f_k| \le \frac{2}{T_s}$, since the signal contains any power only within this interval. Fig. 2 contains the illustration of $v_\text{rc}(\Delta f_k)$. It is visible that $v_\text{rc}(\Delta f_k) = 0$ for $|\Delta f_k| \ge \frac{2}{T_\text{s}}$, i.e. no interference effect will be resulted with larger freq. distances than $\frac{2}{T_\text{s}}$ in contrast to the OFDM case with $v_{\text{OFDM}}(\Delta f_k) > 0$ to arbitrary large Δf_k values at the same time.

IV. Extended SNR Model

Following the introduction of the spectral overlap concept, we return to the insertion of the interference – as it was defined in [1] – into a common 'signal-to-noise model' of the BER calculation, which generally considers the $\frac{E_\text{b}}{N_0}$ fraction. An effective γ signal-to-noise ratio has been introduced, which contains an extended N_0' amount considering the effects of the spectral power density of the received 'original' N_0 additive white Gaussian noise and the effective interference energy. See details in [1, Eq. (14)]. The extended signal-to-noise ratio has been expressed as

$$\gamma = \frac{E_b}{N_0'} = \frac{s_0 T_b}{N_0'} = \frac{s_0 T_b}{N_0 + \sum_{k=1}^{K} s_k \cdot v(\Delta f_k)}, \quad (11)$$

in which T_b denotes the bit time-interval and s_k represents the instantaneous received power of interferer k with $k \in (1, 2, ..., K)$, where K represents the total number of

interferers. In addition $\sum_{k=1}^{K} s_k \cdot v(\Delta f_k)$ also contains the $v(\Delta f_k)$ spectral overlap formerly expressed in equations (8) and (10) and the reason why it can be handled additively to N_0 is that the interference is assumed to propagate across a complex Gaussian (Rayleigh fading channel) characterized by the previously defined $\eta_k(t)$ process.

V. EXTENSION OF THE BER CALCULATION

After considering the interference as an additive quantity to the AWGN, we will be be able to deal with different interference models. Nevertheless, we should consider and solve some computational problems assuming some parameters as *random variables*. This computational solution will be detailed within the current section.

A. Insertion of the interference model

Let us denote the elements of expression (5) with $f_1(s_0, m)$ and $f_2(s_0, m)$ according to

$$P(m) = f_1(s_0, m) - f_2(s_0, m)$$

which will be the functions of s_0 and m. Furthermore, $C_1(\theta, m) = \frac{\sin^2(\varphi_1(m)+\theta)}{\sin^2(\varphi_1(m))}$ and $C_2(\theta, m) = \frac{\sin^2(\varphi_2(m)+\theta)}{\sin^2(\varphi_2(m))}$, while $E_\mathrm{b} = s_0 T_\mathrm{b}$ with $T_\mathrm{b} = \frac{T_\mathrm{s}}{\log_2(M)}$. Let us substitute the extended (containing interference) γ effective signal-to-noise-ratio value defined in (11) into the components of $P(m)$ in expression (5), yielding

$$f_1(s_0, m|\mathbf{s}, \mathbf{f}) = \\ = \frac{1}{2\pi} \int_0^{\beta_1(m)} \exp\left(-\frac{E_s}{N_0 + \sum_{k=1}^{K} s_k \cdot v(\Delta f_k)} \frac{1}{C_1(\theta, m)} \right) d\theta \tag{12}$$

and

$$f_2(s_0, m|\mathbf{s}, \mathbf{f}) = \\ = \frac{1}{2\pi} \int_0^{\beta_2(m)} \exp\left(-\frac{E_s}{N_0 + \sum_{k=1}^{K} s_k \cdot v(\Delta f_k)} \frac{1}{C_2(\theta, m)} \right) d\theta, \tag{13}$$

where $\mathbf{s} = (s_1, s_2, ..., s_K)$ and $\mathbf{f} = (f_1, f_2, ..., f_K)$ represent the vectors constituted of the instantaneous received power levels and the center frequencies of the interference sources respectively.

As it has been emphasized both in [2] and [3], expressions (12) and (13) are conditional quantities with two sets of conditions $\mathbf{s}$ and $\mathbf{f}$, since the elements of these two vectors are considered as *random variables* (RVs). To get the unconditional forms of $f_1(s_0, m)$ and $f_2(s_0, m)$, we should execute an expected value calculation with respect to the many RVs defined above. It has been already discussed, that these calculations would require a K-fold integration severally to (12) and (13) in terms of the s_k and f_k RVs. In addition $\sum_{k=1}^{K} s_k \cdot v(\Delta f_k)$ is a sum of RVs and it is located *within the denominator* of γ, which leads to further hardness regarding the calculation. Furthermore, s_0 can be also considered as a RV. To solve this difficult computational challenge, the authors of [2] have introduced a transformation according to the following lemma.

Lemma 1: For any $x, y > 0$

$$\exp\left(-\frac{y}{x}\right) = 1 - \int_0^{\infty} \frac{J_1(2\sqrt{z})}{\sqrt{z}} \exp\left(-z\frac{x}{y}\right) dz \tag{14}$$

where $J_1(.)$ represents the Bessel function of first order and first kind.

Applying (14), the numerators and denominators of expressions (12) and (13) will be reversed as

$$f_1(s_0, m|\mathbf{s}, \mathbf{f}) = \\ = \frac{1}{2\pi} \int_0^{\beta_1(m)} \left[1 - \int_0^{\infty} \frac{J_1(2\sqrt{z})}{\sqrt{z}} \exp\left(-z\frac{N_0}{s_0 T_\mathrm{s}} C_1(\theta, m) \right) \cdot \right. \\ \left. \cdot \exp\left(-\frac{z}{s_0 T_\mathrm{s}} \sum_{k=1}^{K} s_k \cdot v(\Delta f_k) C_1(\theta, m) \right) dz \right] d\theta \tag{15}$$

and

$$f_2(s_0, m|\mathbf{s}, \mathbf{f}) = \\ = \frac{1}{2\pi} \int_0^{\beta_2(m)} \left[1 - \int_0^{\infty} \frac{J_1(2\sqrt{z})}{\sqrt{z}} \exp\left(-z\frac{N_0}{s_0 T_\mathrm{s}} C_2(\theta, m) \right) \cdot \right. \\ \left. \cdot \exp\left(-\frac{z}{s_0 T_\mathrm{s}} \sum_{k=1}^{K} s_k \cdot v(\Delta f_k) C_2(\theta, m) \right) dz \right] d\theta. \tag{16}$$

Let us consider the benefits of this seemingly difficult transformation. The significant advantage of (14) is that the s_0 instantaneous power of the useful signal and the $\sum_{k=1}^{K} s_k \cdot v(\Delta f_k)$ interference become able to be *handled independently* during the calculation, and the necessity of the K-fold integrations could be eliminated, since the expected value will be able to calculated with the help of the *moment generating function*. The detailed modeling of the different interference scenarios will be demonstrated in the following section.

VI. EXAMPLES OF THE INTERFERENCE MODEL

Based on the transformation in Section V, the sum of the several random variables will appear in the exponent within (15) and (16). This fact will enable us to calculate the expected value in terms of their moment generating function. Let us express the expected value of the interference-related exponential component of $f_1(s_0, m|\mathbf{s}, \mathbf{f})$ defined in (15) with

$$\phi_1(z, \theta, m) = \mathbb{E}\left[e^{-\frac{z}{s_0 T_\mathrm{s}} \sum_{k=1}^{K} s_k v(\Delta f_k) C_1(\theta, m)} \right]. \tag{17}$$

Note that $\phi_2(z, \theta, m)$ can be also calculated similarly with the help of $C_2(\theta, m)$. In the following we will only consider the calculation of $\phi_1(z, \theta, m)$ due to the high level similarity.

The s_k and f_k RVs can be also assumed independent with identical distribution (i.i.d.) for each k. In this case the sum

within the exponent will be eliminated, and we will get a more simple form with

$$\phi_1(z,\theta,m) = \mathbb{E}\left[e^{-z\frac{s_k}{s_0 T_s} v(\Delta f_k) C_1(\theta,m)}\right]^K. \qquad (18)$$

In the following we will introduce and calculate $\phi_1(z,\theta,m)$ for three different interference scenarios.

A. Frequency hopping with OFDM interference

Let us define a scenario with 'OFDM-like' interference, meaning that 'sinc' spectral shapes (see in Section III-A) will be considered. We calculate the expected value of (18) with respect to the frequency distances of interferers to the f_0 center frequency of the useful signal. As we have seen in (8), the $v_{\text{OFDM}}(\Delta f_k)$ depends on the $l_k \in \mathbb{Z}$ parameters in a very simple way. It this interference model l_k will be considered as RVs, hence the f_k center frequencies of the interferers will be located with freq. distances expressed as *integer multiples* of a Δf_c subcarrier spacing from f_0 according to $\Delta f_k = l_k \Delta f_c = |f_0 - f_k|$. The f_k can be located at both sides of f_0, since Δf_k represents the absolute value of the frequency domain distance. Let consider $s_k = s_1$ and $l_k = l$, $\forall k$. In this case, and with the assumption that l has a discrete uniform distribution defined by $l \in \{1, 2, ..., N\}$, the expected value defined in (18) can be calculated as

$$\begin{aligned}\phi_1(z,\theta,m|s_1) &= \mathbb{E}\left[e^{-z\frac{s_1}{s_0 T_s} v(l\cdot\Delta f_c) C_1(\theta,m)}\right]^K = \\ &= \left[\frac{1}{N}\sum_{l=1}^{N} e^{-z\frac{s_1}{s_0}\frac{1}{l^2\pi^2} C_1(\theta,m)}\right]^K = \\ &= \left[\frac{1}{N}\sum_{l=1}^{N} \exp\left(-z\frac{10^{-\frac{\alpha_{\text{dB}}}{10}}}{l^2\pi^2} C_1(\theta,m)\right)\right]^K, \end{aligned} \qquad (19)$$

where N will represent the number of possible Δf_k frequency distance values and α_{dB} denotes s_1/s_0 in [dB]. For larger N the interferers with fixed K number will be located within a wider $B_{\text{ch}} = 2N \cdot \Delta f_c = N_c \cdot \Delta f_c$ bandwidth, resulting larger Δf_k distances with more and more probability, yielding lower average interference in terms of the expression of the spectral overlap with the $N_c = 2N$ number of the f_k position possibilities. The phenomena above can be observed at Fig. 3 with the calculated BER curves for 4-, 8- and 16-PSK, with $K = 1$ and assuming Rice-fading channel for the propagation of the useful signal with parameter $\kappa = 10$. To consider the fading effects, the expected value of the $\frac{\sqrt{\xi} J_1(2\sqrt{z\xi})}{\sqrt{z}}$ component of (15) and (16) should be calculated according to the ξ instantaneous fading power gain affecting the useful signal. The calculation has been detailed in [2, eq. (48)]. During our further investigations Rice-fading will be assumed. The curves of Fig. 3 have been calculated for $N = 16$ and 128 resulting lower interference and lower BER for a larger N value. The degradation effects of the same amount of interference growth results higher BER performance fall-off with the larger M level.

Let consider the adjustment of K. At Fig. 4 the BER curves are shown for the same M levels as in the previous case with fixed $N = 16$. The number of interferers was set to $K = 1$ and 20. It can be clearly observed, that with the increased number of interferers with a fixed B_{ch} bandwidth the BER performance will also suffered in an growing manner with M.

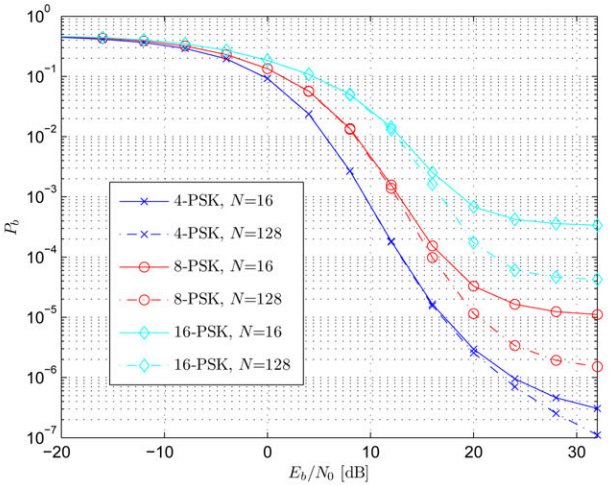

Fig. 3: BER curves for 4-, 8- and 16-PSK in case of Rice-fading with $\kappa = 10$, $\alpha_{\text{dB}} = 10$ dB and different number of possible Δf_k interferer center frequency distances N =16 and 128

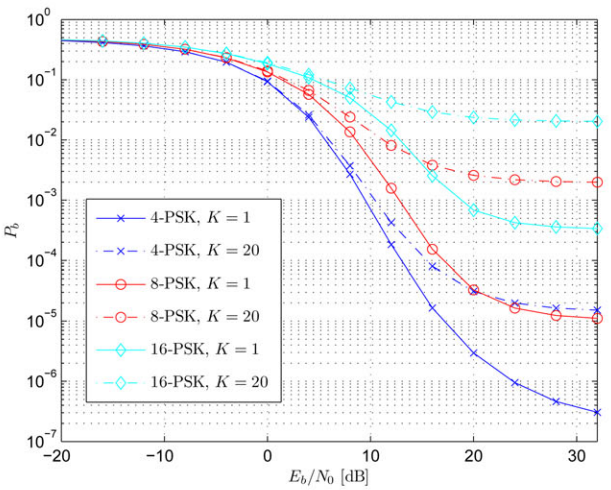

Fig. 4: BER curves for 4-, 8- and 16-PSK in case of Rice-fading with $\kappa = 10$, $\alpha_{\text{dB}} = 10$ dB and different number of interferers K=1 and 20

B. Poisson field of interferers

In this interference scenario we consider a situation in which the K number of interferers in a defined area A will be considered as a Poisson RV with the average of λ [Interferer/m^2/Hz]. In this case $\Pr\{K = k\} = \frac{(A\lambda)^k}{k!} e^{-A\lambda}$. Let r_k denote the distance between the interferer k and the receiver. We calculate $s_k = s_{k,t} r_k^{-\beta}$ with β being the pathloss exponent. The distance r_k has the distribution of $f(r_k) = 2r_k/(D^2 - D_0^2)$ with the D radius of the investigated area and a D_0 initial radius from the receiver with the same center position. We have considered $s_{k,t}$ as the transmit power of interferer k for which $s_{k,t}/s_0 = 1$ will be assumed. We would like to find $\phi_1(z,\theta,m)$ by calculating

the expected value with respect to three different RVs: K, $r_1 = r_k$ for $\forall k$ and l. The variable l will denote the same quantity as in VI-A, since we will assume sinc spectral shapes for the interferers. Then we arrive at

$$\phi(z,\theta,m) = \sum_{k=0}^{\infty} \frac{\left(\lambda\pi D^2\Omega\right)^k}{k!} e^{-\lambda\pi D^2\Omega} \times \\ \times \left(\int_{D_0}^{D} \frac{1}{N} \sum_{l=1}^{N} e^{-r_1^{-\beta} z \frac{1}{l^2\pi^2} C_1(\theta)} \frac{2r_1 dr_1}{D^2 - D_0^2} \right)^k \tag{20}$$

with $\Omega = N \cdot \Delta f_c = N/T_s$ investigated frequency domain. Upon exploiting that $\sum_{k=0}^{\infty} \frac{A^k}{k!} e^{-A} B^k = e^{A(B-1)}$ we get

$$\phi(z,\theta,m) = \\ = \exp\left(\frac{\lambda\pi D^2}{T_s} \left(\sum_{l=1}^{N} \int_{D_0}^{D} r_1 e^{-\frac{r_1^{-\beta}}{l^2} K_1(\theta,m)} \frac{2dr_1}{D^2 - D_0^2} - N \right) \right) \tag{21}$$

where $K_1(\theta,m) = z\frac{1}{\pi^2} C_1(\theta,m)$. Let us also exploit that

$$\int_{D_0}^{D} r_1 e^{-\frac{r_1^{-\beta}}{l^2} K_1(\theta,m)} dr_1 = \\ = \left[\frac{r_1^2}{\beta} \left(\frac{r_1^{-\beta} K_1(\theta,m)}{l^2} \right)^{\frac{2}{\beta}} \Gamma\left(-\frac{2}{\beta}, \frac{r_1^{-\beta} K_1(\theta,m)}{l^2} \right) \right]_{D_0}^{D} \tag{22}$$

where $\Gamma(\rho,a) = \int_a^{\infty} e^{-t} t^{\rho-1} dt$ is defined as the incomplete Gamma function. After substituting (22) into (20) we get the BER curves of Fig. 5 which illustrated the BER curves for 4-, 8- and 16-PSK with Rice-fading also in this case with $\kappa = 10$. The $\lambda = 10^{-4}$ and 10^{-5} values have been assumed for the spatial and frequency-domain density of the interferers, resulting in a higher interference and lower BER for larger λ settings. As it was observed at the previous cases, higher interference effects degrade the BER results for increasing M values.

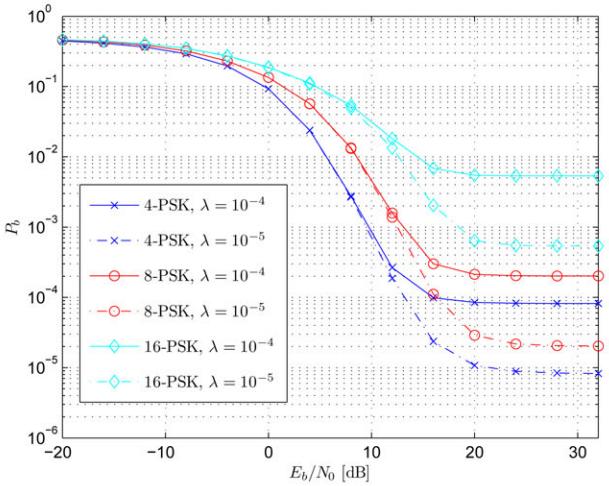

Fig. 5: BER curves for 4-, 8- and 16-PSK in case of Rice-fading with $\kappa = 10$ and different density values of interferers $\lambda = 10^{-4}$ and 10^{-5}

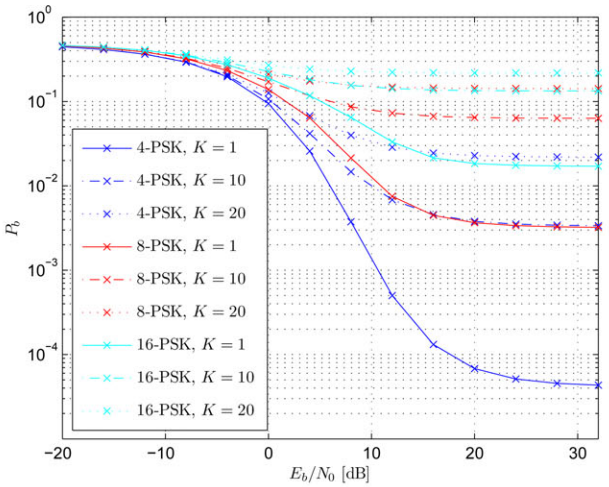

Fig. 6: BER curves for 4-, 8- and 16-PSK in case of Rice-fading with $\kappa = 10$ and different $K = 1$, 10 and 20 number of interferers

C. Interferers with raised cosine spectral shapes

For this scenario we assume $v_{rc}(\Delta f_k)$ defined for raised cosine (RC) in (10). We will perform an analysis by assuming Δf_k to be RVs with uniform distribution within the interval $[0, \frac{2}{T_s})$. Accordingly, we will calculate the expected value within $\phi(z,\theta,m|\Delta f_k, s_k)$ with assuming $s_k = s_1$, $\Delta f_k = \Delta f_1$ $\forall k$ and $s_1/s_0 = 10^{-\frac{\alpha_{dB}}{10}}$ as

$$\phi(z,\theta,m|s_1) = \left(2\int_0^{\frac{2}{T_s}} e^{-z\frac{s_1}{s_0 T_s} v_{rc}(\Delta f_1) C_1(\theta,m)} \frac{d\Delta f_1}{\Omega} \right)^K = \\ = \left(\frac{2}{\Omega} \int_0^{\frac{2}{T_s}} e^{-z\frac{s_1}{s_0 T_s} v_{rc}(\Delta f_1) C_1(\theta,m)} d\Delta f_1 \right)^K = \\ = \left(T_s \int_0^{\frac{2}{T_s}} e^{-z\frac{10^{-\frac{\alpha_{dB}}{10}}}{T_s} v_{rc}(\Delta f_1) C_1(\theta,m)} d\Delta f_1 \right)^K, \tag{23}$$

in which $\Omega = \frac{2}{T_s}$. The BER curves can be observed in Fig. 6 for 4-, 8- and 16-PSK with different number of the interferers K. Since the investigated $[0, \frac{2}{T_s})$ interval for the RC spectral shapes means a rather scant domain around the center frequency f_0 of the useful signal and in our model all f_k are located within that, the resultant interference effects leading to a BER degradation would be higher than in the case of the sinc spectral shapes (Fig. 19).

VII. CONCLUSIONS

An exact closed form calculation method was provided for the BER calculation of M-PSK transmission, which considers the interference and fading effects alike. A high-flexibility interference model has been embedded into an analytic closed form BER calculation framework, which has been originally developed for AWGN channel and without the consideration of any interference effects. The demonstrated calculation method

evaluates the effects of several input parameters, i.e. the received power of the useful signal, the received power values and center frequencies of the interferers *as random variables*, and calculates the BER as an average with respect of many RVs. This way of calculation gives a solution for such complex fading and interference scenarios which could be investigated only by simulations up to this point.

APPENDIX A
VALIDATION OF THE BER CURVES

Let introduce the ρ value of the Signal-to-Interference-Ratio (SIR) expressed as

$$\rho = \frac{s_0}{\sum_{k=1}^{K} s_k} = \frac{s_0}{K s_1} \tag{24}$$

if all of the the interferers have equal $s_k = s_1 \ \forall k$. After that $s_0 = \rho \cdot K s_1$. Our goal is now to validate the BER results with the help of paper [8] for a *deterministic* case (for s_1 and s_0), since the results of it have already been proofed by simulations and also embedded into the MATLAB®Communications Toolbox.

Let us execute an SNR conversion, which will be resulted as an interference accession according to equation (11). After that, we will get certainly lower effective SNR values, which should be substituted as an input of the expression in [8].

Let denote the 'original' (interference-free) SNR with $\gamma = \frac{E_b}{N_0}$, from which and (24)

$$\gamma = \frac{E_b}{N_0} = \frac{s_0 T_b}{N_0} = \frac{\rho \cdot K s_1}{N_0}$$

According to expressions (15) and (16), we will consider the SNR degradation caused by the interference in an effective γ' SNR expression as

$$\gamma' = \frac{E_b}{N_0 + \sum_{k=1}^{K} s_1 v(\Delta f_k)} = \frac{\gamma}{1 + \frac{s_1}{N_0} \sum_{k=1}^{K} v(\Delta f_k)} = \\ = \frac{\gamma}{1 + \gamma \frac{1}{\rho K T_b} \sum_{k=1}^{K} v(\Delta f_k)}. \tag{25}$$

If we substitute γ' into the expressions of [8], we will get and validate the BER curves. Note that for plotting the horizontal axis should contain the 'original' γ values. However, our work is not only a reproduction (or unnecessary complication) of [8], since we have provided a tool for the stochastic handling of s_0, s_k and f_k parameters.

REFERENCES

[1] A. Mraz and L. Pap, "General performance analysis of M-PSK and M-QAM wireless communications applied to OFDMA interference," in *Wireless Telecommunications Symposium (WTS), 2010*, 2010, pp. 1 –7.

[2] K. Hamdi and L. Pap, "A unified framework for interference analysis of noncoherent MFSK wireless communications," *Communications, IEEE Transactions on*, vol. 58, no. 8, pp. 2333 –2344, 2010.

[3] A. Mraz and L. Pap, "General interference analysis of M-QAM transmission applied to LTE performance evaluation," in *EUROCON - International Conference on Computer as a Tool (EUROCON), 2011 IEEE*, april 2011, pp. 1 –4.

[4] D. Y. Kyongkuk Cho, "On the general BER expression of one- and two-dimensional amplitude modulations," *IEEE Transactions on Communications*, vol. 50, no. 7, pp. 1074–1080, July 2002.

[5] D. Y. Jaeyoon Lee and S. K. Park, "Further result on the symbol error probability of MPSK with I/Q phase unbalance," *IEICE Transactions on Communications*, vol. E89-B, no. 5, pp. 1675–1677, May 2006.

[6] D. Woojin Jeong, Jaeyoon Lee, "New BER expressions of MPSK," *submitted to IEEE Transactions on Communications*, Mar 2010.

[7] P. Lee, "Computation of the bit error rate of coherent M-ary PSK with gray code bit mapping," *Communications, IEEE Transactions on*, vol. 34, no. 5, pp. 488 – 491, may 1986.

[8] J. Lassing, E. Strom, E. Agrell, and T. Ottosson, "Computation of the exact bit-error rate of coherent M-ary PSK with gray code bit mapping," *Communications, IEEE Transactions on*, vol. 51, no. 11, pp. 1758 – 1760, nov. 2003.

[9] J. Proakis, *Digital Communications*, 3rd ed. McGraw-Hill Inc., 1995.

László Pap (M93-SM97) graduated from the Technical University of Budapest, Faculty of Electrical Engineering, Branch of Telecommunications. He became Dr. Univ. and Ph.D. in 1980, and Doctor of Sciences in 1992. In 2001 and 2007 he has been elected as a Corespondent and Full Member of the Hungarian Academy of Sciences. His main fields of the research are the electronic systems, nonlinear circuits, synchronization systems, modulation and coding, spread spectrum systems, ATM, CDMA, multiuser detection and mobile communication systems. His main education activity has covered the fields of electrical amplifiers and circuits, electronics, modern modulation and coding systems, communication theory, introduction to mobile communication, transmission and processing of information, nonlinear circuits and digital technique. Professor Pap had been Head of the Dept. of Telecommunications, Budapest University of Technology and Economics and the Vice-Rector of the University.

Albert Mráz (M2005) had received the MSc degree in electrical engineering from the Budapest University of Technology and Economics (BUTE) in 2005. He is currently working toward the Ph.D. degree at BUTE. His research interests include the modeling and resource management of broadband wireless networks (3G and 4G).

Throughput maximization in Wireless Networks by Scheduling End-to-End Flows

Dilip Sarkar and Avishek Ghosal

Abstract— **Due to the hard bandwidth-constraints in wireless ad hoc networks, maximization of achievable throughput is the most important way of enhancing system performance. Existing works have attempted to maximize system throughput by increasing the number of concurrent packet transmissions within the network using multiple radio channels or by using power control techniques. The approach taken in this work is based on the fact that the overall system throughput in an ad hoc network comprising multiple multi-hop flows (IP data paths) varies considerably with the direction and number of hops involved in the flows. When multiple flows cross each other, or are close enough, then packets belonging to those flows contend with each other for channel access, thereby reducing the overall system throughput. If these flows are properly scheduled based on the number of hops involved or their direction of flow, the overall system throughput can be significantly increased. In this work, certain scheduling strategies are proposed and evaluated that prioritize the different flows in the network and aims to improve the overall system throughput. Simulation results indicate that significant improvement can be achieved with the proposed scheduling methods.**

I. INTRODUCTION

During the past decade, there has been a tremendous increase in the popularity of wireless networks. Currently, wireless networks can be categorized into two types - infrastructured and infrastructreless. The immensely popular *cellular networks* are of the first type where a mobile connects to the nearest base station. Each base station may serve hundreds of mobiles in a cell by allocating resources and providing hand-off support. On the other hand, *ad hoc networks*, *sensor networks*, and *wirless LANs* belong to the second category and do not have a fixed infrastructure as a backbone [10]. Since this work focuses on throughput maximization of ad hoc networks, the next section describes them in detail.

A. Ad Hoc Networks

An ad hoc network is formed by a cluster of wireless terminals without the infrastructure of base stations. Based on the range of their radio transceivers, two nodes (wireless terminals) may communicate directly if they are close enough. Otherwise, they communicate indirectly by having one or more intermediate nodes relay their packets. Hence, a strong requirement of such a network is that every node should have the capability of forwarding packets for other nodes and thus act as intermediate routers. The system becomes more complex when mobility is introduced within the network. Such an ad hoc network comprising of mobile nodes is popularly called a mobile ad hoc network (MANET). MANETs are suited for use in situations where pre-deployment of network infrastructure is difficult or unavailable. A few examples include: fleets in oceans, battlefields, emergency search-and-rescue operations, meetings or conventions in which persons wish to quickly share information, and so on [8]. In many cases, ad hoc networks are the only possible way of establishing temporary communication, as there is no time to bring in and setup the entire infrastructure that would be otherwise required. For certain networks that are expected to be only temporary, it is much more cost efficient to setup an ad hoc network, which can be easily dismantled and reused, by simply relocating the wireless terminals to new locations. In such scenarios, building an entire new infrastructure would not only be more costly but also, after the short lifetime of the network has expired it would be much harder to reuse the infrastructure by relocating to a new location. To stimulate research in ad hoc networks, a working group called MANET [5] has been formed by the Internet Engineering Task Force (IETF) .

Avishek Ghosal and Dilip Sarkar are with the Department of Computer Science, University of Miami. E-Mail: sarkar@cs.miami.edu

B. Problems associated with ad hoc networks

Despite the long history of ad hoc networking that dates back to 1972 with the DoD-sponsored Packet Radio Network (PRNET), there are still quite a number of open problems. The major ones relate to the issues of scalability, routing, media access, energy-efficiency, QoS provision and security. Most of these issues are interlinked and it is almost impossible to provide optimized solutions for each of them simultaneously. Hence, the research community has attempted to address these problems separately. Providing solutions to these issues are definitely not non-trivial as wireless ad hoc networks are characterized by the following properties, which are the basis for these problems.

- **Distributed Control.** There are no base stations for network control, routing or administration.
- **Wireless communication medium.** All communication occurs over the wireless medium that has, and will continue to have, significantly lower capacity than their wired counterpart. Moreover, due to effects of multiple access, fading, noise, and interference conditions, the realized throughput is often much less than a radio's maximum transmission rate.
- **Limited communication resources.** Resources like battery energy, bandwidth, processing capacity and memory are strictly limited and must be wisely preserved.

- **Lack of dedicated routers.** All nodes must act cooperatively to handle the functions of routing and media access.
- **Dynamic topology.** This problem is related to the MANET scenario where unpredictable topology changes make frequent re-computation of routes necessary.

The bulk of ad hoc networking research has been devoted to either routing or medium access control. Since this work is closely related to the issue of medium access, a brief discussion of the topic follows in the next section.

C. Medium Access Control (MAC) in ad hoc networks

MAC deals with the issue of accessing and using the shared communication medium (radio spectrum) efficiently and resolving potential contention and collision among the nodes that uses the medium. The dominant wireless media access protocol is currently the IEEE 802.11 standard, which follows the *carrier sense multiple access with collision avoidance (CSMA/CA)* paradigm. The most important requirement of this protocol is that for successful communication of two neighboring nodes, all other nodes that are within the transmission range of these nodes should not access the shared medium. This implies that if multiple pairs of nodes lie within the transmission range of each other and want to communicate, only one pair should be allowed to do so. This reduces the overall throughput of the system. Moreover, as the number of such communicating pairs increases, there will be a further degradation of network performance due to higher contention / collision. The motivation for the reported work arises from such a scenario and is discussed in the next section.

D. Contributions of this paper

An ad hoc network comprising of multiple multi-hop flows is considered where each node accesses the shared medium using the IEEE 802.11 MAC protocol. When more than one such flow cross each other, or are close enough, then packets belonging to those flows contend with each other for channel access, thereby reducing the overall system throughput. If these flows can be properly scheduled based on their direction, spatial coverage, and number of hops involved, the overall system throughput can be increased. This is the approach taken in this work. Certain scheduling policies are proposed and evaluated that prioritize the different flows in the network and aims to improve the overall system throughput.

The organization of the remaining text is as follows. Section II provides a review of the IEEE 802.11 MAC protocol. In Section III some of the existing multiple access protocols for throughput maximization are discussed. Topics include power control based protocols, multiple channel based protocols and a few others. Section IV presents the different scheduling strategies employed in this work. Detailed simulation results as well as analytical performance evaluations are provided in Section V. Finally, Section VI concludes the paper with directions for future work.

II. REVIEW OF IEEE 802.11 MAC

The IEEE 802.11 MAC protocol [4] is the current standard for wireless LANs and provides for both infrastructure mode and ad hoc mode operation. It has been extensively used in almost all test beds and simulations related to ad hoc network research. It covers the MAC and physical layers and defines a single MAC which interacts with different PHYs. Depending on the specifications of the physical layer, there are separate protocols viz 802.11a, 802.11b and 802.11g which collectively form the IEEE 802.11 family of protocols. The 802.11b standard, which transmits in an unlicensed radio spectrum at 2.4 GHz and has a data rate of 11 Mbps, is currently enjoying the most widespread deployment.

The 802.11 MAC layer defines two access methods - distributed coordination function (DCF) and point coordination function (PCF). The DCF mode uses a carrier sense multiple access with collision avoidance (CSMA/CA) scheme, whereas the PCF mode is a polling based access method and uses a point coordinator to determine which node has the right to transmit during each contention-free period. The PCF mode cannot be used in ad hoc networks and so we will limit our discussion only to the DCF mode. We first define the terms *transmission range*, *carrier sensing range* and *carrier sensing zone* which are necessary for precise understanding of DCF.

- **Transmission range:** A node within the transmission range of a sender node, can receive and correctly decode packets from the sender node.
- **Carrier sensing range:** When a node is within the carrier sensing range of a sender node, it can sense the sender's transmission. The carrier sensing range is typically larger than the transmission range and is assumed to be twice the transmission range in our simulations in Section V.
- **Carrier sensing zone:** This is the zone formed when the transmission range is excluded from the carrier sensing range. Nodes in the carrier sensing zone can sense a transmission but may not be able to decode packets correctly.

Figure 1 shows the transmission range, carrier sensing range, and carrier sensing zone for the node S. When S transmits a packet, nodes A and B being in the transmission range of S can receive the packet as well as decode it correctly. However, nodes X and Y being in the carrier sensing zone of S, can only sense the transmission and may not be able to decode the packet correctly.

A. DCF

DCF allows for automatic medium sharing between the nodes through the use of CSMA/CA and a random backoff time following a busy medium condition [4]. In DCF, both physical and virtual carrier sensing is used. The virtual carrier sensing mechanism works as follows. When a node has a DATA packet to send, and senses the channel to be idle for a Distributed Interframe Space (DIFS) period, it starts of by sending a RTS (Request To Send) control packet prior to sending the data packet. The receiver, on receiving the RTS waits for a short interval SIFS (Short Interframe Space) and then replies back with a CTS (Clear To Send) control

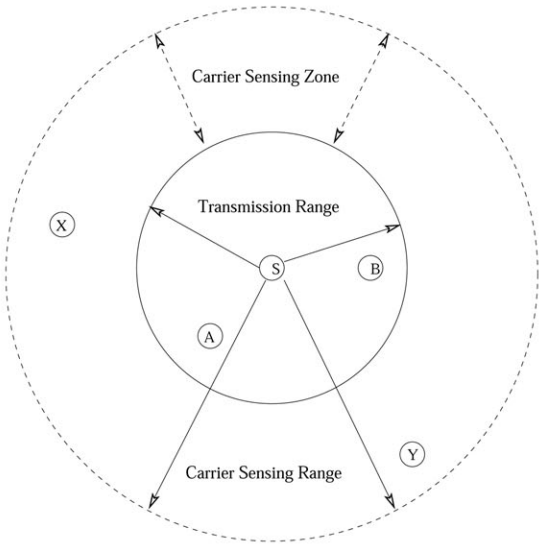

Fig. 1. Transmission Range, Carrier Sensing Range, and Carrier Sensing Zone with respect to a source node S.

packet. On receiving the CTS, the sender waits for a SIFS interval and sends the DATA packet. After the successful reception of the DATA packet, the receiver responds back with an acknowledgement (ACK) after a SIFS interval to ascertain a successful data transfer operation. If an ACK is not received by the sender, the data frame is presumed to be lost, and a retransmission is rescheduled. The headers of RTS, CTS and DATA packets include the expected duration of time for which the channel will be in use. When other nodes overhear these packets, they defer their transmission for the duration specified in these packets. Each node maintains a variable called Network Allocation Vector (NAV) that records the duration of time a node must defer its transmission. The virtual carrier sensing operation is illustrated in Figure 2.

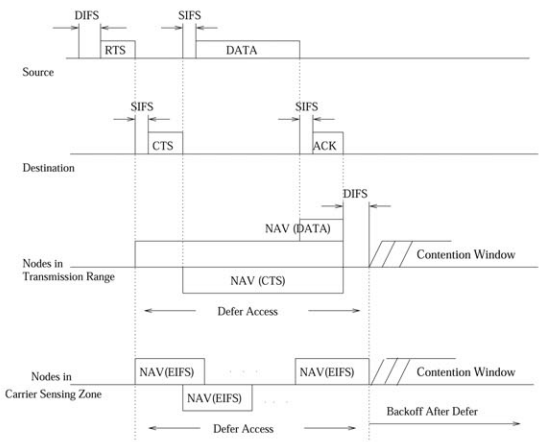

Fig. 2. Operation of IEEE 802.11 DCF

Figure 2 shows how nodes in transmission range and the carrier sensing zone adjust their NAVs during RTS-CTS-DATA-ACK transmission. The nodes in transmission range correctly set their NAVs when receiving RTS or CTS. However, since nodes in the carrier sensing zone cannot decode the packet, they do not know the duration of the packet transmission. To prevent a collision with the ACK reception at the sender, nodes in the carrier sensing zone set their NAVs for EIFS (Extended Interframe Space) duration. The main purpose of EIFS is to provide enough time for a source node to receive the ACK frame, and hence the duration of EIFS is longer than that of an ACK transmission. It is also to be noted that a node waits for DIFS before transmitting RTS, but waits for SIFS before sending CTS or ACK, which is shorter. So an ACK packet will win the channel when contending with RTS or DATA packets.

1) Random backoff in DCF: Initially, when a node has a packet to send, and senses the channel to be idle for a DIFS period, it proceeds with the transmission. If the medium is detected busy, it waits till the channel is idle for a DIFS interval and then further waits for a random backoff period before transmitting. The backoff timer counter decreases as long as the channel is sensed idle, freezes as soon as the channel becomes busy and starts decreasing again if the channel becomes idle for more than DIFS duration. As soon as the backoff timer reaches zero, the node can start transmitting. The backoff time is uniformly chosen from a Contention Window having the range [0, CW], where CW is an integer within the range of values determined by the PHY characteristics CWmin and CWmax, $CWmin \leq CW \leq CWmax$. With each unsuccessful transmission, CW gets doubled till it reaches CWmax and remains there till a successful transmission occurs when its value is reset to CWmin.

III. PROPOSED METHODS FOR THROUGHPUT MAXIMIZATION

Several approaches have been proposed to improve the throughput of wireless ad hoc networks. This section provides an overview of these approaches.

A. Power control based methods

The idea behind all power control schemes is to allow the nodes to transmit at varying power levels. This improves spatial reuse of the wireless channel and hence accounts for increased system throughput. The idea is explained using Figure 3a, where there is an ongoing communication from node A to node B. The circles around the nodes represent their transmission ranges. The communication between nodes C and D cannot be granted because A's signal will interfere with C's. Similarly, communication between nodes F and E cannot be granted because E is within A's transmission range. However, as shown in Figure 3b, if each node's transmit power level is properly tuned, all communication pairs can coexist without any interference. The idea is to have the sender transmit with power just enough to reach the target node, so that the space blocked by that particular transmission is minimized. Besides spatial reuse, power control has another advantage - the battery energy of the wireless nodes may be sustained for a longer period.

A simple power control protocol has been proposed based on an RTS-CTS handshake in the context of IEEE 802.11 [1], [3]. In this scheme, the RTS and CTS control packets

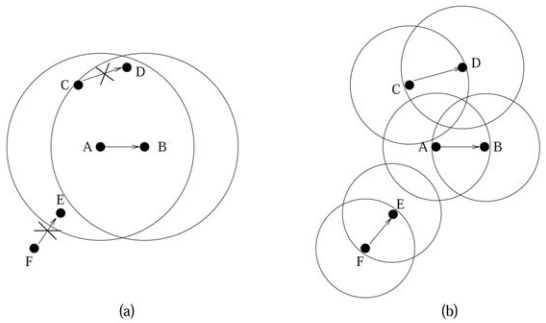

Fig. 3. Transmission scenarios (a) without power control and (b) with power control

are transmitted using the highest power level and, DATA and ACK packets are transmitted using the minimum power level necessary for the nodes to communicate. However, the main goal of this scheme is energy saving rather than throughput maximization. The PCMA (power controlled multiple access) protocol proposed in [6], on the other hand, uses power control as a mechanism for increasing channel efficiency rather than for increasing battery life. It uses two channels, one for "busy tones", and the other for all other packets. While a node is receiving a DATA packet, it periodically sends a busy tone. The power level at which the busy tone is transmitted by a node is equal to the maximum additional noise the node can tolerate. Any node wishing to transmit a packet first waits for a fixed duration (determined by the frequency with which nodes transmit busy tones when receiving data), and senses the channel for busy tones from other nodes. The signal strength of busy tones received by a node is utilized to determine the highest power level at which this node may transmit without interfering with other on-going transmissions. As shown in [6], PCMA improves the throughput performance by more than a factor of 2 as compared to IEEE 802.11 protocol standard.

B. Use of Multiple channels

The use of multiple channels can enhance system throughput, since, multiple transmissions can take place simultaneously in separate channels without interfering with each other. Many studies have shown the benefit of using multiple channels. Two generic approaches — dynamic channel assignment and modification of IEEE 802.11 DCF — are discussed here.

Reference [11] proposes the *Dynamic Channel Assignment* (DCA) protocol that assigns channels dynamically, in an on-demand style. In this protocol, one dedicated channel is maintained for control messages, and other channels for data. Each node has two transceivers, so that it can listen on the control channel and the data channel simultaneously. RTS/CTS packets are exchanged on the control channel, and DATA packets are transmitted on the data channel. In RTS packet, the sender includes suggested data channel information according to the channel condition around itself. The receiver, on receiving RTS, decides which channel to communicate and includes the selected channel information in CTS packet. Then DATA and ACK packets are exchanged on the agreed data channel. This protocol does not need synchronization and can utilize multiple channels with little control message overhead. However, it has two distinct disadvantages. First, it requires that every node should be equipped with two transeivers. Second, it does not perform well in an environment where the number of available channels is less and all the channels have equal bandwidth. The IEEE 802.11 standard provides such an environment. It already has multiple channels available for use, though its MAC protocol is designed for using a single channel. Table I summarizes the features of IEEE 802.11a and IEEE 802.11b standards. It can be seen from Table I that if the DCA protocol is used for IEEE 802.11b devices, which has 3 channels, 33% of the total bandwidth is wasted as control overhead.

	802.11b	**802.11a**
Physical Layer	DSSS with CCK	OFDM
Theoretical Capacity	11 Mbps	54 Mbps
Real Maximum Throughput	6 Mbps	31 Mbps
Spectrum	2.4 GHz	5 GHz
Number of Channels	3	12

TABLE I
FEATURES OF IEEE 802.11 STANDARDS

Another multi-channel MAC protocol is proposed in [9] that modifies IEEE 802.11 DCF and requires only one transceiver for each node. The protocol uses *ad hoc traffic indication message* (ATIM) windows as in power saving mode (PSM) of IEEE 802.11 DCF [4]. The nodes in the network are synchronized by beacons, and the channels are negotiated in the ATIM window using ATIM messages. After the ATIM window, nodes switch to their selected channel and exchange messages on that channel for the rest of the beacon interval. No separate control channel is necessary for this protocol and hence bandwidth wastage due to control overhead is also less.

C. Other methods

Some other methods have also been proposed for increasing system throughput. One such approach is to use directional antennas instead of omnidirectional antennas [7]. Directional antennas are able to transmit signal in one direction, so that the nodes located in other directions can communicate concurrently without interfering with each other.

IV. THROUGHPUT MAXIMIZATION BY SCHEDULING END-TO-END FLOWS

In this Section, we describe our network model and present the details of the proposed scheduling strategies.

A. Description of the Network Model

The Network model considered here consists of a rectangular region of given dimensions (say L X W) as shown in Figure 4. The region encloses a variable number of wireless nodes (represented by little circles), which form an ad hoc network. Each node is assumed to have a transmission range of t such that $t < L$. This ensures that a packet transmitted by a node at one end of the region requires more than one hop

to reach a destination node at the other end of the region. A fixed number of nodes are placed uniformly in two rectangular strips located at the two opposite ends of the region. Both of these strips contain an equal number of nodes (say *x*). The nodes in one of the strips are assumed to be source nodes that can initiate a flow (explained in Section IV-B). Similarly, the *x* nodes in the opposite strip are assumed to be destination nodes (end points of flows). As shown in Figure 4, the source nodes are numbered $S_1, S_2, S_3, \ldots S_x$, and the destination nodes are numbered $D_1, D_2, D_3, \ldots D_x$. The inner rectangular region between the two strips contains a variable number of nodes that are responsible for routing of packets between source and destination nodes. None of these intermediate nodes initiate a flow. Hence, there can be at most *x* simultaneous flows in the network.

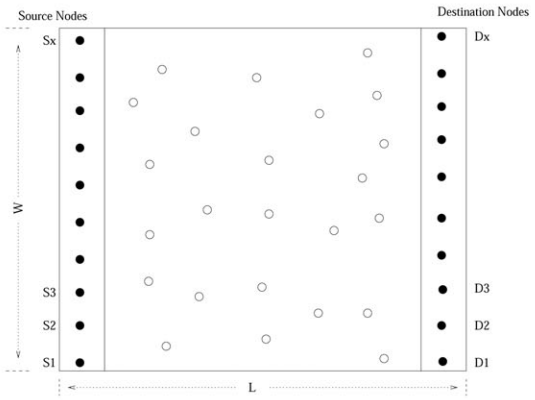

Fig. 4. Network Model. Source and Destination nodes are represented by black circles

Before describing the scheduling strategies in detail, the assumptions for this work are summarized below.

- Every node in the network accesses the shared communication channel by a MAC protocol similar to the IEEE 802.11 MAC protocol. In fact, the simulation results presented in Section V-E are based on an implementation of the IEEE 802.11 standard in the NS-2 simulator [2].
- All the nodes have the capability of forwarding packets for other nodes.
- Path determination between a source-destination pair is done by a shortest path algorithm.
- The nodes are static and their positions do not change for the duration of a simulation run.

The next section describes the strategies employed to maximize the number of active flows or the total system throughput in the network.

B. Proposed scheduling strategies

We first explain some of the key terms necessary for understanding the proposed scheduling strategies.

- **Flow**. It refers to a complete path between a source-destination pair that wish to communicate. In this work, a flow is represented in the format $(S_a \rightarrow D_b)$ where S_a is the source node and D_b is the destination node.
- **Active Flow**. It is a flow that is involved in data transmission.
- **Parallel flow**. It is a flow such that the source node and the destination node lie in the same relative position at the two ends of the network. By same relative position it is meant that the source and destination nodes have equal *y* coordinates in a cartesian coordinate system having *x-axis* and *y-axis* parallel to the length and width respectively of the considered rectangular region. With respect to Figure 4, flows between the pairs $(S_1 \rightarrow D_1)$, $(S_2 \rightarrow D_2)$, $\ldots (S_x \rightarrow D_x)$ represent parallel flows. Thus, a flow can be considered a parallel flow if the subscript of source and destination number are equal.

1) Flow scheduling by sorting of relative positional differences of source-destination pairs: In this scheme, the flows are scheduled after sorting the differences between the relative positions of all source-destination pairs. Following the source-destination node numbering scheme discussed earlier, the difference between the relative position of a source-destination pair in a flow $(S_a \rightarrow D_b)$ is simply the difference in their subscripts.

$$Difference = |(a - b)|$$

It is to be noted that we consider the absolute value of the difference here. The minimum possible difference is zero, which implies a parallel flow and the maximum possible difference is *(x-1)*, which implies a flow between two nodes located at the opposite corners of the network. After sorting, the flows are assigned priorities, with the flow having the minimum difference between the relative position of its source and destination getting the highest priority. In case of two or more flows having the same difference in the relative positions of their source and destination, the priorities are assigned to them randomly.

We now illustrate this scheduling policy with an example. Consider a network with 10 source and destination nodes ($x = 10$). Assume that traffic exists for the flows $(S_1 \rightarrow D_3)$, $(S_2 \rightarrow D_7)$, $(S_3 \rightarrow D_{10})$, $(S_4 \rightarrow D_4)$, $(S_5 \rightarrow D_2)$, $(S_6 \rightarrow D_5)$, $(S_7 \rightarrow D_8)$, $(S_8 \rightarrow D_6)$, $(S_9 \rightarrow D_9)$, and $(S_{10} \rightarrow D_1)$. The following steps are executed in order.

- Computation of relative positional differences, which yields the values 2, 5, 7, 0, 3, 1, 1, 2, 0, and 9 respectively for the above flows.
- Sorting the differences in ascending order yielding 0, 0, 1, 1, 2, 2, 3, 5, 7, 9.
- Assignment of priorities to the flows. Scheduling is done based on the priorities of the flows.

The priority assignment for the above flows is shown in Table II.

In Table II, a smaller number in the 'Priority' column indicates a higher priority, with 1 and 10 being assigned to the highest priority and lowest priority flows respectively. A higher priority flow gets access to the shared medium in preference to a lower priority flow. The logic behind this scheme can be explained with the help of Figure 5, which represents a schematic diagram of the flows in Table II. In the absence of scheduling, packets belonging to the different flows will compete with each other for medium access. Thus, if flow $(S_{10} \rightarrow D_1)$ wins

Flow	Difference between relative positions of source and destination	Priority
$(S_4 \rightarrow D_4)$	0	1
$(S_9 \rightarrow D_9)$	0	2
$(S_6 \rightarrow D_5)$	1	3
$(S_7 \rightarrow D_8)$	1	4
$(S_1 \rightarrow D_3)$	2	5
$(S_8 \rightarrow D_6)$	2	6
$(S_5 \rightarrow D_2)$	3	7
$(S_2 \rightarrow D_7)$	5	8
$(S_3 \rightarrow D_{10})$	7	9
$(S_{10} \rightarrow D_1)$	9	10

TABLE II
ASSIGNMENT OF PRIORITIES TO FLOWS BY SORTING THE DIFFERENCES IN THE RELATIVE POSITIONS OF SOURCE-DESTINATION PAIRS

Flow	Difference between relative positions of source and destination	Priority
$(S_4 \rightarrow D_4)$	0	1
$(S_9 \rightarrow D_9)$	0	2
$(S_6 \rightarrow D_5)$	-1	3
$(S_7 \rightarrow D_8)$	1	4
$(S_8 \rightarrow D_6)$	-2	5
$(S_1 \rightarrow D_3)$	2	6
$(S_5 \rightarrow D_2)$	-3	7
$(S_2 \rightarrow D_7)$	5	8
$(S_3 \rightarrow D_{10})$	7	9
$(S_{10} \rightarrow D_1)$	-9	10

TABLE III
ASSIGNMENT OF PRIORITIES TO FLOWS IN CASE OF DIRECTIONAL SORTING POLICY

access to the medium, all the remaining flows will get affected adversely and the overall system throughput will decrease drastically. However, with scheduling, the high priority flows $(S_4 \rightarrow D_4)$, $(S_9 \rightarrow D_9)$, $(S_6 \rightarrow D_5)$, $(S_7 \rightarrow D_8)$ and $(S_1 \rightarrow D_3)$ get access to the shared medium one after the other and may exist simultaneously, thereby accounting for a much higher system throughput. By prioritizing the flows based on the difference in the relative positions of source and destination, it is ensured that the flows affecting the minimum spatial area gets preferential access to the shared medium. It is to be noted however, that though the flows have been represented by straight arrows in Figure 5, the actual routes involving intermediate nodes may cover a much larger spatial area depending on the positions of the intermediate nodes. The simulation results for this scheme are presented in Section V-C.

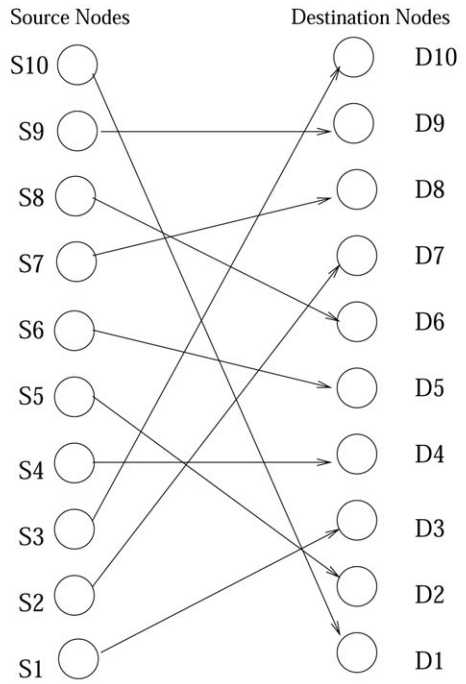

Fig. 5. Schematic diagram of 10 end-to-end flows. Only the source and destination nodes, and not the intermediate nodes are shown.

2) Flow scheduling by Directional Sorting: This scheme is a modified version of the previous scheme with the direction of the flows also taken into account. While we were considering only the magnitude of the differences in the previous case, here the signs are also retained. The assignment of priorities to flows follows the exact procedure as before with only one variation. The variation occurs for flows having the same difference in the relative positions of source and destination, but with different signs. Instead of randomly assigning priorities to such flows, either the positive or the negative difference is given a preference. It does not matter whether the positive difference is given a priority or the negative difference, as long as the same policy is maintained for all equal magnitude differences. In our simulations, the negative differences were given a priority over the positive differences. If both the magnitude and sign of the difference for two flows is same, the tie is again broken arbitrarily. Table III illustrates the priority assignment of flows in case of directional sorting for the sample flows considered in the previous subsection. On comparing Tables II and III, it can be observed that only the priorities for flows $(S_8 \rightarrow D_6)$ and $(S_1 \rightarrow D_3)$ have changed.

C. Flow scheduling based on sorting of hop counts of flows

In this scheme, the flows are scheduled by sorting the number of hops associated with them. After sorting the hop-counts in ascending order, the flows are assigned priorities as in the previous two methods. The flows are then scheduled in the order of their priorities. The idea behind this scheme is based on the fact that a flow involving a larger number of hops will cover a larger spatial area than a flow involving a smaller number of hops. Since our aim is to prioritize flows that cover a smaller spatial area, we adopt this technique. We have simulated this scheme in both NS2 as well as our own simulator. The results are presented in Sections V-C and V-E respectively.

V. SIMULATION AND ANALYTICAL RESULTS

In this Section, the simulation results for the scheduling strategies described in Section IV-B, as well as analytical performance evaluations are presented. We have chosen *number of active flows* as our performance evaluation metric, which is

an indication of the system throughput. The simulations are based on a graph model of the network topology where the vertices of the graph represent the nodes (wireless terminals) and the edges represent possible communication links between the nodes. We assume error-free channels and hence if two nodes are within the transmission range of each other, they can communicate without channel errors. We further assume that packets belonging to the same active flow do not contend with each other for channel access. We simulate three network models (see Section 4). Table IV provides details of the parameters of the models. The transmission range and carrier sensing range of the nodes are assumed to be $100m$ and $200m$ respectively for all the network models. These ranges correspond roughly to those of IEEE 802.11b terminals.

The positions of the source and destination nodes were kept fixed for all simulation runs. Their placement in the rectangular strips is such that adjacent source (and adjacent destination) nodes are apart by a distance that is greater than the transmission range of the nodes. This ensures that, no source or destination node can be part of a flow in which it itself is not the source or destination. However, adjacent source or destination nodes do lie in the carrier sensing zone of one another, which implies that two adjacent source nodes cannot have an active flow at the same time. Thus, the maximum number of simultaneous active flows possible for our simulation models is equal to half the number of source or destination nodes. For each simulation run, the positions of the intermediate nodes are generated from a uniform distribution, and hence vary with each simulation run.

In Figures 6, 7, and 8, results from extensive simulations for the three network models are shown. For models I and II, 10 source destination pairs are assigned whereas that for model III are 20. For the random source-destination plot, each data point is obtained by averaging the number of active flows for 800 simulation runs. On the other hand, the data points for the parallel flows are obtained by averaging 1000 simulation runs.

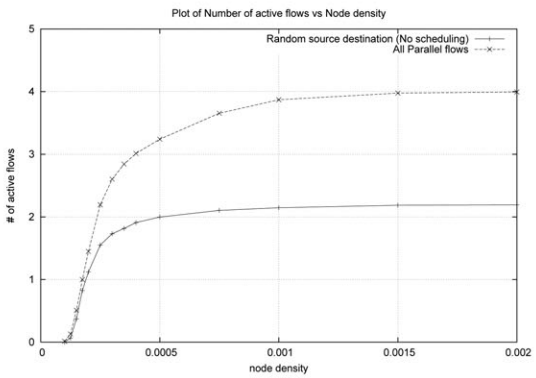

Fig. 6. Total achievable active flows with varying node density for Model I

The reason for plotting these two cases is to get an indication of the difference in system throughput between the best scenario (all parallel flows) and an average scenario (random flows). Our aim is to minimize this difference. All the three figures show that when the node density is smaller

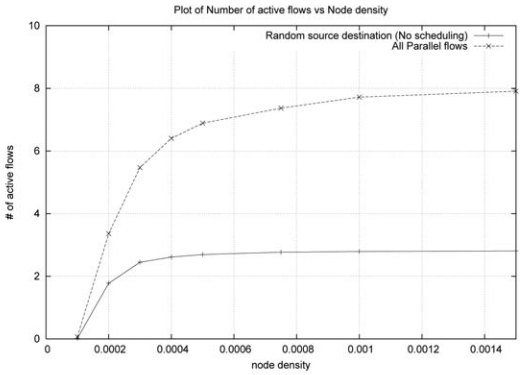

Fig. 7. Total achievable active flows with varying node density for Model II

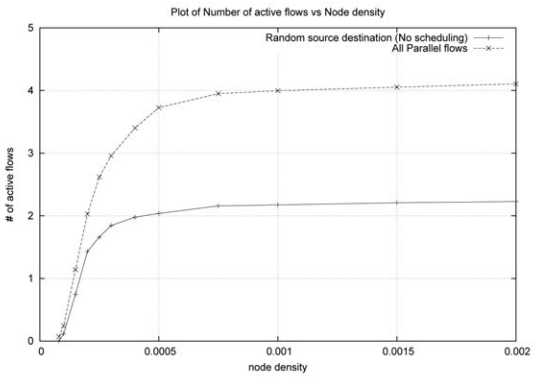

Fig. 8. Total achievable active flows with varying node density for Model III

than about $0.0001 nodes/m^2$, the number of active flows is negligible. This is because, there are too few intermediate nodes to form a route between any source-destination pair. With the increase in node density, the number of active flows increases as more routes are able to form between source-destination pairs. The number of active flows for parallel flows is significantly greater than that for random source-destination pairs, for node densities above $0.00025 nodes/m^2$. This is a clear indication that flows involving larger spatial area degrade system performance and hence the need for scheduling of flows.

The plots for parallel flows asymptotically approach the number of maximum achievable active flows for each model. Maximum active flows are obtained when the flows take near straight line paths. This is only possible when sufficient intermediate nodes lie on or very close to the straight lines joining source and destination nodes. The probability of such a situation increases with node density and hence the nature of these plots. On comparing Figures 6 and 8, it can be observed that more number of active parallel flows are obtained for model III than model I for same node densities, though both models I and III have the same number of source and destination nodes. This can be explained as follows. Model III being half in width of model I, involves approximately half the number of hops for each flow. A smaller number of hops indicate a smaller number of intermediate nodes that can be displaced from the straight line paths, which in turn implies

Parameters	Model I	Model II	Model III
Network area dimensions	$1100mX1100m$	$1000mX2200m$	$550mX1100m$
Rectangular strip dimensions	$50mX1100m$	$40mX2200m$	$25mX1100m$
# of source / destination nodes	10	20	10
Maximum possible Active Flows	5	10	5

TABLE IV
SIMULATION MODEL PARAMETERS

a higher probability of straight line paths for the same node density.

The difference in the number of active flows for parallel and random case is much more pronounced for model II, where the number of source and destination nodes is double that of the other two models. This indicates that there is more scope of improvement of system throughput when there are more number of flows. Before presenting simulation results of our scheduling schemes, we first provide some analytical results to evaluate the accuracy of our simulator. The analytical performance evaluation is done for two cases. In the first case, we provide an analysis for a constrained network model, where the intermediate nodes are allowed to have only specific positions. This makes the analysis relatively simpler. For the second case, however, we remove this restriction and provide the analysis for our general network model.

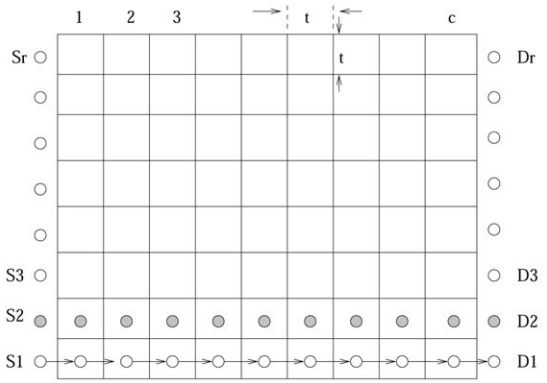

Fig. 9. Division of network area into a grid. Nodes are placed at the center of boxes. If there is an active flow through row 1, row 2 cannot have an active flow.

A. Analytical performance evaluation - Case I

We divide the inner rectangular region enclosing the intermediate nodes into a grid of r rows and c columns. The values of r and c are obtained by dividing the length and width respectively of the rectangular region by *t*, the transmission range of nodes. Thus, each box in the grid is a square of $side = t$. The last column or row of boxes might have $side < t$ in case the length or the breadth of the rectangular region are not exact multiples of *t*. However, we proceed with our analysis assuming all the boxes to be squares of equal size. Let the total number of boxes thus obtained be N_b. Since the intermediate nodes are placed randomly with a uniform distribution, the probability *p* of a node being present in a particular box is given by

$$p = \frac{1}{N_b} \tag{1}$$

Let the total number of intermediate nodes be *N*. The probability of no nodes being present in a particular box is $(1-p)^N$, which means that the probability of existence of at least one node in a particular box , *P* is

$$P = 1 - (1-p)^N = 1 - (1 - \frac{1}{N_b})^N \tag{2}$$

Now lets consider Figure 9, which represents our network model after dividing it into grids.

It is assumed that whenever a node is placed in a box, it is placed at the center of the box. Since the distance between the centers of two consecutive boxes is equal to the transmission range of the nodes, the presence of at least one node in every box of a row guarantees a parallel flow through that row of boxes. The probability of such a parallel flow is given by $P(parallel flow) = P' = P^c$, as *P* is independent for two or more boxes. Now lets estimate the number of active flows for this system. We start from row 1 and move upwards toward row *r*. The probability of an active flow through row 1 (P_1) is simply P' as it is not influenced by any other active flow. The probability of an active flow through row 2 (P_2), is however given by

$$P_2 = P' \times (1 - P_1) = P' \times (1 - P') = P' - P'^2 \tag{3}$$

This is because, an active flow through row 2 can only occur if there is no active flow through row 1. In a similar manner, the probability of active flows through rows 3, 4, ...r is given by

$$\begin{aligned} P_3 &= P' \times (1 - P_2) \\ &= P' \times (1 - P' \times (1 - P')) \\ &= P' - P'^2 + P'^3 \\ P_4 &= P' \times (1 - P_3) \\ &= P' - P'^2 + P'^3 - P'^4 \\ &\dots \\ P_r &= P' \times (1 - P_{r-1}) \\ &= \textstyle\sum_{i=0}^{r-1} (-1)^i \times P'^{(i+1)} \end{aligned}$$

The total number of active flows for this system can be computed by simply adding the probabilities P_1, P_2, P_3, $\dots P_r$. Thus,

$$Total\ no\ of\ active\ flows = P_1 + P_2 + P_3 + \dots + P_r \tag{4}$$

$$= \sum_{i=0}^{r-1} (-1)^i \times (r - i) \times P'^{(i+1)} \tag{5}$$

The analytical estimates obtained from Equation 5 were verified simulation results. In order to obtain a correspondence with the analytical model, the randomly generated intermediate nodes during the simulation runs were placed at the center of the grids in which they happen to lie. Figure 10 shows the plots obtained using Equation 5 and from simulation of the network model I, with $r = c = 10$ and $N_b = 100$. The very small difference between the two curves is a verification of the accuracy of the analytical model . In the next subsection, we remove the restriction of placing nodes at the center of grid boxes and provide a more general analysis.

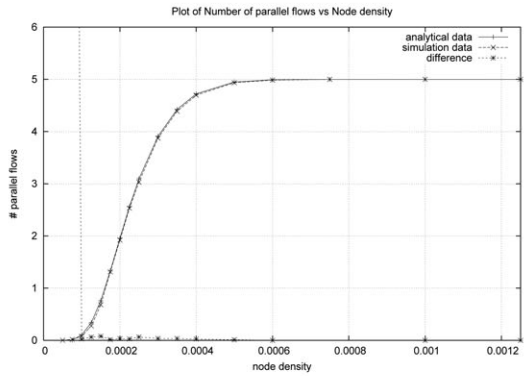

Fig. 10. Comparison of Analytical and Simulation results when nodes are placed at the center of grids.

B. Analytical performance evaluation - Case II

In this section we attempt to find the average distance between two nodes that are part of the same flow. That will give us the average number of hops for an active flow, which we can compare with our simulation results. Consider Figure 11, which shows half the area covered by the transmission range of a node that is part of a flow. Our aim is to find the distance of the next node that can be part of this flow.

The probability of a node lying in the elemental strip is equal to dA/A, where dA is the area of the elemental strip, and A is the area of the entire (rectangular) region. Thus,

$$P(\text{at least 1 node in } dA) = 1 - (1 - \frac{dA}{A})^N$$

If the above equation is expanded using binomial expansion and the second and higher order terms are neglected, we get

$$P(\text{at least 1 node in } dA) = 2N \times \frac{\sqrt{(t^2 - x^2)}dx}{A} \quad (6)$$

In Equation 6, t is the transmission range of a node. The probability of no nodes lying in the shaded area is equal to $(1 - A_s/A)^N$, where A_s is the area of the shaded region and is given by

$$A_s = t^2 \times \arccos(x/t) - x \times \sqrt{(t^2 - x^2)}$$

The probability of selecting a node from the elemental strip *P(S)*, is the product of the probability of at least 1 node in the strip and the probability of no nodes in the shaded area. This gives

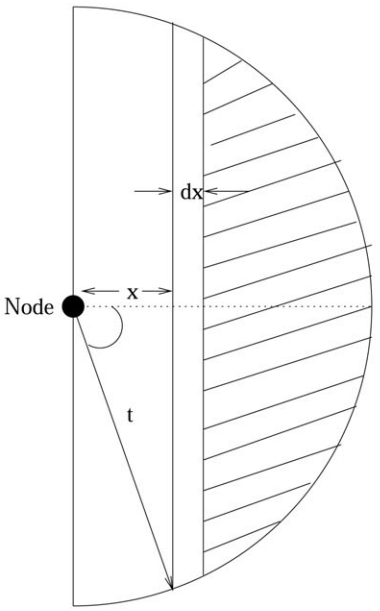

Fig. 11. Estimation of average distance of next node in flow

$$P(S) = \frac{2N}{A} \times \sqrt{(t^2 - x^2)} \times \left(1 - \frac{t^2 \times \arccos(x/t) - x \times \sqrt{(t^2 - x^2)}}{A}\right)^N dx \quad (7)$$

The average distance of the selected node x_{avg}, can be obtained by integrating Equation 8 over the semicircular region shown in Figure 11. Thus,

$$x_{avg} = \frac{2N}{A} \int_0^t \sqrt{(t^2 - x^2)} \times \left(1 - \frac{t^2 \times \arccos(x/t) - x \times \sqrt{(t^2 - x^2)}}{A}\right)^N \times x\, dx \quad (8)$$

By substituting $x = t\cos\theta$, Equation 9 can be rewritten as:

$$x_{avg} = \frac{2Nt}{a} \int_0^{\pi/2} \cos\theta \sin^2\theta \times (1 - \frac{\theta - \cos\theta \sin\theta}{a})^N d\theta \quad (9)$$
$$where,\ a = A/t^2$$

On expanding the term $(1 - \frac{\theta - \cos\theta \sin\theta}{a})^N$ in Equation 9, and after further simplification, we arrive at the following result:

$$x_{avg} = \frac{2Nt}{a} \sum_{i=0}^{N} \sum_{j=0}^{i} (-1)^{i+j} \binom{N}{i} \binom{i}{j} \times \int_0^{\pi/2} \frac{\theta^{i-j} \cos^{j+1}\theta \sin^{j+2}\theta}{a^i} d\theta \quad (10)$$

A closed form expression could not be obtained because the integral produces a different result for each combination of *i* and *j*. Thus, the only possible way to get x_{avg} is to

use numerical integration. We used *Simpson's Rule* and the obtained values for model I are shown in Figure 12. The Figure actually plots the *average number of hops*, which is obtained by dividing the distance between a source-destination pair belonging to a parallel flow by x_{avg}.

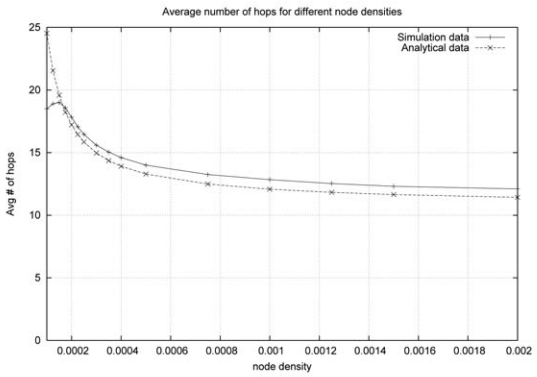

Fig. 12. Comparison of Analytical and Simulation results for model I

C. Results with scheduling policies

In this section, we present the simulation results for the three network models with the previously described scheduling strategies enforced. Figures 13, 15, and 17 are for the three network models respectively. It can be seen that the performance of the three scheduling schemes is very similar. The *Directional sorting* scheme performs slightly better than the other schemes at high node densities for all the models. For low node densities, the *sorting on hop count* scheme slightly outperforms the other two schemes. This is more evident for model I where the length of the network area, and hence the average number of hops per flow, is the greatest. When the node density is low, fewer flows are able to form. Further, these flows take non-linear curvy paths and, on an average, involve a larger number of hops than when for higher densities. In such a situation, a flow with a higher difference in the relative position of its source and destination may actually cover a smaller spatial area than that by a flow having a lower difference. Thus, *sorting on hop count* proves more benefitial than the other two methods. Figures 14, 16, and 18 show the improvement achieved with the proposed scheduling methods. The improvement is calculated as follows:

$$\text{Improvement} = I = \frac{F_{ws} - F_{wos}}{F_{wos}}$$

where, F_{ws} and F_{wos} are the number of active flows with and without scheduling, respectively.

It can be observed that though the number of active flows increases with node density, no appreciable increase in improvement takes place with the increase in node density. Also, as the number of source-destination pairs increases, a greater overall improvement is achieved. Thus, model II with 20 source-destination pairs shows the highest improvement.

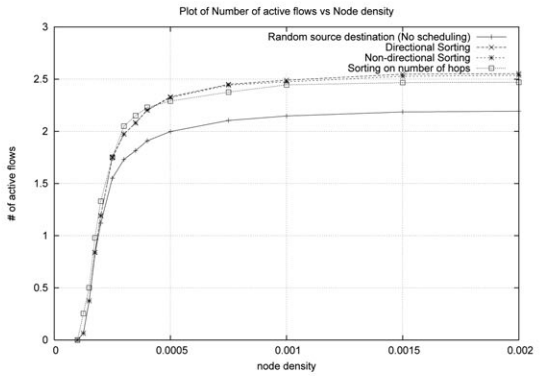

Fig. 13. Performance Comparison of different scheduling policies with no scheduling for Simulation model I

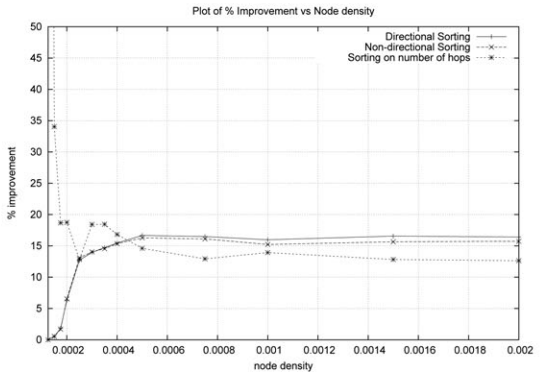

Fig. 14. Percentage Improvement with different scheduling policies for Simulation model I

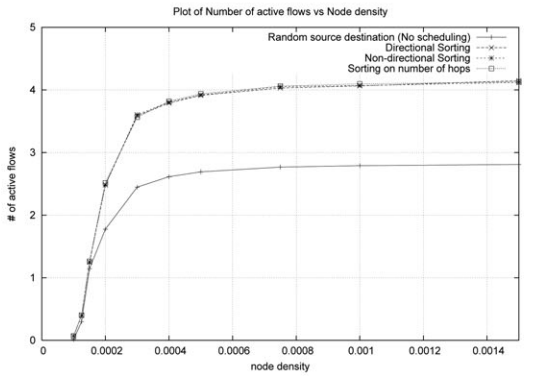

Fig. 15. Performance Comparison of different scheduling policies with no scheduling for Simulation model II

D. Results for a multi-channel MAC protocol

We have also simulated a multi-channel MAC protocol besides the proposed scheduling policies. The motivation for using multiple channels arises from the fact that IEEE 802.11 standard already has multiple channels available for use. IEEE 802.11b physical layer has 14 channels, 5MHz apart in frequency. But to be totally non-overlapping and thus feasible for use in the same region, the frequency spacing must be at least 25MHz. So channels 1, 6, and 11 can be used for simultaneous communication, and thus we have 3 channels

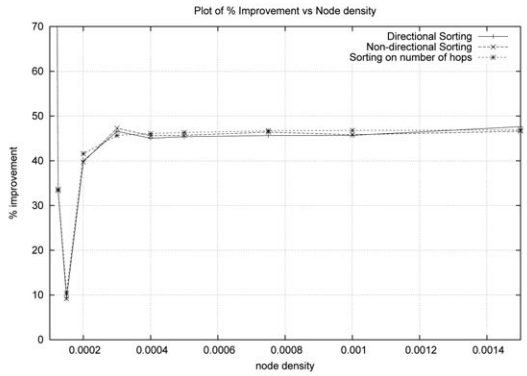

Fig. 16. Percentage Improvement with different scheduling policies for Simulation model II

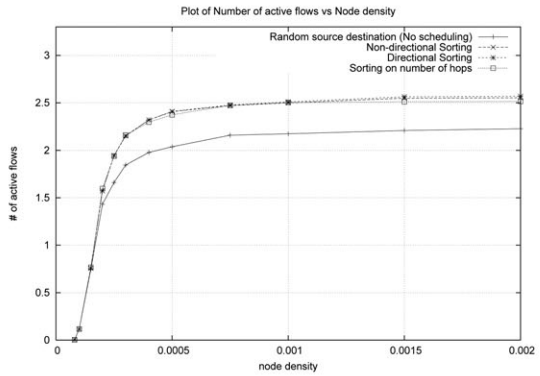

Fig. 17. Performance Comparison of different scheduling policies with no scheduling for Simulation model III

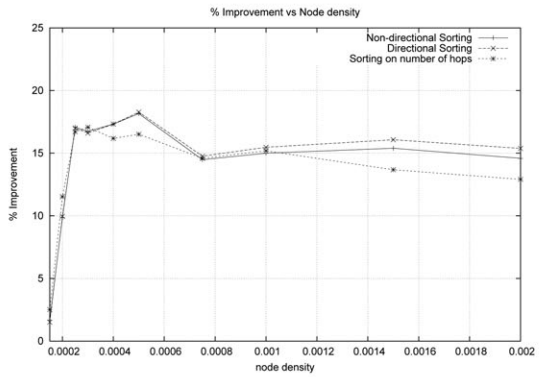

Fig. 18. Percentage Improvement with different scheduling policies for Simulation model III

available for use (as shown in Table I). IEEE 802.11a provides 12 channels, 8 in the low part of the band for indoor use and 4 in the upper part for outdoor use. The IEEE MAC protocol, however, is designed for sharing a single channel only. This is because, each IEEE 802.11 host is equipped with only one half-duplex transceiver. So, it can only transmit or listen on one channel at a time.

The multi-channel MAC protocol simulated here is similar to the one proposed in [9]. Every node maintains a list of channels. A pair of nodes that wish to communicate chooses a channel from this list such that the chosen channel is not being used by any other pair of communicating nodes in their respective carrier-sensing zones. However, nodes belonging to the same flow are exempt from this restriction because of our intial assumption that packets belonging to the same flow do not compete for channel access. For this simulation, the restriction of separating adjacent source nodes or destination nodes by distances greater than the transmission range of nodes is removed. This is because, availability of multiple channel ensures that adjacent flows can be active at the same time. We use the simulation model I, with the difference that instead of having 10 source-destination pairs, we now have 20 pairs. Figure 19 shows the results with 1, 3, and 5 channels.

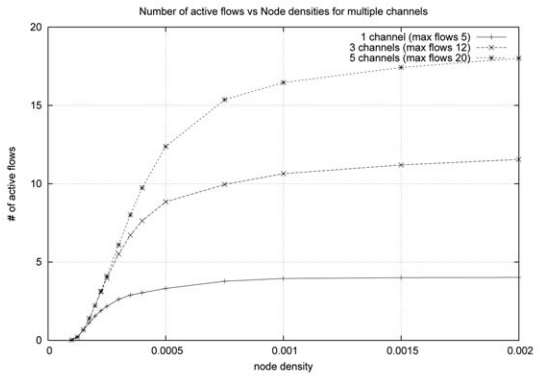

Fig. 19. Total achievable number of active flows using multiple channels

E. Simulation in NS-2

This part of the simulation is done in NS-2 [2]. We use 2 Mbps for the channel bit rate and a packet size of 512 bytes. Each flow in the network transmits CBR (Constant Bit Rate) traffic. The transmission range of the nodes is $250m$ which is the default in NS-2. All simulation results are the average of 8 runs and each simulation runs for 40 seconds of simulation time. We use a network model that is different from the three models presented earlier. The model consists of a rectangular region of $850m \times 1300m$, with 5 source and destination nodes placed at the two sides of the network. We had to use a different model because NS-2 gets over loaded for networks having around 100 or more nodes. For these simulations we use *system throughput* as our performance metric.

Figures 20 and 21 show the plots of overall system throughput against node density for parallel flows as well as random source-destination pairs, with packet arrival rates of 4 pkts/sec and 8 pkts/sec respectively. It is observed, that a greater arrival rate provides a greater opportunity for performance enhancement. This can be explained as follows. We know that when flows cross each other, packets contend for channel access. A higher arrival rate causes a greater number of packets to contend for channel access than for a lower arrival rate, which results in more number of collisions and retransmissions. Scheduling the flows in such a scenario can improve the system performance significantly. This is observed in Figure 22, which shows the results when the *sorting on hop count* scheme presented in Section IV-C is employed for an arrival

rate of 8 pkts/sec. The plots show an improvement of upto 30% with the scheduling scheme.

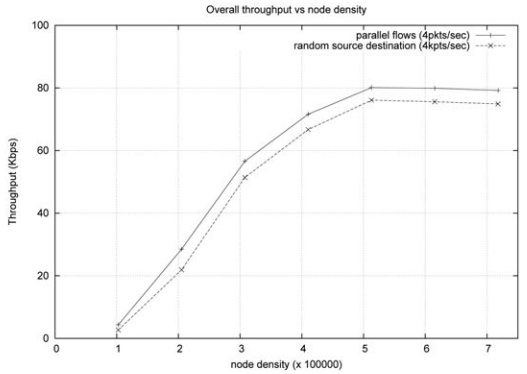

Fig. 20. Total system throughput with varying node density for arrival rate = 4 pkts/sec

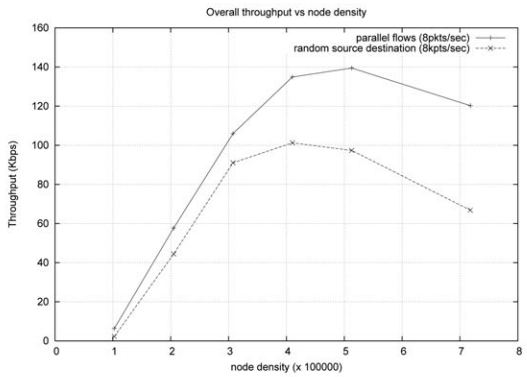

Fig. 21. Total system throughput with varying node density for arrival rate = 8 pkts/sec

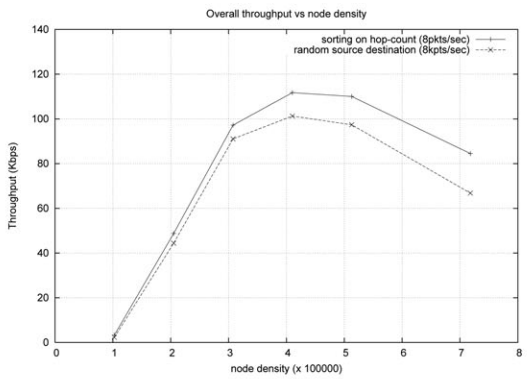

Fig. 22. Total system throughput with and without scheduling for arrival rate = 8 pkts/sec

VI. CONCLUSION

In this work, we presented some strategies for scheduling the flows in an ad hoc network in order to maximize system throughput. We assumed that the nodes access the shared communication medium using the IEEE 802.11 MAC protocol which is the *de facto* standard for wireless LANs. The proposed schemes were evaluated for different network models and the results show that significant improvement in terms of number of active flows or system throughput can be obtained by scheduling source destination pairs. We observed that the scheduling schemes produce a greater improvement under high load conditions, when a greater number of packets compete for channel access, resulting in more collisions and retransmissions. The choice of a particular scheme depends on the network scenario. For example, in case of networks having low node density and high average number of hops per flow, the *sorting on hop count* scheme outperforms the other schemes.

The *directional sorting* scheme can be implemented if the angular displacement of consecutive nodes in a flow is known. An enhancement of the routing algorithm so that it interacts with location based services like GPS (Global Positionioning System) can be used to determine the angular displacement. Scheduling can also be used to improve system throughput in mixed architectures comprising a centralized backbone as well as an ad-hoc network. In such cases, the backbone can act as a centralized scheduler that will have the information for all the flows in the network and it can choose a particular scheduling policy depending on the network scenario. Design of such a scheduler is the scope of future work.

REFERENCES

[1] S. Agarwal, S. Krishnamurthy, R. H. Katz, and S. K. Dao. Distributed Power Control in Ad-Hoc Wireless Networks. In *PIMRC'01*, 2001.

[2] Kevin Fall and Kannan Varadhan. *The ns manual (formerly known as ns Notes and Documentation)*. The VINT Project January 2003 (Work in Progress). http://www.isi.edu/nsnam/ns/ns-documentation.html.

[3] J. Gomez, A. T. Campbell, M. Naghshineh, and C. Bisdikian. Conserving Transmission Power in Wireless Ad-Hoc Networks. In *ICNP'01*, November 2001.

[4] IEEE Std. 802.11. *Wireless LAN Medium Access Control (MAC) and Physical Layer (PHY) Specifications*, 1999.

[5] IETF MANET Working Group. http://www.ietf.org/html.charters/manet-charter.html.

[6] J. P. Monks, V. Bharghavan, and W. mei W. Hwu. A Power Controlled Multiple Access Protocol for Wireless Packet Networks. In *INFOCOM 2001*, April 2001.

[7] A. Nasipuri, S. Ye, J. You, and R. Hiromoto. A MAC Protocol for Mobile Ad Hoc Networks using Directional Antennas. In *IEEE Wireless Communications and Networking Conference (WCNC)*, Chicago, IL, September 2000.

[8] E. M. Royer and C. K. Toh. A review of current routing protocols for ad hoc mobile wireless networks. *IEEE Personal Communications*, pages 46–55, April 1999.

[9] Jungmin So and Nitin H. Vaidya. A Multi-channel MAC Protocol for Ad Hoc Wireless Networks. Technical Report, January 2003.

[10] Ivan Stojmenovic, editor. *Handbook of Wireless Networks and Mobile Computing*. A Wiley-InterScience Publication, 2002.

[11] S.-L. Wu, Y.-C. Tseng, C.-Y. Lin, and J.-P. Sheu. A New Multi-Channel MAC Protocol with On-Demand Channel Assignment for Multi-Hop Mobile Ad Hoc Networks. In *IEEE Wireless Communications and Networking Conference (WCNC)*, Chicago,IL, September 2000.

Evaluation of the Location Privacy Aware Micromobility Domain Planning Scheme*

László Bokor† *Member IEEE,* Vilmos Simon† *Member IEEE,* Sándor Imre† *Member IEEE*

***Abstract*—Next generation telecommunication systems are converging into a synergistic union of wired and wireless technologies, where integrated services are provided on a universal IP-based infrastructure. The concept of global reachability fuelled with the advanced mobility schemes and the "anytime, anywhere" paradigm caused that the requirements for security and privacy in the global Internet era differs a lot from the ones of a decade ago. We focus on a subset of this complex problem space and consider location privacy issues defined by the information leakage of IP addresses during the movement of users. In our previous work we proposed a special domain planning algorithm to optimize location privacy supporting potential of certain mobility management mechanisms by increasing the level of concealment of address changes in the network. In this paper we extensively evaluate the scheme by applying well-known location privacy metrics from the literature and using them as objective measures for our original algorithm and its variants first introduced here. The conducted series of simulations verified the efficiency of the scheme and also confirmed the performance enhancements commenced by our improvements and modifications to the original algorithm.**

***Index Terms*—location privacy, privacy metrics, micromobility, simulation, domain planning algorithms, simulated annealing**

I. INTRODUCTION

The Internet is evolving towards a fully pervasive and ubiquitous architecture in which users are expected to be able to use remote resources anytime and anywhere. Besides the evolution of wireless networks toward heterogeneous all-IP mobile communication architectures, end-user terminals are also becoming more and more powerful devices implementing extremely large variety of functions from making voice and video calls through social networking and sharing multimedia till exploiting the advantages of geographic positioning solutions in order to use navigational applications and location based services. However mobile terminals' location data possess important service-enabler potential, in wrong hands it can be used to build up private and intimate profile of the mobile user and can pose serious threats to location privacy [1]. In the all-IP world of future mobile Internet, location privacy of users is even harder to protect as the most common parameters in every single packet – i.e., the source and destination IP addresses – can easily be translated to a quite accurate estimation of the peers' actual geographical location [2][3][4][5][6] thus making third parties able to track mobiles' real-life movements [7][8]. As mobility becomes one of the most unique characteristics of future's convergent architectures, more attention must be given to the above location privacy issues, even at the earliest phases of design: at the network planning level.

When discussing network planning in next generation all-IP heterogeneous wireless communication systems, at least one special factor should be considered. In such systems moving across multiple IP subnets (i.e., changing access nodes which provide IP connection with topologically different address spaces) will occur more likely, resulting in much frequent IP address changes compared to today's mainly homogeneous architectures, therefore raising a strong need of special mobility handling mechanisms. The most known solution for this is called micromobility management which aims to localize mobility events by grouping several IP subnets into domains, and provides fast, seamless, and local handoff control in areas where mobile nodes (MNs) change their point of attachment to the network so often that the general (i.e., macromobility) schemes originate significant overhead in terms of packet delay, packet loss, and excrescent signaling [9]. Frequent IP address changes further aggravate problems of location information leakage. However, micromobility also includes capabilities to support location privacy: localization of mobility events inside a micromobility domain can hide location information easily exposable by IP address changes of handovers [10]. Note that only in cases of inter-domain handovers the location is updated and revealed to outside of the domain; not on each access point change. Next generation, heterogeneous, pico- and femto-cell based mobile architectures [11] are even more sensitive to the above Quality of Service (QoS) and privacy issues which imply the spreading of micromobility protocols (e.g., [12][13][14][15]), and the need of advanced network planning algorithms to support real-life deployment of the micromobilty paradigm.

One of the open issues of deploying micromobility protocols in next generation mobile environments is the optimal design of micromobility domains. The main question is what size (in means of consisting subnets) a micromobility domain should be for reducing the cost of paging, maintaining routing tables and registration signaling. Existing network planning algorithms (e.g., [16][17][18][19][20][21]) are mainly focusing on the trade-off between the paging cost and the registration cost. In our earlier work [22] we considered

* This work is supported by the project TÁMOP-4.2.1/B-09/1/KMR-2010-0002, which is connected to the program of the "Development of quality-oriented and harmonized R+D+I strategy and functional model" at the Budapest University of Technology and Economics.

† Budapest University of Technology and Economics, Department of Telecommunications, Budapest, H-1117, Magyar tudósok körútja 2, Hungary. Corresponding author: László Bokor, E-mail: bokorl@hit.bme.hu

also the location privacy supporting potential of micromobility management and presented a simulated annealing based micromobility domain optimization approach, which – to the best of our knowledge – firstly introduced privacy awareness in network planning methodologies. However, the evaluation of this algorithm was only performed on one specific cell and road structure, and the comparison of simulation results was based on a proprietary quantifier for the location privacy ability of micromobility structures and not on widely and comprehensively accepted location privacy metrics available in the literature. This motivated us to broaden our evaluation efforts and provide an extensive and more complete simulation analysis of the location privacy aware micromobility domain planning scheme and also to use the novel results to further enhance the original algorithm.

The rest of the paper is organized as follows. Section 2 introduces the related work. Preliminaries are summarized in Section 3 by reviewing our prior work – the first delegate of the location privacy aware domain planning scheme called PA-SABLAF – and the definition of the location privacy metrics applied by us for evaluation purposes. Section 4 presents the way how these metrics were realized to be applicable in our scheme, while Section 5 shows the modifications and enhancements of PA-SABLAF eventuated by the applied metrics. The extensive evaluation based on the metrics and the enhanced algorithm versions is detailed in Section 6. Finally, we conclude the paper in Section 7 and sketch the scope of future research.

II. RELATED WORK

It is usually hard to design the size of a micromobility area (i.e., locally administrated domain). Several important questions arise: how to group wireless points of attachments with their relevant coverage into micromobility domains, what kind of principles must be used to configure the hierarchical levels if they are available, and in which hierarchical level is advisable to implement special functions (e.g., anchors or gateways). The traffic load and mobility of nodes may vary, therefore a fixed structure lacks of flexibility: design schemes are needed to comprise these network dynamics and to provide optimal or near-optimal solutions.

An obvious algorithm is to group those access nodes and their coverage areas (i.e., cells) into one domain, which has a high rate of handovers among each other. In that way the number of global location updates (registration messages) can be significantly decreased. But joining too much access nodes into one domain would degrade the overall performance since it will generate a high traffic load on anchor/gateway nodes, and result in higher cost of packet delivery and paging. Contrarily a small number of cells inside a micromobility domain will lead to a huge amount of location updates to the home network but will alleviate paging costs.

Based on these assumptions, He Xiaoning et al. [16] proposed a dynamic micromobility domain construction scheme which is able to dynamically compose each micromobility domain according to the aggregated traffic information of the network.

The related questions are very similar to the Location Area (LA) planning problem (where cells must be grouped into location areas in an optimal way [23][24]), as in micromobility domain planning we also need to search for a trade-off compromise between the location update and the packet delivery cost.

One of the most known LA planning schemes is the solution called Traffic-Based Static Location Area Design – TB-LAD [25], that groups cell pairs with higher inter-cell mobile traffic into the same LA. In this algorithm a list of neighbors is created for each cell, and the neighbor with the highest inter-cell traffic will be selected from the list and included in the same LA with this cell. In the next step the algorithm finds neighbors with the highest traffic from the neighbor lists of the cells that are included for the current LA and includes them into the current LA. This is terminated, when there are no more neighbors that can be included or the maximum number of cells is reached for the current LA. After this loop the algorithm starts the forming of the next LA in the same way.

However, in case of the Location Area Forming Algorithm – LAFA [26], LAs are not formed one after the other, but simultaneously, always including the actual cell-pair to an already existing LA or creating a new one, enabling to build the LA structure in a distributed way.

Based on the experiments of LAFA, the duet of the Greedy LA Forming Algorithm (GREAL) and the Simulated Annealing Based Location Area Forming Algorithm (SABLAF) was proposed by [20]. In this scheme GREAL is adopted to form a basic partition of cells into LAs in a greedy way without any additional assumptions for cell contraction, and then SABLAF is applied for getting the final partition.

Based on this algorithm, authors in [27] constructed a simulated annealing based anycast subnet forming algorithm (SABAS) aiming to use the idea of GREAL+SABLAF for micromobility domain planning. SABAS is a general method for optimal grouping of cells into micromobility domains. Authors show its efficiency by applying the method for a particular micromobility protocol based on IPv6 anycasting.

In [28] authors also propose a similar simulated annealing based LA planning method giving a heuristic and near-optimal solution for LA planning in tolerable run-times.

There is also a specific Location Area planning algorithm for GEO Mobile Satellite Systems: by the way of extensive comparison of the cost of location management using different types of location area designs, an appropriate scheme was separated by the authors satisfying the special requirements of GEO satellite systems [29].

There are also Location Area and micromobility domain planning algorithms which are able to handle network structures with hierarchical levels [18][21] for assignment of an optimal tree structure to a given source of access router handover rates.

However there exists a quite broad literature on location area and micromobility domain planning, the substantial and a-priori question of how to integrate location privacy requirements into the algorithms is still almost completely

unexplored. To the best of our knowledge, the only study about location privacy aware domain planning is our prior research [22], which extends SABLAF/SABAS with a simple location privacy policy model and a special rate weighting technique applied to integrate the effects of the cells' static location privacy significance and mobile nodes' dynamic privacy demands into the boundary crossing rates between neighboring cells. The algorithm is called PA-SABLAF (Privacy Aware SABLAF) and joins the most important cells according to the location privacy policy model which are also in the same dominant moving directions (highways, footpaths, etc.,). Therefore the number of handovers among domains can be decreased while the location privacy is also considered in the created structure. This scheme allows network designers to maximally take into consideration pre-existing location privacy requirements and also the users' dynamic privacy demands in the design phase.

Aiming to provide more general results and to improve the original algorithm of [22], we applied some well-known location privacy metrics from the literature and started the work on more thorough simulation analysis of the location privacy aware micromobility domain planning scheme.

III. PRELIMINARIES

This section reviews our earlier work related to PA-SABLAF together with our originally applied, proprietary metric, then introduces the basics of two, widely accepted and more general metrics from the literature, both are used for evaluating PA-SABLAF in a more universal way and also to enhance our original algorithm.

A. Review of PA-SABLAF and the proprietary metric used for its preliminary evaluation

In the location privacy policy model we applied in [22], a combination of two substances is used to provide boundary conditions for location privacy aware domain planning. On one hand we introduced the *static location privacy significance level of the cells* (denoted by $SLP_{[k]}$ for cell k) which can separate coverage areas inside the operator's network considered to be more sensitive to location privacy than others. On the other hand we defined *user's location privacy profile for different location types* (denoted by $ULP_u^{lt_{[k]}}$ for user u and location type lt of cell k) to describe what level of location privacy protection is required for a mobile user at a given type of location. The incoming dynamic demands are cumulated and the average will be compared with the static location privacy significance level of the issued cell at every announcement. The winner of this comparison – called the *cell's overall location privacy factor* – will take over the role of the cell's static significance level. In this simple way not only operators' requirements, but also the dynamic demands of mobile users can be respected during the location privacy aware network design.

In order to integrate the effects of the cells' overall location privacy factor into the boundary crossing rates between neighboring cells, a special rate weighting technique was created. In the mathematical representation we use, the cells are the nodes of a graph, the cell border crossing directions are represented by the graph edges and the weights are assigned to the edges based on the cell border crossing rates of every direction (i.e., rates of entering or leaving a cell are summarized and assigned to the corresponding edge as its weight). These rates are weighted with the overall location privacy factor of the destination cell.

$$WR_{[k][l]} = CR_{[k][l]} \times OLPF_{[l]} + CR_{[l][k]} \times OLPF_{[k]} \quad (1)$$

where $WR_{[k][l]}$ is the weighted rate of edge between cells (graph nodes) k and l, notation $CR_{[k][l]}$ stands for the cell border crossing rate from cell k to l, and $OLPF_{[l]}$ is the overall location privacy factor of cell l.

Based on the above definition, PA-SABLAF will start with a GREAL-based greedy phase that will provide a basic domain partitioning as an input (i.e., initial solution) of the simulated annealing. At the beginning of this greedy phase, we choose the cell pair with the biggest weighted rate in our cell structure. If the biggest rate occurs multiple times, then we choose one of the instances randomly and include the two cells belonging to that handover rate into domain D_1 of cells. In the next step, we search for the second biggest weighted rate among the cell pairs for which is true, that one of them belongs to domain D_1. We must check whether inequality $N_k < N_{max}$ is satisfied, where N_k is the number of cells in the k^{th} domain and N_{max} stands for the maximum number of cells in a single micromobility domain which will give us the minimum of the registration cost and the maximum size of the location privacy protective micromobility domain. If the inequality is satisfied, the cell can be included into set D_1. If the inequality is not satisfied, the cell can not be included into this set: a new domain with this cell is to be created in order to prevent exceeding the paging cost constraint [22]. In this way we can join the most important cells according to the location privacy policy model which are also in the same dominant moving directions (highways, footpaths, etc.,).

After processing all the cell pairs in the above sequential and greedy way a likely sub-optimal domain structure will be created, which will serve as an input (i.e., initial solution or s_0 domain partitioning) for the simulated annealing part of the algorithm. Based on s_0 a neighbor solution s_1 is then generated as the next solution ($N_k < N_{max}$ must be satisfied by s_1 too), and the change in the registration cost $\Delta C_{Reg}(s_0, s_1)$ is calculated. If a reduction in the cost is achieved, the current solution is replaced by the generated neighbor; otherwise we evaluate the acceptance function $e^{(-\frac{\Delta C_{Reg}}{T})}$ to decide whether to retain or change the current solution (T is the temperature). The cooling schedule is based on three input parameters: initial temperature T, step of decrement ($decr$) for T, and the stopping rule which is the maximal iteration step number until ΔC_{Reg} does not change. The details and the complete flowchart of the whole PA-SABLAF can be found in [22].

In [22] we also performed simulations on PA-SABLAF and showed the potential of our method by comparing it with our

previous domain planning algorithm called SABAS. A proprietary location privacy metric – denoted by $\boldsymbol{LP^{s}_{mic}}$ in this paper – was designed for this purpose to express how efficiently a given micromobility domain structure takes static location privacy significance of cells and the incoming dynamic location privacy demands of users into account during operation (i.e., how effective could be the protection of users' location privacy while keeping paging and registration costs on a bearable level). We quantified the inability of non inside-domain attackers in tracking mobile users by computing a weighted number of inter-domain changes of mobile nodes in the network. This metric tracks and saves movements (i.e., whole paths) of mobile users and also saves cell boundary crossings in order to localize and count mobile nodes' inter-domain changes. For every inter-domain handover of a mobile node and for the previous and the next cells of such handovers the algorithm sums the value of the cells' static location privacy significance and the squared value of the level of the mobile node's location privacy profile set for the issued location types. The above calculation is performed for every mobile node, and the sum of these values will stand for the location privacy metric of the whole micromobility domain system.

$$\boldsymbol{LP^{s}_{mic}} = \\ = \sum_{u} \sum_{h \in IH_u} (ULP_u^{lt_{[k]}})^2 + (ULP_u^{lt_{[l]}})^2 + SLP_{[k]} + SLP_{[l]} \qquad (2)$$

where IH_u means the set of all inter-domain handover events of user u, and $h_{[k][l]} \in IH_u$ stands for a handover event with exit and entry cells of k and l respectively. Implicitly the smaller $\boldsymbol{LP^{s}_{mic}}$ values are the better.

However the above metric is able to numerically present the location privacy capabilities of a complete network's certain micromobility domain structure, it lacks in generality. That is why we started to evaluate our scheme using more general and widespread location privacy metrics. The metrics we have chosen for our efforts are introduced in the next two sections.

B. Uncertainty-based location privacy metric

This type of metric was originally proposed in [30] [31]. Authors in [30] present an information theoretic model that allows to measure the degree of anonymity provided by schemes for anonymous connections. Authors of [31] introduce an information theoretic measure of anonymity that considers the probabilities of users sending and receiving the messages and also show how to calculate this measure for a message in a standard mix-based anonymity system. Both proposals use the same metric model. The attacker's goal is to identify the initiator and/or the responder of a message travelling in the network. Each user in the system is assigned a probability for being the possible initiator/responder of a particular message, and the system's overall anonymity level is determined by the entropy of the random variable that is formed by the users' probabilities. In this way the metric captures the attacker's uncertainty (measured by the entropy) during the identification procedure.

This metric can be easily applied to comply also with location privacy measurement purposes: the location privacy of a given user in the system is calculated as the attacker's uncertainty during linking observed events (e.g., positions in trajectories) to users. Authors in [32] define a well-detailed system model which can be used to formalize the uncertainty-based location privacy metric as follows.

Consider a user $u \in U$ and an event $\hat{e}_i \in \hat{R}_u|_{obs}$ successfully observed by the attacker ($\hat{R}_u|_{obs}$ means all the user u events observed by the attacker). Also consider E^l as the set of edges of the probabilistic graph called the linkability graph (G^l) representing the linkability of observed events based on the attacker's knowledge. (Note, that the attacker's goal is to reassemble the user's actual set of events; hence it assigns probabilities to possible related events in order to reconstruct the user's trajectory.) Define $\pi^l(\hat{e}_i, \hat{e}_j)$ as the weight function of G^l for representing the probability with which the attacker believes that both $\hat{e}_i$ and $\hat{e}_j$ events are associated with the same user and $\hat{e}_i$ is an immediate predecessor of $\hat{e}_j$ in the user's observed set of events. Let a random variable X_i stand for the probability that another observed event $\hat{e}_j$ is the immediate successor of $\hat{e}_i$. According to the notations of [32] we have $Pr_A(X_i = j) = \pi^l(\hat{e}_i, \hat{e}_j)$ for any j such that $(\hat{e}_i, \hat{e}_j) \in E^l$ in G^l, where $Pr_A(s)$ means the probability with which the attacker considers a statement s to be true. The entropy of X_i can be calculated to measure the attacker's uncertainty when linking observed events to users and therefore can be used as objective location privacy metric for user u at the $tm(\hat{e}_i)$ time instance at which the event $\hat{e}_i$ occurred.

$$\boldsymbol{LP^{u}_{u}}\big(tm(\hat{e}_i)\big) = \mathbb{H}(X_i) \\ \mathbb{H}(X_i) = -\sum_{j} Pr_A(X_i = j) \times log_2\big(Pr_A(X_i = j)\big) \qquad (3)$$

Eq. (3) is the common form of the uncertainty-based metric which has been widely used to measure location privacy in different wireless scenarios. For example, authors of [33] applied this scheme in order to maximize the location privacy at each identifier update by users, in the presence of asynchronous identifier updates and predictability of movements of user terminals. In [34] this metric is used to analyze a novel location privacy enhancement protocol which obfuscates several types of privacy-compromising information revealed by mobile nodes, including sender identity, time of transmission, and signal strength. Our last example for application use-cases of the uncertainty-based metric is [35] where authors employ the scheme to measure the performance of their solution designed to enhance users' contradictory requirements on location privacy without diminishing communication QoS.

These examples show how varied application possibilities of the uncertainty-based location privacy metric are and why it is considered a widely accepted and adapted metric in the literature.

C. Traceability-based location privacy metric

This kind of metric captures the level to which the attacker can track a mobile user with high certainty. The attacker's uncertainty or confusion in the tracking procedure is measured by the uncertainty-based metric (e.g., using entropy). In [36] authors define a so called *mean time to confusion* metric to measure the degree of privacy as the time that an attacker could correctly follow a user's trace. Therefore the *mean time to confusion* is the mean tracking time between points where the attacker faced confusion (i.e., was not able to determine the next sample with sufficient certainty). Authors of [37] propose another variant of the traceability-based location privacy metric called the *mean distance to confusion*, which measures the mean distance over which tracking of a user may be possible by the attacker.

The above variants are defined as the time/travel distance until the uncertainty of the tracking grows above a pre-defined threshold. The formalization of the traceability-based location privacy metric is also done according to the system model defined in [32]. We call an event in the observed trace of a user ($\hat{e} \in \hat{R}_u|_{obs}$) as a confusion point if the attacker's uncertainty is above a given threshold: $\boldsymbol{LP}_u^u(tm(\hat{e})) > \mathbb{H}_{cf}$. It means that the *time to confusion / distance to confusion* is specified as the time/distance to travel before reaching a confusion point, during which the attacker's uncertainty remains below $\mathbb{H}_{cf}$. In this way the average value of *time/distance to confusion* represents a user's lack of location privacy.

Denote $\hat{R}_u|_{obs}^{cf}$ as the set of all confusion points (events) of user $u \in U$. Let C_u stand for the union set of the last observed event of user u and the user's confusion events. Let B_u denote the set of events that contain the first observed event from u and all the events which are not confusion points but are immediate successors of each confusion point in the observed trace of user u. Consequently, a traceable period can be defined as the time/travelled distance between an event in B_u and an event in C_u such that there is no other event in B_u in that period. Denote Z_u as the set of all these traceable periods for user u. Based on the above notation the location privacy metric of user u based on *mean time to confusion* ($\boldsymbol{LP}_u^{\dot{t}}$) and *mean distance to confusion* ($\boldsymbol{LP}_u^{\ddot{t}}$) can be defined as the mean tracking time/distance during which uncertainty stays below a confusion threshold and can be calculated as follows (note, that this metric is inversely proportional to *mean time to confusion* and *mean distance to confusion* values).

$$\boldsymbol{LP}_u^{\dot{t}} = \left(\frac{\sum_{(\hat{e}_i, \hat{e}_j \in Z_u)} |tm(\hat{e}_i) - tm(\hat{e}_j)|}{|Z_u|} \right)^{-1} \quad (4)$$

$$\boldsymbol{LP}_u^{\ddot{t}} = \left(\frac{\sum_{(\hat{e}_i, \hat{e}_j \in Z_u)} \|loc(\hat{e}_i) - loc(\hat{e}_j)\|}{|Z_u|} \right)^{-1} \quad (5)$$

where $tm(\hat{e}_i)$ and $loc(\hat{e}_i)$ stands for the time instance and the location at which the event $\hat{e}_i$ occurred, respectively.

This metric is also a well-known and widespread measure of location privacy. One of its main advantages is the fine-grained tuneability: if the threshold of $\mathbb{H}_{cf}$ is chosen high, tracking times increase but so may do the number of false positives (i.e., the attacker follows incorrect traces). A good example for the application of this metric is [38] where authors used the approach in a trace-based simulation of their anonymizer scheme camouflaging users' current location with various predicted paths.

Both the above introduced uncertainty- and traceability-based location privacy metrics are general, widespread and also effective in the means that they are able to quantify the incapacity of a particular attacker in localizing or tracking mobile users. That was our main motivation for choosing them as base approaches in our evaluation work.

IV. REALIZATION AND ADAPTATION OF THE METRICS

Since to the best of our knowledge no other location privacy aware domain planning algorithm exists even in these days, during our preliminary measurements we used our former, simulated annealing based domain optimization method called SABAS [27] as a basis to compare with the PA-SABLAF, and also developed a proprietary location privacy metric in the simulator for this comparison [22]. However, this earlier evaluation work was performed on one cell/road topology only, and the used metric was not general enough for comprehensive analysis. In order to eliminate the above shortcomings we extended the range of topologies/scenarios and adopted two of the most widespread and common location privacy metrics into our simulation environment: uncertainty- and traceability-based location privacy metrics.

A. Metric requirements and assumptions

The level of location privacy in a complete network (i.e., system of several micromobility domains) can be determined by how easily attackers can recognize trajectories (series of cells/access areas owning unique IP prefixes) of mobile users. Every single user in the mobile network passes cells of several domains during their respective paths.

In such architecture inside-domain movements are safe as localized mobility management obfuscates IP address changes of mobile users: valuable addressing information (i.e., location information data of IP communication) will not leak out the domain. However, domain changes will disclose IP address information to all correspondent nodes (CNs) of the mobile as macromobility mechanisms will also be executed besides the micromobility procedures. We assume that the attacker is in continuous communication with the observed mobile user (or at least the attacker is able to capture packets originating from the MN) and is located outside of the MN's domain. The obtainable address information is enough to identify the MN's actual domain but not sufficient to determine the particular cell or access area from where the mobile node communicates.

Due to the aforementioned characteristics of the micromobility management the attacker continuously communicating with the MN can be aware of the complete set of domains crossed during the MN's path, and this information can be used to specify the precise, cell-based

trajectory of the observed entity (i.e., the solution which the attacker wants to obtain). Reconstruction of the whole trajectory gets harder if the built-in location privacy supporting capability of the micromobility domain system (i.e., the obfuscation of the observable information performed by the localized mobility management) becomes more effective. This is what a metric in our framework should measure.

As the attacker can observe only the set of domains the MN passes, it must apply statistical calculations to get the solution. An adequately large domain with sufficient number of inter-domain transitions is able to significantly increase the quantity of potential solutions and to enhance location privacy of users in a general way, independently of pre-defined or dynamic privacy parameters we applied in our earlier work. The metrics below serve as efficient tools in our efforts to enhance PA-SABLAF and create more comprehensive and universal algorithms.

B. Realization and adaptation of LP^u

Aiming to implement the uncertainty-based metric in our simulation framework and to adapt it for our evaluation purposes we slightly modified the $\boldsymbol{LP^u}$ scheme. In order to do this, we adapt the $\boldsymbol{LP^u}$ scheme to our framework and also extend it to be applicable for all the users in the micromobility system (as a sum of their entropies).

In a micromobility network the attacker relying on intercepted IP packets can only observe series of crossed domains along the MN's movements. This is because domains usually contain several cells with multiple possible transitions inside and outside of the particular domain. The exact place of a domain change (i.e., the two cells of that transition) can be determined with probability $\frac{1}{n}$ where n is the number of possible transitions between the two domains.

That is why we calculate $\boldsymbol{LP^u}$ in the following way. We split the trajectory of the MN into domain entry and exit points which are basically the observable events (locations) in our threat model and delimit unobservable path segments between them. As these inside-domain path segments are not traceable based on IP information and assuming that domains contain more than two cells at least, the attacker can only deduce the entry and exit points (so called "flashes"). We assume that transitions are not weighted and the transition probability is the same in every case. Considering $Pr_A(d)$ here as the probability of the attacker guessed right when reckoning the actual entry and exit points of crossing domain d, a user's $\boldsymbol{LP^u}$ for a particular domain inside the network can be produced by calculating the entropy of $Pr_A(d)$. (Note that $Pr_A(d)$ can be computed as the product of the probabilities of inlet- and outlet routes belonging to two consecutive "flashes".) By calculating this entropy for every domain of every user, and creating the sum of these entropies we get the overall entropy of a micromobility system denoted by $\boldsymbol{LP^u_{mic}}$ (as this metric is an entropy-like measure, the larger values denote the better location privacy support).

$$\boldsymbol{LP^u_{mic}} = -\sum_u \sum_j Pr_A(d_j) \times log_2\left(Pr_A(d_j)\right) \tag{6}$$

C. Realization and adaptation of LP^t

Due to the peculiar application scenario devised by our domain planning scheme, modifications in the original concept of the traceability-based metric ($\boldsymbol{LP^t}$) were required. During the realization and adaptation phase of this kind of location privacy measurement approach we recognized that according to our scheme and threat model the attacker is not able to track mobile users when they are moving inside a particular micromobility domain. It means that domains serve as confusion points, which also implies that *mean time to confusion* and *mean distance to confusion* approaches become vague: users spend their time mostly in confusion points and only inter-domain handovers ("flashes") are considered as inter-confusion point events which are negligible both in means of time and distance.

This motivated us to create two slightly modified traceability-based metrics called *mean time in confusion* and *mean distance in confusion*. These two metrics capture the level to which the attacker cannot track a mobile user with high certainty. The mobile user's safety during the IP information-based tracking procedure is measured by our modified $\boldsymbol{LP^t}$ metric versions. We define the *mean time in confusion* metric to measure the degree of privacy as the time that an attacker could not correctly follow a user's trace: the *mean time in confusion* is the mean tracking time between points where the attacker overcomes the confusion (i.e., becomes to be able to determine the next sample with sufficient certainty). Similarly, the *mean distance in confusion* measures the mean distance over which tracking of a user may not be possible by the attacker.

According to the already introduced formalization C_u stands for the union set of the last observed event of user u and the user's confusion events, B_u denotes the set of events that contain the first observed event from u and all the events which are not confusion points but are immediate successors of each confusion point in the observed trace of user u. Consequently, an untraceable period can be defined as the time/travelled distance between two or more consecutive events in C_u such that there is no other event in B_u in that period. Let Y_u stand for the set of all these untraceable periods for user u. Based on the above notation the location privacy metric of user u based on *mean time in confusion* ($\boldsymbol{LP^{\bar{t}}_u}$) and *mean distance in confusion* ($\boldsymbol{LP^{\bar{\bar{t}}}_u}$) can be defined as follows.

$$\boldsymbol{LP^{\bar{t}}_u} = \left(\frac{\sum_{(\hat{e}_i,\hat{e}_j \in Y_u)} \left| tm(\hat{e}_i) - tm(\hat{e}_j) \right|}{|Y_u|}\right)^{-1} \tag{7}$$

$$\boldsymbol{LP^{\bar{\bar{t}}}_u} = \left(\frac{\sum_{(\hat{e}_i,\hat{e}_j \in Y_u)} \left\| loc(\hat{e}_i) - loc(\hat{e}_j) \right\|}{|Y_u|}\right)^{-1} \tag{8}$$

where $tm(\hat{e}_i)$ and $loc(\hat{e}_i)$ stands for the time instance and the location at which the event $\hat{e}_i$ occurred, respectively.

Our simulation framework is not prepared for measuring the time duration between user events (i.e., handovers); the system fits only for marking locations (i.e., cells) and the distance between different locations in means of required transition numbers. Therefore we calculate the overall traceability-based location privacy metric of a micromobility system ($\boldsymbol{LP}^{\bar{\bar{t}}}_{\boldsymbol{mic}}$) in our simulator as follows (the location privacy supporting capability is proportional with the *mean distance in confusion*, so here the exponent implies that the smaller values are the better).

$$\boldsymbol{LP}^{\bar{\bar{t}}}_{\boldsymbol{mic}} = \sum_{u} \left(\frac{\sum_{(\hat{e}_i, \hat{e}_j \in Y_u)} \left\| loc(\hat{e}_i) - loc(\hat{e}_j) \right\|}{|Y_u|} \right)^{-1} \tag{9}$$

V. IMPROVING PA-SABLAF

The above applied metrics introduced more general, extensive and comprehensive aspects into the requirement set of our location privacy aware domain planning scheme, and therefore also eventuated modifications in the original PA-SABLAF algorithm. These modifications formed two novel PA-SABLAF versions, both trying to present more universal and pervasive solutions compared to their predecessor. In this Section these new PA-SABLAF variants are introduced.

A. PA^u-SABLAF

The main design choice for this algorithm was to eliminate the dependency of the operation from both the *static location privacy significance level of the cells* and the *mobile node's location privacy profile* (which equally can narrow the applicability of the model) and create a more general scheme based on the criteria of the widespread and universal uncertainty-based location privacy metric.

In order to do this we altered the greedy phase of the algorithm for increasing the uncertainty of the attacker during its tracking intentions by dismissing the privacy weighted boundary crossing rates ($WR_{[k][l]}$) and creating a novel weighting technique which raises the possible number of transitions at inter-domain movements.

For that reason the greedy phase of PA^u-SABLAF also considers the crossing rates of all the neighboring transitions besides the crossing rates of the actually examined transition. It means that during the contraction the greedy phase favors to choose cell pairs rendering big crossing rates and also showing big traffic through large number of edges between their neighbors. Since the maximum number of cells in a single micromobility domain is limited by N_{max}, we can always create a structure where cells with big transition rates will create domains and simultaneously their neighbors with reasonably significant number and volume of transitions will form neighboring domains such increasing the uncertainty of the attacker observing users' domain changes. According to this, PA^u-SABLAF will lead the traffic of cells with large transit demands away toward as many edges/edge series as possible. The calculation of the weighted rate based on the above considerations and used in the greedy phase of PA^u-SABLAF is as follows.

$$WR^{u}_{[k][l]} = CR_{[k][l]} + CR_{[l][k]} + TF_{[l]} \tag{10}$$

where $CR_{[k][l]}$ stands for the cell border crossing rate from cell k to l, and $TF_{[l]}$ is the transition factor of cell l (a cell still waiting to be grouped into a domain). We defined the transition factor as $TF_{[l]} = \sum_{m \in A_l} (CR_{[l][m]} + CR_{[m][l]})$ where A_l means the set of all neighbors of cell l. Besides this modified weighting and cell selection scheme the PA^u-SABLAF algorithm is the same as the method introduced in Section III/A.

B. PA^t-SABLAF

This algorithm variant also breaks with the rate weighting technique of the original PA-SABLAF and focuses on more general requirements characterized by the traceability-based location privacy metrics. Here the motivation is to create a micromobility domain structure where user traffic is mainly transacted and kept inside the domains. In case of PA^t-SABLAF we also approach this problem by modifying the applied weighting scheme of the greedy phase inside the original algorithm.

The traceability-based metric implies a single domain covering all the access areas (i.e., cells) as the optimal solution for the location privacy aware domain planning problem. Of course this is not an option: N_{max} is the maximum number of cells in a single micromobility domain in order to provide a strict burden for the paging (and such also maximizing the size of the location privacy protective micromobility domain). So we have to take the cost constraints into consideration and simultaneously create a domain structure in which mobile users likely will perform inside-domain movements.

This can be achieved by increasing the number of "deflector" edges inside the domains. We name an edge or a series of edges as "deflector" if it possesses significant crossing rate and/or it provides input and output for high crossing rates of other edges or series of edges from multiple directions. By inserting cell pairs with deflector edges into the micromobility domains we can enforce that frequent cell sequences of mobile users will likely consist a domain. Such a structure decreases inter-domain movements while fulfilling all the domain planning constraints and also enhances the privacy level of the micromobility scheme in an efficient manner. The calculation of the weighted rate based on the above introduced idea framed for the greedy phase of PA^t-SABLAF is as follows.

$$\begin{aligned} &if && E_{[k][l]} \in D_{\psi} \\ &then\ for && \forall E_{[i][j]} \in E_{[k][l]} \cup A_{[k][l]} \\ &do && WR^{t}_{[i][j]} = CR_{[i][j]} + CR_{[i][j]} + DF \end{aligned} \tag{11}$$

where $E_{[k][l]}$ denotes the edge between cells k and l, D_{ψ} means the set of deflector edges containing edges with the upper ψ percent of all crossing rates in the network, $A_{[k][l]}$ is

the set of neighbors of $E_{[k][l]}$, $CR_{[k][l]}$ stands for the cell border crossing rate from cell k to l, and DF is a constant called deflector factor used for rewarding certain edges with deflector properties. This basically means that deflector edges chosen with parameter ψ and their neighboring edges are rewarded with parameter DF.

Besides the special weighting technique of (11) the PA^t-SABLAF algorithm is basically identical to our original scheme.

VI. Evaluation results

We have evaluated our location privacy aware micromobility domain planning methods (PA-SABLAF, PA^u-SABLAF and PA^t-SABLAF) in four different scenarios formed by complex network architectures consisting of several cells, mobile nodes and various compound road grids (Fig. 2). Using this environment we compared our algorithms with their ancestor – the already introduced SABAS [27], which is also a simulated annealing based micromobility domain forming solution but without any trace of location privacy awareness.

A. Simulation framework

In order to evaluate PA-SABLAF together with its variants and analyze their performance in real-life scenarios, we designed and implemented a realistic, Java-based mobile environment simulator, which serves a two-fold purpose.

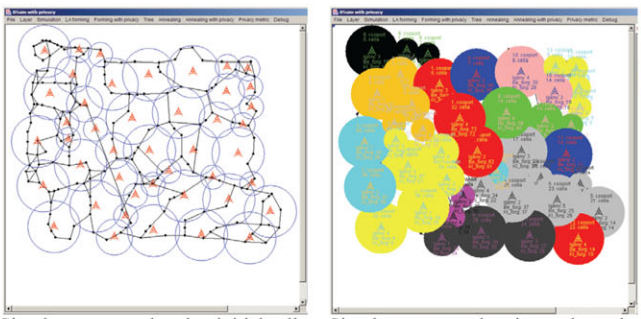

Simulator screen showing initial cell and road structure built in the GUI

Simulator screen showing a planned micromobility domain structure

Fig. 1. The simulation software in use

On one hand it generates a realistic cell boundary crossing and incoming call (i.e., initiation of IP session) database in a mobile system given by the user with cell, mobile node and movement path placing within the GUI. It also calculates both the handover rate and the location privacy-weighted rate for each cell pair, defined on the border of these cells. The incoming session statistic can be also generated for every cell; therefore the paging cost and the registration cost can be calculated in the same time for every domain.

On the other hand the simulator uses the above produced data as an input for the widest scale of location area and domain planning algorithms, and forms LAs and micromobility domains by running the implemented mathematical functions.

The simulation can be executed on an arbitrary and customizable road grid covered by cells of various access technologies (e.g., WiFi, GSM, UMTS) as shown in Fig. 1 (left). The static location privacy significance level of the cells can also be set in case of need as well as the location type. Mobile nodes (MN) can be placed into this highly customizable environment by firstly specifying MNs' velocities, setting the incoming session arrival parameter (IP session intensity) and the location privacy profile to every mobile node if needed.

This way different types of mobility environments with different location privacy characteristics can be designed (rural environment with highways without strict location privacy requirements or a densely populated urban environment with roads and carriageways and the widest scale of location privacy sensitive areas like military facilities, government buildings, etc.,), together with the grids of cells configured and adapted to these environments. The applied mobility model here for MNs is the following. The different mobile terminals will move on the defined road grid by time-to-time choosing a random destination point on the road, similarly as in real life. Since typical mobile users are on the move aiming to manage a specific duty or reach a particular destination (e.g., heading to a hotel, a workplace, a hospital, etc.,) and they usually want to arrive in the shortest possible time, therefore the Dijkstra algorithm is used in our simulation framework in order to find the shortest path for mobile hosts towards their selected destination. The average speed of MN movements is defined by the velocity parameter of each mobile node.

For every mobile node an incoming session arrival parameter is defined and when a session initiation packet hits the node, the simulator designates it to the cell where the node is in that moment. When a mobile host changes a cell, the simulator registers that a handover (i.e., cell boundary crossing) happened between the respective cell-pair. When a simulation run ends, the simulator sums the cell boundary crossings and incoming session initiation distribution for every cell in the simulated network, and also calculates the normal and the location privacy-weighted rates for the LA and micromobility domain planning algorithms. The results (road structure, cell structure, call numbers and cell matrix, mobile data) can be saved and opened to easily provide inputs for the Java implementation of our algorithms. An example domain structure gathered at the end of the whole simulation process is depicted in Fig. 1 (right).

Our goal with this mobility simulator was to provide a flexible tool which is able to give the possibility to evaluate LA partitioning and micromobility domain planning algorithms for the widest scale of network types, by freely choosing the road grid, communicating mobile hosts and cell structure/characteristics.

B. Parameters and scenarios

The comparison was carried out with the help of two key performance indicators. On one hand we analyzed the schemes using the applicable privacy metrics ($\boldsymbol{LP^s_{mic}}$, $\boldsymbol{LP^u_{mic}}$, and $\boldsymbol{LP^{\bar{i}}_{mic}}$, respectively) from the location privacy point of view. On the other hand we used the global registration cost to

measure the efficiency of the algorithms from the signaling cost optimization perspective. Note, that besides the above we also considered the N_{max} as a constraint for the paging costs.

In order to provide an extensive and broad simulation analysis of the location privacy aware micromobility domain planning scheme represented by the three algorithm versions, we executed several simulation runs for all the three algorithm variants, for $N_{max} = [2..6]$ values, for every scenario, and depicted the total average of all the measurements for a particular domain planning solution in function of the N_{max}. Besides this, in case of the third variant (i.e., PA^t-SABLAF) we applied different ψ and DF value combinations ($\psi = 20\%, DF = 20$, $\psi = 40\%, DF = 15$, $\psi = 60\%, DF = 10$), and showed the average of these results in our analysis.

Four different scenarios were defined and created in our simulation framework by cell (i.e., wireless internet point of access), mobile node and movement path placing. These scenarios were designed to differ in their cell/access point structures, number of active mobile users, and style of interconnection (i.e., possible transition paths between cells) aiming to provide a reasonable scale and variety of initial input data for evaluation. Fig. 2 depicts these scenarios and the following enumeration details the most important scenario parameters and characteristics.

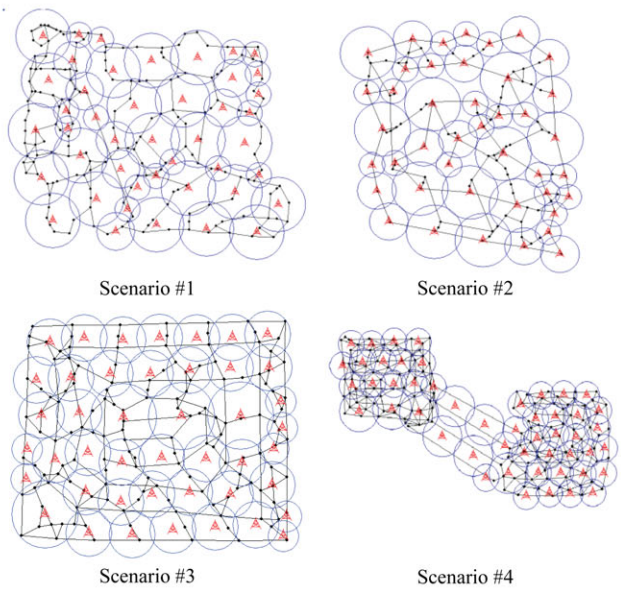

Fig. 2. Simulation scenarios used for evaluation

1) *Scenario #1* consists of 44 multiply interconnected cells and 33 mobile users. Both densely linked (urban-like) and rarely linked (rural-like) areas exist in this construction.
2) *Scenario #2* consists of 42 multiply interconnected cells and 33 mobile users. The average level of interconnection of cells is significantly lower than in Scenario #2, implicating smaller number of transition possibilities.
3) *Scenario #3* consists of 44 multiply interconnected cells and 25 mobile users. This scenario represents a structure where the possible number of inter-cell transitions is high.
4) *Scenario #4* consists of 50 multiply interconnected cells and 22 mobile users. This structure has two, densely linked cell groups, which is interconnected with only a limited set of cells and transition paths.

The simulation of the four scenarios was run till the completion of several thousands of handovers in order to generate substantial number of realistic cell boundary crossings, incoming call/session data and location privacy-weighted rates for each cell pair, also calculating the paging cost and the registration cost for every domain. The produced data will then be used as an input for our algorithms to be evaluated.

C. Results

As an initialization of our experiments we ran the mobility simulator on the scenarios of Fig. 2 and gathered all the required input data for our three location aware domain planning solutions (PA-SABLAF, PA^u-SABLAF, PA^t-SABLAF) and for the base algorithm of our evaluation (SABAS). After that we executed all the algorithms (with parameters $N_{max} = 6$, $T = 100$, and $decr = 2$) on the produced input data and cell structure in order to render the micromobility domain configuration.

On the rendered domain layout we examined how the registration cost and the location privacy metric changes by increasing the maximum number of cells in one micromobility domain for each algorithm and scenario. This way we could check how the domain forming methods perform in terms of location privacy support and signaling cost optimization, and also whether the registration cost function is correct (i.e., whether it reaches the minimum value when a domain consists N_{max} number of cells.)

Simulation results depicted on Fig. 3 and 4 show that PA-SABLAF finds a much better domain structure in means of the $\boldsymbol{LP^s_{mic}}$ metric for every value of N_{max} compared to the original SABLAF. However, we have to pay the prize of this benefit: the registration cost is slightly higher in most of the cases with a maximum of 4.8%. We have to emphasize, that the $N_{max} = 6$ case results in gain also regarding the registration cost, so here the algorithm managed to ameliorate both parameters of the trade-off.

Fig. 5 and 6 introduces that PA^u-SABLAF achieves the most significant relative gain in means of the location privacy metric and the registration cost increment: a more then 30% relative growth can be noticed for location privacy in the $N_{max} = 6$ case. Despite this promising result PA^u-SABLAF shows the most serious volume of additional registration costs after location privacy aware domain planning: even the smallest cost growth is 27%. However, this is compensated by the remarkable revenues of the $\boldsymbol{LP^u_{mic}}$ metric.

Results of PA^t-SABLAF evaluation is depicted in Fig. 7 and 8. This algorithm variant performs a moderate average gain (3.9%) in our scenarios and also shows negative relative gain in the $N_{max} = 4$ case. However, the algorithm enhances the privacy metric together with registration cost in all the other N_{max} cases which is not a negligible achievement.

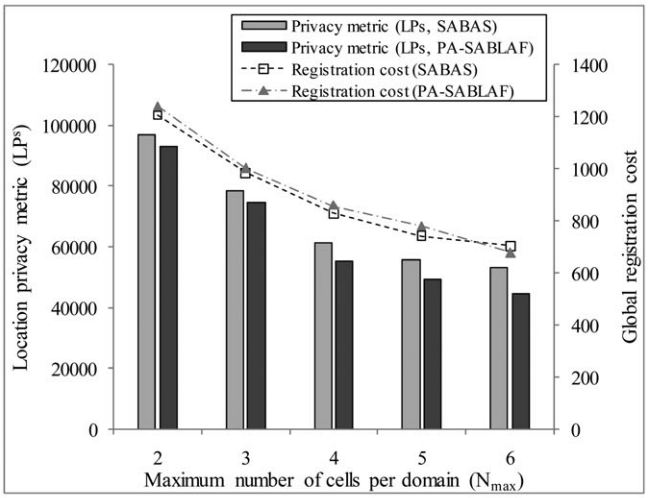

Fig. 3. PA-SABLAF vs. SABAS

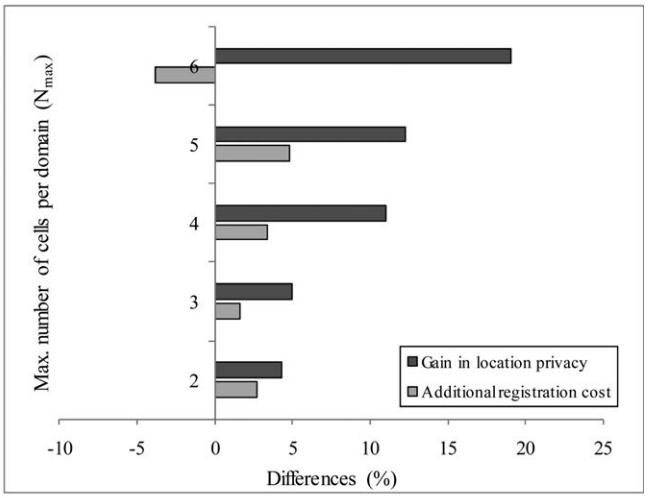

Fig. 4. Location privacy gain vs. cost increment: PA-SABLAF

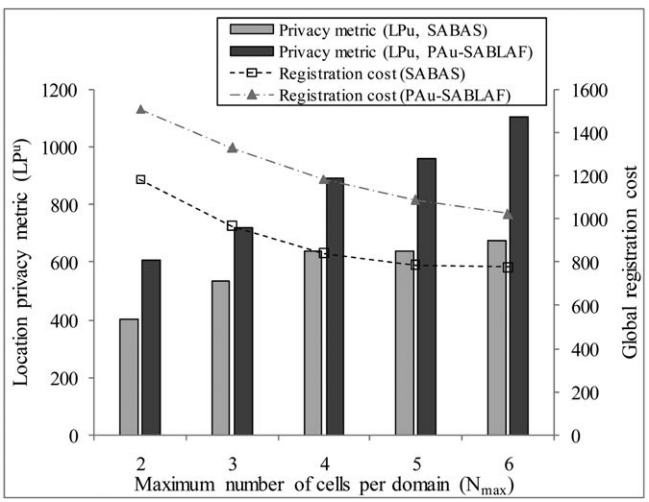

Fig. 5. PA^{u}-SABLAF vs. SABAS

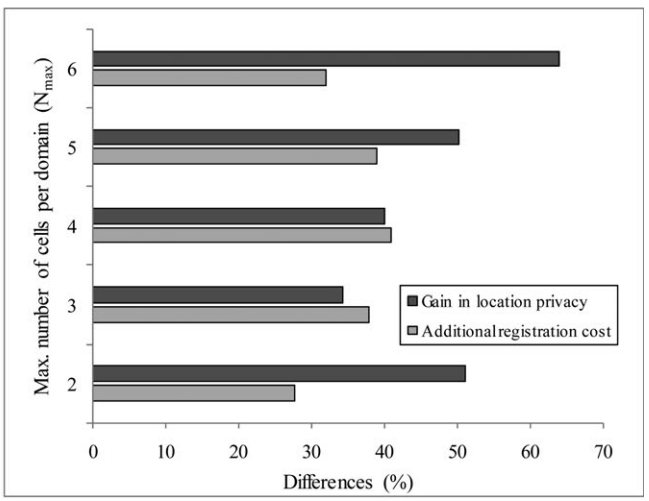

Fig. 6. Location privacy gain vs. cost increment: PA^{u}-SABLAF

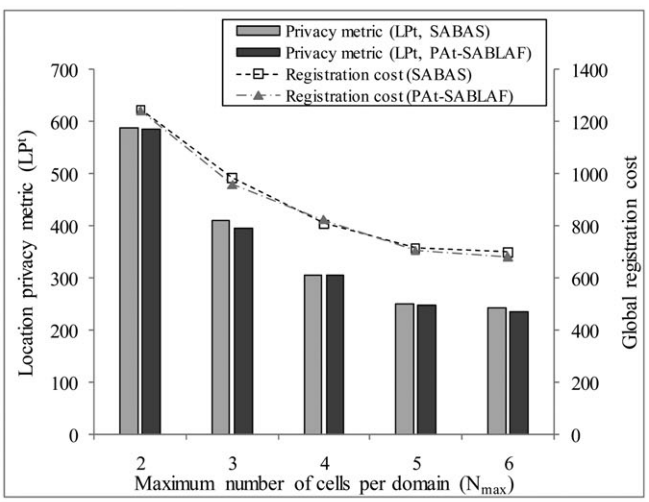

Fig. 7. PA^{t}-SABLAF vs. SABAS

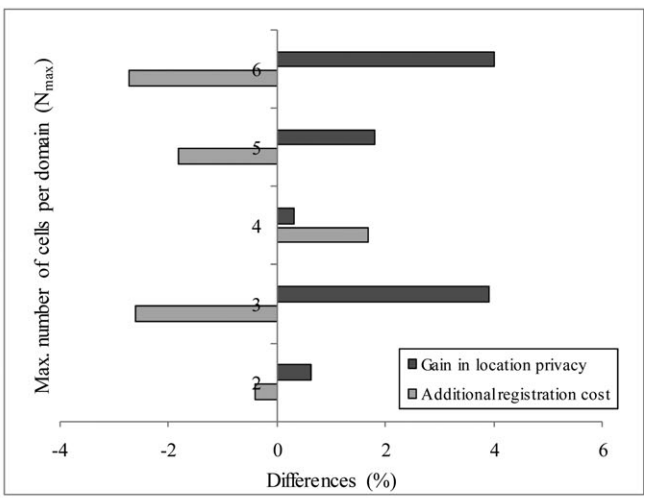

Fig. 8. Location privacy gain vs. cost increment: PA^{t}-SABLAF

VII. CONCLUSION

In order to create a mobile network architecture which provides location privacy for mobile users in micromobility environments by exploiting inherent properties of micromobility protocols, optimized domain planning is needed that also considers the strict constraints formed by paging and registration costs. This paper evaluates the location privacy aware micromobility domain planning scheme. The scheme is represented here by three algorithm variants (PA-SABLAF, PA^u-SABLAF and PA^t-SABLAF, the last two first presented in this paper), both of them based on a two-step domain forming solution, which consists of a greedy phase that gives the basic cell partitions, and a simulated annealing phase which gives a near-optimal domain structure in acceptable runtime. The algorithms differ in the operation of their greedy schemes, respectively optimized for a particular attribute of location privacy.

Aiming to evaluate the performance of the scheme, a mobile environment simulator was used and three different quantifiers for the location privacy ability of micromobility structures were applied ($\boldsymbol{LP^s_{mic}}$, $\boldsymbol{LP^u_{mic}}$, $\boldsymbol{LP^{\bar{t}}_{mic}}$, the first being a proprietary metric from the earlier work of the authors, and the last two being adaptations of well-known and widespread measures of location privacy from the literature). Using the input data produced by a realistic simulation environment, the micromobility domain planning methods could be evaluated. Based on this comprehensive toolset we evaluated our location privacy aware algorithms by examining the global registration cost and the location privacy metric of the network in the function of the maximal number of cells per a micromobility domain. As a result of our evaluation efforts we can say that the scheme proved its power by significantly enhancing the location privacy of users in the network. The total average gain in location privacy for every run of all the three algorithm variants approached 20% at the expense only of a total average 8% growth of the global registration cost (meaning an average 12% relative gain), and there were also distinct cases when the scheme operated with more than 30% relative gain.

As the main part of our future work we plan to integrate our algorithms. It is obvious that PA^u-SABLAF and PA^t-SABLAF catch conflicting attributes of location privacy. In order to provide a more general and complete scheme, it is advisable to combine their features and integrate them in a complex solution. Even merging all three proposed algorithms could be efficient and achievable. We also plan to integrate the concept of location privacy aware network planning into researches relating to personal paging area design.

ACKNOWLEDGMENT

This study was supported by Mobile Innovation Centre Hungary. The authors also would like to express their appreciation to Krisztián Kovács for his essential work on this research and also to Gábor Gulyás and Iván Székely for raising interest in location privacy studies.

REFERENCES

[1] A.R. Beresford and F. Stajano, "Location privacy in pervasive computing," *IEEE Pervasive Computing*, pp. 46–55, 2003.

[2] A. Lakhina, J. Byers, M. Crovella, and I. Matta, "On the Geographic Location of Internet," *IEEE Journal on Selected Areas in Communications*, August 2003.

[3] Michael J. Freedman, Mythili Vutukuru, Nick Feamster, and Hari Balakrishnan, "Geographic Locality of IP Prefixes," in *Internet Measurement Conference (IMC)*, Berkeley, CA, 2005.

[4] B. Gueye, A. Ziviani, M. Crovella, and S. Fdida, "Constraint-based geolocation of internet hosts," *IEEE/ACM Transactions on Networking*, vol. 14, no. 6, pp. 1219-1232, December 2006.

[5] Brian Eriksson, Paul Barford, Joel Sommersy, and Robert Nowak, "A Learning-based Approach for IP Geolocation," in *Lecture Notes in Computer Science*. Berlin / Heidelberg: Springer, 2010, vol. 6032/2010, pp. 171-180.

[6] Y. Wang, D. Burgener, M. Flores, A. Kuzmanovic, and C. Huang, "Towards Street-Level Client-Independent IP Geolocation," in *Proc. USENIX Symposium on Networked Systems Design and Implementation (NSDI'11)*, Boston, MA, 2011.

[7] W. Haddad et al., Anonymous Identifiers (ALIEN): Privacy Threat Model for Mobile and Multi-Homed Nodes, June 26, 2006.

[8] R. Koodli, IP Address Location Privacy and Mobile IPv6: Problem Statement, May 2007.

[9] P. Reinbold and O. Bonaventure, "IP Micro-Mobility Protocols," *IEEE Communications Surveys & Tutorials*, pp. 40-57, 2003.

[10] Jukka Ylitalo, Jan Melen, Pekka Nikander, and Vesa Torvinen, "Re-thinking Security in IP based Micro-Mobility," in *Proc. of the 7th International Conference on Information Security Conference (ISC'04)*, Palo Alto, CA, USA, 2004, pp. 318-329.

[11] FemtoForum. (2010, June) Femtocells – Natural Solution for Offload – a Femto Forum brief.

[12] A. Valko, "Cellular IP: A New Approach to Internet Host Mobility," *ACM SIGCOMM Comp. Commun. Rev.*, vol. 29, no. 1, pp. 50-65, January 1999.

[13] H. Soliman, C. Castelluccia, K. El Malki, and L. Bellier, Hierarchical Mobile IPv6 Mobility Management (HMIPv6), August 2005.

[14] L. Bokor, Sz. Nováczki, and S. Imre, "A Complete HIP based Framework for Secure Micromobility," in *5th @WAS International Conference on Advances in Mobile Computing and Multimedia*, Jakarta, Indonesia, 2007, pp. 111-122.

[15] A. A.-G. Helmy, M. Jaseemuddin, and G. Bhaskara, "Multicast-based mobility: a novel architecture for efficient micromobility," *IEEE Journal on Selected Areas in Communications*, vol. 22, no. 4, May 2004.

[16] Xiaoning He, Daichi Funato, and Toshiro Kawahara, "A dynamic micromobility domain construction scheme," in *Personal, Indoor and Mobile Radio Communications (PIMRC'03)*, vol. 3, 2003, pp. 2495 - 2499.

[17] P. S. Bhattacharjee, D. Saha, and A. Mukherjee, "Heuristics for assignment of cells to switches in a PCSN," in *Proc. IEEE Int. Conf. Personal Comm.*, Jaipur, India, 1999, pp. 331-334.

[18] S. Pack, M. Nam, and Y. Choi, "A Study On Optimal Hierarchy in Multi-Level Hierarchical Mobile IPv6 Networks," in *IEEE Globecom*, 2004, pp. 1290-1294.

[19] Shi-Wu Loa, Tei-Wei Kuo, Kam-Yiu Lam, and Guo-Hui Lic, "Efficient location area planning for cellular networks with hierarchical location databases," *Computer Networks*, vol. 45, no. 6, pp. 715-730, August 2004.

[20] V. Simon and S. Imre, "A Simulated Annealing Based Location Area Optimization in Next Generation Mobile Networks," *Journal of Mobile Information Systems*, vol. 3, no. 3/4, pp. 221-232, 2007.

[21] V. Simon, L. Bokor, and S. Imre, "A Hierarchical Network Design Solution for Mobile IPv6," *Journal of Mobile Multimedia (JMM)*, vol. 5, no. 4, pp. 317-332, 2009.

[22] L. Bokor, V. Simon, and S. Imre, "A Location Privacy Aware Network Planning Algorithm for Micromobility Protocols," in *Simulated Annealing, Theory with Applications*.: Sciyo, 2010, pp. 75-98.

[23] J.G. Markoulidakis, G.L. Lyberopoulos, D.F. Tsirkas, and E.D. Sykas, "Evaluation of location area planning scenarios in future mobile telecommunication systems," *Wireless Networks*, vol. 1, pp. 17 - 29, 1995.

[24] S. Tabbane, "Location Management Methods for Third Generation Mobile Systems," *IEEE Commun. Mag.*, vol. 35, no. 8, 1997.

[25] E. Cayirci and I.F. Akyildiz, "Optimal Location Area Design to Minimize Registration Signalling Traffic in Wireless Systems," *IEEE Transactions on Mobile Computing*, vol. 2, no. 1, 2003.

[26] V. Simon and S. Imre, "Location Area Design Algorithms for Minimizing Signalling Costs in Mobile Networks," in *Mobile Computing: Concepts, Methodologies, Tools, and Applications*, David Taniar, Ed., 2009, pp. 682-695.

[27] László Bokor, Vilmos Simon, István Dudás, and Sándor Imre, "Anycast Subnet Optimization for Efficient IPv6 Mobility Management," in *IEEE GIIS'07*, Marrakesh, 2007, pp. 187-190.

[28] N. B. Prajapati, R. R. Agravat, and M. I. Hasan, "Simulated Annealing for Location Area Planning in Cellular networks," *International journal on applications of graph theory in wireless ad hoc networks and sensor networks (GRAPH-HOC)*, pp. 1-7, March 2010.

[29] Gao Qian, Li Guang-xia, Lv Jing, Xu Yi-qun, and Zhou Ming, "Location Area Design for GEO Mobile Satellite System," in *Second International Conference on Computer Engineering and Applications (ICCEA)*, Bali Island, Indonesia, 2010, pp. 525 - 529.

[30] Claudia Diaz, Stefaan Seys, Joris Claessens, and and Bart Preneel, "Towards measuring anonymity," in *PET'02*, San Francisco, 2002.

[31] Andrei Serjantov and George Danezis, "Towards an Information Theoretic Metric for Anonymity," in *Privacy Enhancing Technologies*. Berlin / Heidelberg: Springer, 2003, vol. 2482/2003, pp. 259-263.

[32] Reza Shokri, Julien Freudiger, Murtuza Jadliwala, and Jean-Pierre Hubaux, "A Distortion-Based Metric for Location Privacy," in *8th ACM workshop on Privacy in the electronic society*, Chicago, Illinois, USA , 2009, pp. 21-30.

[33] Li Mingyan, Sampigethaya Krishna, Huang Leping, and Poovendran Radha, "Swing & swap: user-centric approaches towards maximizing location privacy," in *Proceedings of the 5th ACM workshop on Privacy in electronic society (WPES '06)*, Alexandria, VA, USA., 2006.

[34] Jiang Tao, J., Wang Helen, and Hu Yih-Chun, "Preserving Location Privacy in Wireless LANs," in *ACM MobiSys'07*, vol. Proceedings of the 5th international conference on Mobile systems, applications and services, San Juan, Puerto Rico, USA., 2007.

[35] Huang Leping, Yamane Hiroshi, Matsuura Kanta, and Sezaki Kaoru, "Silent Cascade: Enhancing Location Privacy Without Communication QoS Degradation," in *Security in pervasive computing*, J.A. Clark et al., Ed. Berlin Heidelberg: Springer-Verlag, 2006, vol. Lecture Notes in Computer Science 3934/2006, pp. 165-180.

[36] Hoh Baik, Gruteser Marco, Xiong Hui, and Alrabady Ansaf, "Preserving privacy in gps traces via uncertainty-aware path cloaking," in *Proceedings of the 14th ACM conference on Computer and communications security (ACM CCS '07)*, Alexandria, Virginia, USA., 2007.

[37] Hoh Baik et al., "Virtual trip lines for distributed privacy-preserving traffic monitoring," in *Proceeding of the 6th international conference on Mobile systems, applications, and services (ACM MobiSys '08)*, Breckenridge, Colorado, USA., 2008, pp. 15-28.

[38] T., Meyerowitz Joseph and Roy, Choudhury Romit, "Realtime location privacy via mobility prediction: creating confusion at crossroads," in *Proceedings of the 10th workshop on Mobile Computing Systems and Applications (ACM HotMobile '09)*, Santa Cruz, CA, USA, 2009.

László Bokor graduated in 2004 with M.Sc. degree in computer engineering from the Budapest University of Technology and Economics (BME) at the Department of Telecommunications. In 2006 he got an M.Sc.+ degree in bank informatics from the same university's Faculty of Economic and Social Sciences. He is a Ph.D. candidate at BME, member of the IEEE, member of Multimedia Networks Laboratory and Mobile Innovation Centre of BME where he participates in researches of wireless protocols and works on advanced mobility management related projects (as FP6-IST PHOENIX and ANEMONE, EUREKA-Celtic BOSS, FP7-ICT OPTIMIX, EURESCOM P1857, EUREKA-Celtic MEVICO). His research interests include IPv6 mobility, next generation networks, mobile broadband networking architectures, network performance analyzing, and heterogeneous networks.

Vilmos Simon received his Ph.D. from Budapest University of Technology and Economics (BUTE) in 2009 and is currently a senior lecturer at the Department of Telecommunications. His research interests include self-organizing and adaptive networks, evolution of communication protocols, opportunistic and delay-tolerant networks, mobility management and energy efficiency in 3G and 4G mobile systems. He participated in several research projects including the EU ICST-FET FP6 BIONETS where he also acted as a WP leader. He published 30+ papers in international journals and conferences, and acts as a reviewer or organizer for numerous scientific conferences.

Sándor Imre was born in Budapest in 1969. He received the M.Sc. degree in Electronic Engineering from the Budapest University of Technology (BME) in 1993. Next he started his Ph. D. studies at BME and obtained dr. univ. degree in 1996, Ph.D. degree in 1999 and DSc degree in 2007. Currently he is carrying his teaching activities as Head of the Dept. of Telecommunications of BME. He was invited to join the Mobile Innovation Centre of BME as R&D director in 2005. His research interest includes mobile and wireless systems, quantum computing and communications. Especially he has contributions on different wireless access technologies, mobility protocols and reconfigurable systems.

Energy and Frequency Analysis of Wireless Smart Metering Solutions

Gergely Ill, Károly Lendvai, *Member, IEEE*, Ákos Milánkovich, *Member, IEEE*,
Sándor Imre, *Member IEEE, HTE*, Sándor Szabó, *Member IEEE, HTE*

Abstract: **The aim of this paper is to provide a brief summary and analysis of today's state-of-the-art wireless smart metering solutions. The most important factors to evaluate wireless protocols are presented in order to form basics of further research. Furthermore a mathematical approach was constructed which determines numerically the efficiency of the evaluated systems. Using the created formulas, the efficiency of different smart metering solutions was calculated in bit/Joule. Also measurements were conducted to determine the available range using different frequencies.**

1. INTRODUCTION

Nowadays one of the very important areas in research and development is smart metering. More and more countries are introducing their own solutions for the task, as automated reading of data offers tremendous advantages over the conventional methods. European Union directives are motivating further research.

Possible application areas of the system: metering of gas, electricity, water etc. consumption in a remote and scalable way. The technology should be operable in villages, sparsely populated areas and also in blocks of flats in cities. These special criteria challenge device vendors because of the entirely different goals and needs.

The paper is structured as follows: Section 2 introduces smart metering advantages over traditional metering. Section 3 summarizes the available solutions suitable for wireless smart metering.

Section 4 compares the selected solutions based on a set of features. Section 5 introduces a novel calculation of protocol efficiency and compares the solutions according to the results. Section 6 presents the frequency versus range measurement conducted during the research. The last section concludes the paper.

Manuscript received August 31, 2011. This work is connected to the scientific program of the "Development of quality-oriented and harmonized R+D+I strategy and functional model at BME" project, supported by the New Hungary Development Plan (Project ID: TÁMOP-4.2.1/B-09/1/KMR-2010-0002).

G. Ill and Á. Milánkovich are students at the Department of Telecommunications, Budapest University of Technology and Economics, Budapest, 2, Magyar tudósok körútja, 1117, Hungary (e-mail: gill@bme-infokom.hu).

K. Lendvai, S. Szabó and S. Imre are with the Department of Telecommunications, Budapest University of Technology and Economics, Budapest, 2, Magyar tudósok körútja, 1117, Hungary, e-mail: lendvai@hit.bme.hu).

2. SMART METERING

Smart metering technology is supposed to substitute the traditional meters, practically by digitalizing them. Today's analogue meters can only measure the total consumption of a billing unit, which means there is no information about the exact values between two readings. In contrast, smart meters are able to determine e.g. the hourly consumption and identify differences between the different periods of a day, and present these data to the provider and consumer. This technology provides not only digital reading of meters but much more, for instance alerting functions. Smart metering devices can form a wireless network which collects and forwards every single device's measured data to a central unit for processing. With the help of smart meters the end users can monitor their current consumption (water, gas, electricity and also providers can obtain continuous information about their users' consumption customs.

Advantages for the provider are as follows:

- more accurate knowledge of the time distribution of measured data
- decrease of administrative costs
- monitoring of leaks continuously
- more opportunities for retail service renewal

Advantages for the consumer:

- no payment for meter reading and billing
- quick detection anomalies (broken pipes, gas leaks, etc.)
- consumption can be monitored real-time
- current balance can be monitored

According to Berg Insight's newest research, the number of households using smart meters will reach 130 million in Europe by 2015, and 116.5 million is Asia, Australia and the Pacific summed [1].

3. AVAILABLE SOLUTIONS

There are many wired and wireless solutions available, but this article focuses only on wireless technologies.

The following solutions passed our selection criteria:

DASH7 is a wireless sensor network technology based on active RFID standards (ISO/IEC 18000-7). The operating frequency is 433 MHz, which is in one of the ISM bands and can be used worldwide. The technology was originally developed for military use (supported by US Department of Defense), but it is penetrating to consumer markets as well.

The standard is being pushed by the DASH7 Alliance, a non-profit industrial syndicate existing since March 2009. OpenTag is an open source implementation in C language [2].

ZigBee is a specification for a suite of high level communication protocols using small, low-power digital radios based on the IEEE 802.15.4 standard for Low-Rate Wireless Personal Area Networks (LR-WPANs), such as wireless light switches with lamps, electrical meters with in-home-displays, consumer electronics equipment via short-range radio that need low data rates. The technology defined by the ZigBee specification is intended to be simpler and less expensive than other WPANs, such as Bluetooth. ZigBee is targeted at radio frequency (RF) applications that require a low data rate, long battery life and secure networking [3], [4], [5].

ONE-NET provides the open design specification necessary to enable a low-cost, low-bandwidth wireless control network. Residential applications need control/automation devices to be low cost, very low power (able to run on batteries), and able to operate in secure wireless communication modes. For the greatest market penetration, these devices must be interoperable, using open design standards. The protocol is small and simple enough to run on a wide variety of low cost microcontrollers [6].

SimpliciTI is a free network protocol stack developed by Texas Instruments. It provides a simple API for communication between radio devices. The protocol is fully supported by the company's devices and they provide sample codes and tutorials. SimpliciTI is suitable for smart metering applications. TI's major design principle was efficient energy use, which makes their devices consume less power [7], [8].

Wavenis Wireless Technology is a wireless connectivity platform dedicated to serve machine-to-machine (M2M) applications. The main requirements in today's data-centric M2M industry are quite different from broadband and high-speed Internet connections, and generally focus on providing ways to transmit small amounts of data wirelessly on a regular but non-permanent basis. Coronis Systems created Wavenis as a proprietary technology in 2001. It was decided to form an open standard based on this technology in 2008. The Wavenis Open Standard Alliance created Wavenis-OSA to manage and govern the technology to evolve [9].

The following technologies were also considered:

Bluetooth is a well-known standard, which has a very limited range and higher energy consumption [10].

Z-Wave is not open source therefore it is not publicly documented. Open-zwave is not ready yet [11].

6LoWPAN is an acronym of IPv6 over Low power Wireless Personal Area Networks. 6LoWPAN is the name of a working group in the Internet area of the IETF. This protocol is not a finished standard yet [12].

DLMS/COSEM: Device Language Message Specification is an abstract modeling tool for communication entities. COmpanion Specification for Energy Metering is a set of rules, based on existing standards, for data exchange with energy meters. Because it covers only the OSI application layer to transport layer, it was not included in this paper [13].

Figure 1 shows a summarized view of the selected solutions and what they implement from the ISO/OSI layer hierarchy.

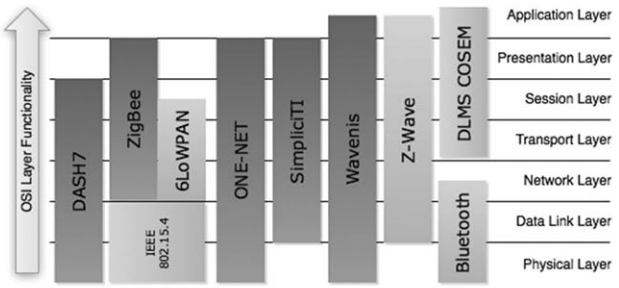

Figure 1 - Investigated technologies and the ISO/OSI layers they cover

4. ANALYZED PARAMETERS

In this section, a uniform system of categorized features is presented to provide a detailed classification of selected solutions.

Features compared are:

Frequency band [MHz]: depending on the frequency used the waves can propagate through water, concrete, urban obstructions with different loss and reflection. E.g. DASH7 uses ISM-band at 433 MHz, in which signals penetrate through concrete constructions, and the frequency is free to use in many countries without much interference. Experiments were also conducted on 868 MHz and found out that 433 MHz has better penetration capabilities and longer range at the expense of lower bit rate. All solutions use ISM frequency bands.

Range [m] means how far two meters can transmit and receive information reliably. DASH7's 433 MHz is applicable for up to 2 kilometers of transmission range outside and about 3 floors indoors with a standard antenna and batteries and regulated transmit power (10 mW in EU).

Measurements were conducted to compare the range of 433 MHz and 868 MHz frequencies. The results are presented in the Section 5.

Table 1 shows a comparison of the investigated systems according to the different features. The Λ parameter in the last row is defined in the following sections.

Feature	DASH7	ZigBee	ONE-NET	SimpliciTI	Wavenis
International standard?	ISO/IEC 18000-7	IEEE 802.15.4	-	-	-
Frequency band [MHz]	433.92	868/915 /2400 (Pro)	US: 915 EU: 866.5	480/868/ 915/955/ 2400	868 (EU) 915 (US) 433 (extension) 2400 (optional)
Indoor range [m]	20-50	10-70	60-100	10-60	200
Outdoor range [m]	1500	1500	500	1739.5 at 433 MHz 825.1 at 915 MHz 314.5 at 2.45 GHz	LOS range up to 1 km 25 mW; LOS range up to 4 km 500 mW
Transmission speed [kbps]	200	20/40/250	38.4-230.4	up to 250	4.8-100 9.6 at 433/868 MHz 19.2 at 915 MHz
Overhead bytes in PHY	20	32	15	14	7
Payload/ packet in PHY [%]	92	76	73	78	97
Latency [ms]	2500-5000 in sleep	15 in sleep	2000 in sleep typically 50	device dependent	12.8-12800 (typ. 12800)
Scalability	15 hops	254 nodes	3 hops	2-~30 nodes (4 hops)	200 nodes
Security	AES, CRC	AES, CRC	XTEA, CRC	XTEA, CRC	AES, RSA, 3DES, FEC with BCH
Technologies used in PHY/MAC	GFSK, CSMA-CA	DSSS, BPSK, CSMA-CA	2-FSK, CSMA	(G)FSK, OOK/ASK	FHSS, GFSK, SCP (Scheduled Channel Polling) similar to SMAC
Λ parameter [bit/J]	5690	2501	1003	1229	5460

Table 1 – Comparison of investigated protocols

5. EFFICIENCY MEASURES

The calculation method presented below grades the smart metering protocols' energy efficiency.

In the presented calculations the devices have the following five distinct modes:

- The device is in sleep mode
- The device transmits user data packets
- The device processes or makes calculations on user data (radio off)
- The device transmits management information
- The device processes management information (radio off)

It is important to distinguish these modes, because the device operates on different energy levels in these different modes. In this approach the user data is handled only in two modes, the management data is considered as overhead.

An interesting and important problem would be to determine whether the data should be processed on the device and transmitted less frequently, or all information should be sent in every case. The formulas below can answer this question.

During the creation of the formulas, relatively easily measurable - or accessible from the data sheets - data is used.

The ratio of user data and all packets sent in time T is calculated in formula (1), where T is the measured time all the calculations are based on.

$$\alpha = \frac{number\ of\ \ user\ data\ packets\ in\ T}{number\ of\ all\ packets\ in\ T} \quad (1)$$

Expression (2) shows the amount of time needed to send data packets in time *T*.

$$t_{data\ send} = \alpha \cdot \frac{|user\ data\ packet|}{transmission\ speed} \quad [\text{s}] \quad (2)$$

, where $|x|$ means the number of bits in x.

The time needed to send management packets in time *T* can be calculated as

$$t_{man\ send} = (1-\alpha) \cdot \frac{|\ management\ packet|}{transmission\ speed} \quad [\text{s}] \quad (3)$$

The following definition gives the amount of time spent by the device in non-sleeping mode.

$$t = t_{data\ send} + t_{data\ proc} + t_{man\ send} + t_{man\ proc} \quad [\text{s}] \quad (4)$$

, where $t_{data\ proc}$ means the time used for processing data packets, and $t_{man\ proc}$ is the processing time of management packages.

E_{sleep} refers to the amount of energy used by the device in sleeping mode.

$$E_{sleep} = (T-t) \cdot P_{sleep} \quad [\text{J}] \quad (5)$$

, where P_{sleep} is the power of the sleeping device. (T-t) is the amount of time spent in sleep mode of time T.

Formula (6) calculates the amount of energy used for sending and processing management packets.

$$E_{management} = t_{man\ send} \cdot P_{send} + t_{man\ proc} \cdot P_{active} \quad [\text{J}] \quad (6)$$

, where P_{send} is the transmitting power consumption (with an active radio module), P_{active} denotes the active mode power consumption (without radio mode on).

Similar to (5) the energy needed to send and process data packets is calculated by formula (7).

$$E_{data} = t_{data\ send} \cdot P_{send} + t_{data\ proc} \cdot P_{active} \quad [\text{J}] \quad (7)$$

, where the power values are the same as before and the time values are labeling the data packets as previously.

With these calculated energy amounts the total energy used by the protocol in time *T* can be summed as

$$E_{total} = E_{sleep} + E_{management} + E_{data} \quad [\text{J}] \quad (8)$$

Assuming also the knowledge of the number of payload bits in data packets, it can be calculated that how much user data the selected protocol can transfer in one energy unit.

$$\Lambda = \frac{|data\ packet\ payload|}{E_{total}} \quad \left[\frac{\text{bit}}{\text{J}}\right] \quad (9)$$

The result of these formulas shows a protocol and device specific number and is suitable for comparison of efficiency of the different solutions. The devices' consumption in different modes is unique and the time they spend in those modes is protocol specific, so this formula combines hardware and software efficiency. The final result is measured in useful bit/Joule ratio, which can be easily used for further calculations of battery lifetime and amount of data transmitted. This result measures the whole system, which consists of a device and a protocol.

Assumptions used in calculations:

- The device is awake in 1% of time and is in sleep mode in 99% of time [14]
- The packets are 20% data and 80% management information filled so $\alpha = 0.2$
- T is one hour

Figure 2 shows the calculated values for each protocol using the same assumptions and MicaZ hardware's performance values [15].

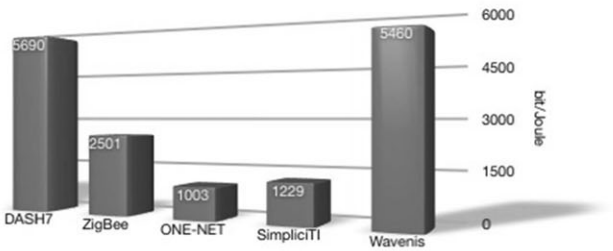

Figure 2 – Λ results compared for investigated protocols

As Figure 2 shows there are significant differences between the solutions. The higher values are better. DASH7 and Wavenis can transmit more user data using 1 Joule of energy. Among all parameters of Table 1, the Payload/packet value correlates the most to Λ.

6. MEASUREMENTS

Another important factor besides energy efficiency - considered in the previous section - is the frequency-dependent range of the various protocols, which means how far the bits containing useful information can be transmitted.

The 2.4 GHz ISM frequency band is crowded, thus jamming and interference is significant. Moreover the waves in this frequency cannot propagate through water and concrete, which can be a disadvantage because of the meters' location, as opposed to the 433 MHz and 868 MHz bands which have suitable properties for smart metering

applications. Therefore, the mesurements were conducted with 433.92 MHz and 868 MHz with 10 mW transmission power in various environments: inside a building, from indoor to outdoor, and LOS environment at an airport. The received signal strengths were recorded.

The first set of measurements was conducted indoors. The results are presented in Table 2 and Figure 3. When the devices were 3 floors away, they lost connection. The building's ferroconcrete structure absorbs radio signals to a great extent, especially at 868 MHz.

Placemark	*433 MHz*	*866 MHz*
A	-14 dBm	-25 dBm
B	-68 dBm	-68 dBm
C	-42 dBm	-61 dBm
D	-86 dBm	-95 dBm
E	-70 dBm	-87 dBm
F	no signal	no signal

Table 3 – Indoor measurements

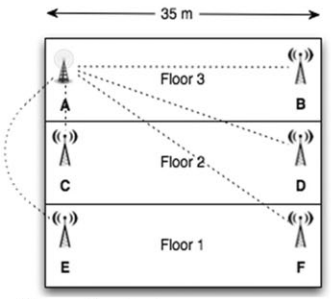

Figure 3 – Indoor measurements

The second set of measurements was conducted from indoor to outdoor. At point C shown on Figure 4 a fracture in signal strength can be noticed, as the measurement was carried out at the opposite side of the building. Table 3 shows the measured values.

Placemark	*Distance from Laboratory*	*433 MHz*	*866 MHz*
A	15 m	-78 dBm	-90 dBm
B	90 m	-80 dBm	-92 dBm
C	100 m	-90 dBm	no signal
D	150 m	-87 dBm	-95 dBm
E	210 m	-84 dBm	-94 dBm
F	250 m	-87 dBm	-94 dBm

Table 3 – Indoor to outdoor measurements

Figure 4 – Indoor to outdoor measurements map

The third set of measurements was conducted outdoors at an airport. Figure 5 shows a map of the location. Table 4 concludes the measured values alongside the calculated values for 433 MHz, 868 MHz and 2.4 GHz. The calculated values estimate the ideal Signal to Noise Ratio (SNR) of a clear channel. The measured values are lower than the calculated values, as background noise was significant.

Place-mark	*Distance to Base*	*433 MHz measured*	*433 MHz calculated*	*868 MHz calculated*	*2.4 GHz calculated*
A	173 m	-70 dBm	-58.65 dBm	-64.68 dBm	-73.51 dBm
B	335 m	-79 dBm	-64.39 dBm	-70.42 dBm	-79.25 dBm
C	564 m	-85 dBm	-68.92 dBm	-74.95 dBm	-83.78 dBm
D	774 m	-95 dBm	-71.67 dBm	-77.69 dBm	-86.53 dBm
E	1045 m	-100 dBm	-74.28 dBm	-80.3 dBm	-89.14 dBm

Table 4 – Outdoor measurements

Figure 5 – Outdoor measurements map

The fourth set of measurements was conducted on 433 MHz in a rural environment. These measurements were based on a real-world scenario as the meter was placed in a chamber (at the water pipes) and at the electricity box. The measurement points are presented on Figure 6. The measured values for the two scenarios are summarized in Table 5. The water chamber significantly shades the signal, so at further distances no signal was measured. The signal strength dropped more rapidly than at the second measurement, where indoor to outdoor performance was evaluated.

Placemark	*Distance from meter*	*Water chamber*	*Electricity meter*
A	192 m	-101 dBm	-85 dBm
B	149 m	-99 dBm	-83 dBm
C	77 m	-95 dBm	-73 dBm
D	19 m	-75 dBm	-54 dBm
E	79 m	-93 dBm	-78 dBm
F	107 m	-100 dBm	-91 dBm
G	195 m	no signal	-94 dBm
H	266 m	no signal	-98 dBm
I	305 m	no signal	-97 dBm
J	354 m	no signal	no signal
K	336 m	no signal	-100 dBm
L	289 m	no signal	-96 dBm
M	316 m	no signal	-96 dBm

Table 5 – Rural environment measurements

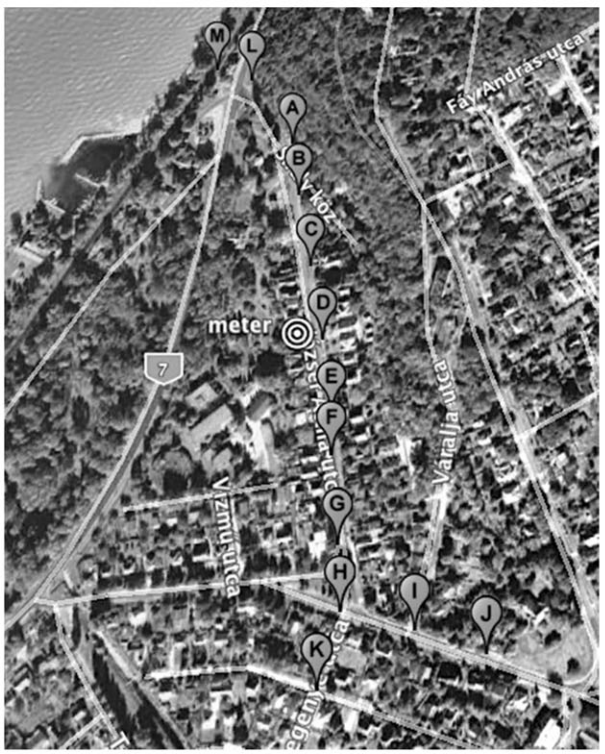

Figure 6 – Map of rural environment measurements

The measurements proved that a 433 MHz frequency signal has better propagation properties, than an 868 MHz signal, hence more suitable for smart metering applications.

7. CONCLUSIONS

In this article different wireless smart metering technologies were investigated and a formula was created which enables to determine the efficiency of the protocols in bit/Joule. The efficiency of wireless smart metering technologies were calculated. According to the results, DASH7 and Wavenis has the best bit/Joule ratio. Also the range of used frequencies were compared.

This research helps companies to decide which technology to select according to their goals. A formula can be constructed to give a preference-weighted correlated evaluation about the strengths and weaknesses of each protocol according to their custom needs.

Further research can be conducted to determine the impact of processing and storage of data on the devices, instead of instantaneous transmission.

REFERENCES

[1] Berg Insight: News Archive
http://www.berginsight.com/News.aspx?m_m=6
[2] *"ISO/IEC-18000-7 INTERNATIONAL STANDARD"* Third Edition 2009-08-01
[3] Tatsiopoulos, C. and Ktena, A., "A Smart ZIGBEE Based Wireless Sensor Meter System" *16th International Conference on Systems Signals and Image Processing 1-4*, 2009.
[4] T. Ryan Burchfield, S. Venkatesan, Douglas Weiner, "Maximizing Throughput in Zigbee Wireless Networks through Analysis, Simulations and Implementations". *University of Texas at Dallas, 2007.*
[5] ZigBee Specification January 17, 2008.
http://people.ece.cornell.edu/land/courses/ece4760/FinalProjects/s2011/kjb79_ajm232/pmeter/ZigBee%20Specification.pdf
[6] ONE-NET Specification Version 1.6.2 February 11, 2011
http://www.one-Net.info/spec/ONE_NET_1_6_2_DOCUMENTATION.zip
[7] SimpliciTI Overview
http://www.ti.com/corp/docs/landing/simpliciTI/index.htm?DCMP=hpa_rf_general&HQS=NotApplicable+OT+simpliciti
[8] Larry Friedman, "SimpliciTI: Simple Modular RF Network Specification" Texas Instruments Inc., San Diego, California USA, 2009.
[9] Wavenis Datasheet
http://www.coronis.com/en/wavenis_technology.html
[10] Specification of the Bluetooth System 1999.
http://grouper.ieee.org/groups/802/15/Bluetooth/profile_10_b.pdf
[11] Zensys Launches the First RF Single Chip Portfolio for IR Replacement in AV Control
http://www.zen-sys.com/modules/iaCM-ZW-PR/readMore.php?id=16777216
[12] Geoff Mulligan. "The 6LoWPAN Architecture" in proceedings of the *4th workshop on Embedded networked sensors ACM*, New York, 2007.
[13] Klaas De Craemer, Geert Deconinck: "Analysis of State-of-the-art Smart Metering Communication Standards" *Leuven, YRS,* 2010.
[14] Mikhail Nesterenko: "IEEE 802.15.4" presentation
deneb.cs.kent.edu/~mikhail/classes/seminar.u04/praveen_lrwpan.ppt
[15] MICAz Wireless Measurement System Datasheet, *Crossbow Technology, Inc. San Jose, California*
http://www.openautomation.net/uploadsproductos/micaz_datasheet.pdf

Call for Papers

Prospective authors are invited to submit original research papers for publication in the upcoming issues of our Infocommunications Journal.

Topics of interests include the following areas:

- Data and network security
- Digital broadcasting
- Infocommunication services
- Internet technologies and applications
- Media informatics
- Multimedia systems
- Optical communications
- Society-related issues
- Space communications
- Telecommunication software
- Telecom. economy and regulation
- Testbeds and research infrastructures
- Wireless and mobile communications

Theoretical and experimentation research results achieved within the framework of European ICT projects are particularly welcome. From time to time we publish special issues and feature topics so please follow the announcements. Propo-sals for new special issues and feature topics are welcome.

Our journal is currently published quarterly and the editors try to keep the review and decision process as short as possible to ensure a timely publication of the paper, if accepted. As for manuscript preparation and submission, please follow the guidelines published on our website

http://www.infocommunications.hu/for_our_authors.

Authors are requested to send their manuscripts via electronic mail (preferably) or on a CD by regular mail to the Editor-in-Chief:

Csaba A. Szabo
Dept. of Telecommunications,
Budapest University of Technology and Economics
2 Magyar Tudosok krt. Budapest 1117 Hungary
E-mail: szabo@hit.bme.hu

Call for Proposals of Special Issues

Infocommunications Journal welcomes proposals for Special Issues – collections of papers dedicated to a particular topic of interest for the readers of the journal.

A Special Issue can be based on a recent high quality workshop or conference or papers can be collected from open call. Invited papers can be part of the special issue as well.

A Special Issue can fill in a whole issue, in which case the number of papers is expected to be 8 to 10, or it can be a Mini – Special Issue. In the latter case, at least 3, preferably 4 papers are required.

Proposals for special issues should include:

– contact information
(name, e-mail, title, affiliation and address);
– resume(s) of the proposer(s), with a representative list of recent publications and related experience
(Editorial Board memberships, Guest Editorships, or roles in relevant conferences' program committees);
– the proposed title for the special issue;
– the way the special issue will be compiled
(contributions solicited from a technical event, or to be collected from call for this special issue;
– intent to include invited papers should be also indicated, if possible with the names of professionals who are planned to be invited;
– scope and motivation and description of the special issue;
– guest editors (if different from the proposers) with detailed contact information and resumes.

Proposals should be sent to the Editor-in-Chief:

Csaba A. Szabo
Dept. of Telecommunications,
Budapest University of Technology and Economics
2 Magyar Tudosok krt. Budapest 1117 Hungary
E-mail: szabo@hit.bme.hu

Guidelines for our authors

Format of the manuscripts

Original manuscripts and final versions of papers should be submitted in IEEE format according to the formatting instructions available on
http://www.ieee.org/publications_standards/publications/authors/authors_journals.html#sect2,
"Template and Instructions on How to Create Your Paper".

Length of the manuscripts

The length of papers in the aforementioned format should be 6-8 journal pages.
Wherever appropriate, include 1-2 figures or tables per journal page.

Paper structure

Papers should follow the standard structure, consisting of *Introduction* (the part of paper numbered by "1"), and *Conclusion* (the last numbered part) and several *Sections* in between.
The Introduction should introduce the topic, tell why the subject of the paper is important, summarize the state of the art with references to existing works and underline the main innovative results of the paper. The Introduction should conclude with outlining the structure of the paper.

Accompanying parts

Papers should be accompanied by an *Abstract* and a few *index terms (Keywords)*. For the final version of accepted papers, please send the *short cvs* and *photos* of the authors as well.

Authors

In the title of the paper, authors are listed in the order given in the submitted manuscript. Their full affiliations and e-mail addresses will be given in a footnote on the first page as shown in the template. No degrees or other titles of the authors are given. Memberships of IEEE, HTE and other professional societies will be indicated so please supply this information.
When submitting the manuscript, one of the authors should be indicated as corresponding author providing his/her postal address, fax number and telephone number for eventual correspondence and communication with the Editorial Board.

References

References should be listed at the end of the paper in the IEEE format, see below:

a) Last name of author or authors and first name or initials, or name of organization
b) Title of article in quotation marks
c) Title of periodical in full and set in italics
d) Volume, number, and, if available, part
e) First and last pages of article
f) Date of issue

[11] Boggs, S.A. and Fujimoto, N., "Techniques and instrumentation for measurement of transients in gas-insulated switchgear," IEEE Transactions on Electrical Installation, vol. ET-19, no. 2, pp.87–92, April 1984.

Format of a book reference:

[26] Peck, R.B., Hanson, W.E., and Thornburn, T.H., Foundation Engineering, 2nd ed. New York: McGraw-Hill, 1972, pp.230–292.

All references should be referred by the corresponding numbers in the text.

Figures

Figures should be black-and-white, clear, and drawn by the authors. Do not use figures or pictures downloaded from the Internet. Figures and pictures should be submitted also as separate files. Captions are obligatory. Within the text, references should be made by figure numbers, e.g. "see Fig. 2."
When using figures from other printed materials, exact references and note on copyright should be included. Obtaining the copyright is the responsibility of authors.

Contact address

Authors are requested to send their manuscripts via electronic mail or on an electronic medium such as a CD by mail to the Editor-in-Chief:

Csaba A. Szabo
Dept. of Telecommunications
Budapest University of Technology and Economics
2 Magyar Tudosok krt.
Budapest 1117 Hungary
szabo@hit.bme.hu

SCIENTIFIC ASSOCIATION FOR INFOCOMMUNICATIONS

Who we are

Founded in 1949, the Scientific Association for Infocommunications (formerly known as Scientific Society for Telecommunications) is a voluntary and autonomous professional society of engineers and economists, researchers and businessmen, managers and educational, regulatory and other professionals working in the fields of telecommunications, broadcasting, electronics, information and media technologies in Hungary.

Besides its more than 1300 individual members, the Scientific Association for Infocommunications (in Hungarian: Híradástechnikai és Informatikai Tudományos Egyesület, HTE) has more than 60 corporate members as well. Among them there are large companies and small-and-medium enterprises with industrial, trade, service-providing, research and development activities, as well as educational institutions and research centers.

HTE is a Sister Society of the Institute of Electrical and Electronics Engineers, Inc. (IEEE) and the IEEE Communications Society. HTE is corporate member of International Telecommunications Society (ITS).

What we do

HTE has a broad range of activities that aim to promote the convergence of information and communication technologies and the deployment of synergic applications and services, to broaden the knowledge and skills of our members, to facilitate the exchange of ideas and experiences, as well as to integrate and harmonize the professional opinions and standpoints derived from various group interests and market dynamics.

To achieve these goals, we…

- contribute to the analysis of technical, economic, and social questions related to our field of competence, and forward the synthesized opinion of our experts to scientific, legislative, industrial and educational organizations and institutions;
- follow the national and international trends and results related to our field of competence, foster the professional and business relations between foreign and Hungarian companies and institutes;
- organize an extensive range of lectures, seminars, debates, conferences, exhibitions, company presentations, and club events in order to transfer and deploy scientific, technical and economic knowledge and skills;
- promote professional secondary and higher education and take active part in the development of professional education, teaching and training;
- establish and maintain relations with other domestic and foreign fellow associations, IEEE sister societies;
- award prizes for outstanding scientific, educational, managerial, commercial and/or societal activities and achievements in the fields of infocommunication.

Contact information

President: **DR. GÁBOR HUSZTY** • *ghuszty@entel.hu*

Secretary-General: **DR. ISTVÁN BARTOLITS** • *bartolits@nmhh.hu*

Managing Director, Deputy Secretary-General: **PÉTER NAGY** • *nagy.peter@hte.hu*

International Affairs: **ROLLAND VIDA, PhD** • *vida@tmit.bme.hu*

Addresses

Office: H-1055 Budapest, V. Kossuth Lajos square 6-8, Room: 422.

Mail Address: 1372 Budapest, Pf. 451., Hungary

Phone: +36 1 353 1027, Fax: +36 1 353 0451

E-mail: *info@hte.hu*, Web: *www.hte.hu*